

AEDC-TR-84-3

~~172-1007~~
~~85-123~~
AEDC/PA

85-123

~~ATTN: Mr. Cote~~
~~(Replacement Copy)~~

Analysis of Heat-Transfer Measurements
from Two AEDC Wind Tunnels on the
Shuttle External Tank

Kenneth W. Nutt
Calspan Field Services, Inc.

October 1984

Final Report for Period October 1982 -- November 1983

(NASA-CR-171470) ANALYSIS OF HEAT-TRANSFER
MEASUREMENTS FROM 2 AEDC WIND TUNNELS ON THE
SHUTTLE EXTERNAL TANK Final Report, Oct.
1982 - Nov. 1983 (Calspan Field Services,
Inc.) 81 p HC AC5/MF A01

NE5-28263

Unclas
21476

CSCI 20D G3/34

**ARNOLD ENGINEERING DEVELOPMENT CENTER
ARNOLD AIR FORCE STATION, TENNESSEE
AIR FORCE SYSTEMS COMMAND
UNITED STATES AIR FORCE**



UNCLASSIFIED

SECURITY CLASSIFICATION OF THIS PAGE

REPORT DOCUMENTATION PAGE

1a. REPORT SECURITY CLASSIFICATION UNCLASSIFIED			1b. RESTRICTIVE MARKINGS			
2a. SECURITY CLASSIFICATION AUTHORITY			3. DISTRIBUTION/AVAILABILITY OF REPORT			
2b. DECLASSIFICATION/DOWNGRADING SCHEDULE						
4. PERFORMING ORGANIZATION REPORT NUMBER(S) AEDC-TR-84-3			5. MONITORING ORGANIZATION REPORT NUMBER(S)			
6a. NAME OF PERFORMING ORGANIZATION Arnold Engineering Development Center		6b. OFFICE SYMBOL (if applicable)	7a. NAME OF MONITORING ORGANIZATION			
6c. ADDRESS (City, State and ZIP Code) Air Force Systems Command Arnold Air Force Station, TN 37389			7b. ADDRESS (City, State and ZIP Code)			
8a. NAME OF FUNDING/SPONSORING ORGANIZATION See Next Page		8b. OFFICE SYMBOL (if applicable)	9. PROCUREMENT INSTRUMENT IDENTIFICATION NUMBER			
8c. ADDRESS (City, State and ZIP Code)			10. SOURCE OF FUNDING NOS			
11. TITLE (Include Security Classification) See Next Page			PROGRAM ELEMENT NO.	PROJECT NO.	TASK NO.	WORK UNIT NO.
			65807F			
12. PERSONAL AUTHOR(S) Nutt, Kenneth W., Calspan Field Services, Inc.						
13a. TYPE OF REPORT Final Report		13b. TIME COVERED FROM 10/1/82 TO 11/30/83		14. DATE OF REPORT (Yr., Mo., Day)		15. PAGE COUNT
16. SUPPLEMENTARY NOTATION						
17. COSATI CODES			18. SUBJECT TERMS (Continue on reverse if necessary and identify by block number)			
FIELD	GROUP	SUB GR.	heat transfer Reynolds number aerothermodynamics			
20	13		space shuttles aerodynamic heating enthalpy			
14	02		Mach number wind tunnel tests			
19. ABSTRACT (Continue on reverse if necessary and identify by block number) Previous aerodynamic heating tests have been conducted in the AEDC/VKF Supersonic Wind Tunnel (A) to aid in defining the design thermal environment for the Space Shuttle external tank. The quality of these data has been under discussion because of the effects of low tunnel enthalpy and slow model-injection rates. Recently the AEDC/VKF Hypersonic Wind Tunnel (C) has been modified to provide a Mach 4 capability that has significantly higher tunnel enthalpy with more rapid model-injection rates. Tests were conducted in Tunnel C at Mach 4 to obtain data on the external tank for comparison with Tunnel A results. Data were obtained on a 0.0175-scale model of the Space Shuttle Integrated Vehicle at $Re/ft = 4 \times 10^6$ with the tunnel stagnation temperature varying from 740° to $1440^\circ R$. Model attitude varied from an angle of attack of -5 to 5 deg and an angle of sideslip of -3 to 3 deg. One set of data was obtained in Tunnel C at $Re/ft = 6.9 \times 10^6$ for comparison with flight data. This report presents data comparisons between the two tunnels for numerous regions on the external tank. Tunnel-to-flight data (Cont)						
20. DISTRIBUTION/AVAILABILITY OF ABSTRACT UNCLASSIFIED/UNLIMITED <input type="checkbox"/> SAME AS RPT. <input checked="" type="checkbox"/> DTIC USERS <input type="checkbox"/>			21. ABSTRACT SECURITY CLASSIFICATION UNCLASSIFIED			
22a. NAME OF RESPONSIBLE INDIVIDUAL W. O. Cole			22b. TELEPHONE NUMBER (Include Area Code) (615)455-2611 Ext. 7813		22c. OFFICE SYMBOL DOS	

UNCLASSIFIED

SECURITY CLASSIFICATION OF THIS PAGE

8a, b, and c. FUNDING AND SPONSORING ORGANIZATION

NASA/MSFC - Huntsville, AL 35812

and

AEDC/DO - Arnold AFS, TN 37389

11. TITLE

Analysis of Heat-Transfer Measurements from Two AEDC Wind Tunnels
on the Shuttle External Tank

19. ABSTRACT (Cont)

comparisons are presented for a small number of locations on the nose of
the external tank.

UNCLASSIFIED

SECURITY CLASSIFICATION OF THIS PAGE

PREFACE

The work reported herein was performed by the Arnold Engineering Development Center (AEDC), Air Force Systems Command (AFSC). The program was jointly sponsored by the National Aeronautics and Space Administration, Marshall Space Flight Center (NASA/MSFC), Huntsville, Alabama, and the Aerospace Flight Dynamics Testing Office (DOFA), AEDC. The NASA/MSFC Project Manager was Mr. L. D. Foster, and the AEDC/DOFA Project Manager was Mr. J. T. Best. The results were obtained by Calspan Field Services, Inc./AEDC Division, operating contractor for the aerospace flight dynamics testing effort at the AEDC, AFSC, Arnold Air Force Station, Tennessee. The work was performed under AEDC Project Number C796VW (Calspan Project Number V44W-4L). The data analysis was completed on November 30, 1983, and the manuscript was submitted for publication on January 4, 1984.

The author wishes to express his appreciation to Mr. W. K. Crain, formerly of Calspan Field Services, Inc., for his contribution in directing the test program that provided the data base for this report. In addition, thanks are due Mr. R. K. Matthews, Calspan Field Services, Inc., for his consultation.

CONTENTS

	<u>Page</u>
1.0 INTRODUCTION	5
2.0 APPARATUS	5
2.1 Test Facilities	5
2.2 Test Article	7
2.3 Instrumentation	7
3.0 PROCEDURES	8
3.1 Test Conditions	8
3.2 Test Procedures	8
3.3 Wind Tunnel Data Reduction	9
3.4 Flight Data Reduction	11
4.0 RESULTS AND DISCUSSION	13
4.1 Wind Tunnel Data Comparison	13
4.2 Wind Tunnel-to-Flight Data Comparison	16
5.0 CONCLUDING REMARKS	16
REFERENCES	17

ILLUSTRATIONS

Figure

1. Schematic View of Tunnel A	19
2. Tunnel A Model-Cooling Manifold	21
3. Tunnel C Mach 4.0 Configuration	22
4. Tunnel C Model-Cooling Manifold	24
5. Model Sketch	25
6. Model Installation in Aerothermal Tunnel (C)	26
7. Model Installation in Tunnel A	28
8. Details of 0.0175-Scale External Tank	30
9. Model Instrumentation Locations	35
10. Variation of R on External Tank	37
11. Temperature Profile caused by Presence of Gage in an Insulating Material	38
12. Data Comparison with Analytical Turbulent Heat-Transfer-Rate Distribution on the External Tank Alone	39
13. Model Shadowgraph Photographs for $\alpha = 0$, $\beta = 0$	40
14. Data Repeatability	43

<u>Figure</u>	<u>Page</u>
15. Distribution of Measurement Repeatability	47
16. Comparability of Tunnel A to Tunnel C Measurements	49
17. Gage Measurement Influenced by Thermal Conduction	50
18. Heating Distribution on Nose Section (Theta = 25 deg)	51
19. Heating Distribution on Bottom Centerline (Theta = 180 deg)	52
20. Heating Distribution on Top Centerline of External Tank in Region of Orbiter Bow-Shock Impingement	54
21. Heating Distribution in the Region of Forward SRB Attach Strut (Theta = 280 deg)	57
22. Heating Distribution Between LO ₂ Anti-Geyser and LO ₂ Feed Lines (Theta = 32 deg)	60
23. Heating Distribution Near the Rear Orbiter-to-Tank Attach Strut (Theta = 68 deg)	62
24. Influence of Temperature Difference (TT - TW) on Measured Heating Coefficient	65
25. Wind Tunnel-to-Flight Data Comparison	67

TABLES

	<u>Page</u>
1. Model Instrumentation Locations	69
2. Test Data Summary	71

APPENDIX

A. Importance of Recovery Temperature	73
NOMENCLATURE	76

1.0 INTRODUCTION

Tests have been performed in the 40-in. Supersonic Wind Tunnel (A) at the von Karman Gas Dynamics Facility (VKF) to obtain heat-transfer-rate data on the Space Shuttle Integrated Vehicle. When the initial Shuttle-heating test requirements were evaluated, Tunnel A was the only test unit available at AEDC/VKF that could provide data in the Mach number range of 3.0 to 5.5. During this evaluation there were factors identified with the tunnel operation that could influence the quality of the heating measurements. These factors were (1) the tunnel operates with a low stagnation enthalpy providing a low driving potential for heat transfer, (2) slow model-injection rates, and (3) tunnel-induced interference. Steps were taken to minimize the influence of these factors, but they were not eliminated.

The Hypersonic Wind Tunnel (C) Mach 10 circuit has recently been modified to include a Mach 4 aerothermal configuration. With the addition of this modification to Tunnel C came the capability to provide Mach 4 conditions similar to those run in Tunnel A, but at a much larger temperature-driving potential and with rapid model-injection rates directly into the test section. Thus, Hypersonic Wind Tunnel (C) is converted to Aerothermal Tunnel (C).

The objectives of this program were twofold. The primary objective was to compare heating data obtained on the Space Shuttle external tank in Aerothermal Tunnel (C) (Ref. 1) at conditions comparable to a previous test (Ref. 2) in Tunnel A. The configuration tested was the 0.0175-scale Rockwell International 60-OTS Integrated Space Shuttle Vehicle. The comparable test conditions were run at $M = 4.0$, $Re/ft = 4 \times 10^6$, and $TT = 740^\circ R$. Additional data were obtained in Aerothermal Tunnel (C) at nearly constant Re/ft but with increases in the tunnel stagnation temperature over the range of 740 to 1440°R. Model attitude was varied from an angle of attack of -5 to 5 deg and an angle of sideslip from -3 to 3 deg. The secondary objective was to compare the tunnel data to selected flight data from STS-4.

2.0 APPARATUS

2.1 TEST FACILITIES

2.1.1 Tunnel A

Tunnel A is a continuous, closed-circuit, variable-density wind tunnel with an automatically driven flexible-plate-type nozzle and a 40- by 40-in. test section. The tunnel can be operated at Mach numbers from 1.5 to 6 at maximum stagnation pressures from 29 to 200 psia, respectively, and stagnation temperatures up to 750°R ($M = 6$). Minimum operating pressures range from about one-tenth to one-twentieth of the maximum at each number. The tunnel is equipped with a model-injection system which allows removal of the

model from the test section while the tunnel remains in operation. A schematic view of Tunnel A is presented in Fig. 1. Performance and operational characteristics of Tunnel A are detailed in Ref. 3.

A schematic view of the model-injection system is presented in Fig. 1b. With this system, the model is injected into the tunnel downstream of the test section. The injection stroke requires approximately 13 sec to reach the tunnel centerline. When the model reaches the tunnel centerline, there is a slight delay (1 to 2 sec) to actuate the axial drive. The axial-drive unit translates the model upstream to the test section in approximately 5 sec.

A model-cooling manifold was located in the injection tank (Fig. 2). This manifold was capable of cooling the model to approximately 15°F with chilled air supplied from a vortex generator (Hilsch vortex tube, Ref. 4). The cooling manifold, which is normally located to the side of the model, was modified (Fig. 2) to allow the model attitude to be set, and then injected directly out of the cooling environment into the tunnel.

2.1.2 Aerothermal Tunnel (C)

The Mach 4 Aerothermal Tunnel (C) is a closed-circuit, high-temperature, supersonic, free-jet wind tunnel with an axisymmetric contoured nozzle and a 25-in.-diam nozzle exit, Fig. 3. This tunnel utilizes parts of the Tunnel C circuit (the electric air heater, the Tunnel C test section and injection system) and operates continuously over a range of pressures from nominally 15 psia at a minimum stagnation temperature of 710°R to 180 psia at a maximum temperature of 1570°R. Using the normal Tunnel C Mach 10 circuit (Series Heater Circuit), the Aerothermal Mach 4 nozzle operates at a maximum pressure and temperature of 100 psia and 1900°R, respectively. The air temperatures and pressures are normally achieved by mixing high-temperature air (up to 2250°R) from the primary flow discharged from the electric heater with the bypass airflow (at 1440°R) from the natural gas-fired heater. The primary and the bypass airflows discharge into a mixing chamber just upstream of the aerothermal tunnel stilling chamber. The entire aerothermal nozzle insert (the mixing chamber, throat and nozzle sections) is water-cooled by integral external, water jackets. Calibration and performance data pertaining to the Tunnel C, Mach number 4, aerothermal tunnel are documented in Ref. 5.

The model-support injection/retraction system allows the model to be injected directly from the model-injection tank into the test section. The injection stroke requires nominally 2 sec to reach tunnel centerline. The model can be retracted from the test section while the free-jet tunnel remains in operation.

The Tunnel C model-cooling manifold is shown in Fig. 4. The manifold was supplied with pressurized air capable of cooling the model to 40 to 70°F.

2.2 TEST ARTICLE

The test article was a 0.0175-scale, thin-skin-thermocouple model of the Rockwell International Vehicle 5 configuration of the Space Shuttle. The model was adapted for installation of Schmidt-Boelter gages (Ref. 6) at selected locations. Rockwell International fabricated the model and supplied the model drawings. A sketch of the model showing the model coordinate system and reference length is presented in Fig. 5. The integrated model was composed of the orbiter vehicle, external tank (ET), and two solid-propellant rocket booster (SRB) motors that are identified in Fig. 6a. The model was designated as the 60-OTS model, and the configuration tested reflects Shuttle Configuration Control VC72-000002F.

An installation photograph of the 60-OTS model in Aerothermal Tunnel (C) is shown in Fig. 6a, and an installation sketch of the model is shown in Fig. 6b. An installation photograph and sketch of the same model in Tunnel A are shown in Figs. 7a and b, respectively.

The external tank was constructed of 17-4 PH stainless steel. Details of the external tank model and associated protuberances are presented in Fig. 8. A new, instrumented, corrugated intertank, Fig. 8a, was installed on the external tank for the tests documented in this report.

2.3 INSTRUMENTATION

The instrumentation, recording devices, and calibration methods used to measure the primary tunnel and test data parameters in Tunnel C are documented in Ref. 1, along with the estimated uncertainties. The same information for the measurements made in Tunnel A is documented in Ref. 2.

The 60-OTS model was instrumented with 30-gage Chromel[®]-constantan, thin-skin thermocouples and 0.050-in.-diam thermopile Schmidt-Boelter heat-transfer gages. The principle of operation of the Schmidt-Boelter gage is described in Ref. 6. The only instrumentation that will be discussed in this report is that which was installed on the external tank and functioned for both the Tunnel C and Tunnel A tests. These instruments are shown in Fig. 9 and identified by location and type in Table 1.

Certain instruments were positioned at locations where developmental flight instrumentation (DFI) was placed on the full-scale flight test Space Shuttle. Data from selected instruments at these DFI locations were compared with flight data from flight STS-4.

3.0 PROCEDURES

3.1 TEST CONDITIONS

The nominal conditions at which the wind tunnel tests were conducted in each tunnel are given below:

<u>Tunnel</u>	<u>M</u>	<u>PT, psi</u>	<u>TT, °R</u>	<u>hREF, Btu/ft²-sec-°R</u>	<u>Re, ft⁻¹</u>
A	4.0	72	740	5.1×10^{-2}	4.1×10^6
C	4.0	60	740	4.7×10^{-2}	3.5×10^6
↓	↓	120	740	6.6×10^{-2}	6.9×10^6
		102	980	6.5×10^{-2}	3.8×10^6
		120	1050	7.1×10^{-2}	4.0×10^6
		140	1240	7.8×10^{-2}	3.6×10^6
		175	1440	8.9×10^{-2}	3.6×10^6

Data were obtained on the external tank over the attitude range of angle of attack from -5 to 5 deg and angle of sideslip from -3 to 3 deg. Sideslip angles were attained by pitching and rolling the model. A summary of the test data used in this study is presented in Table 2.

3.2 TEST PROCEDURES

3.2.1 Tunnel A

Figure 2 shows the model mounted on the sting support mechanism and positioned in the cooling manifold in the installation tank directly under the tunnel test section. Before each tunnel injection the model was cooled to approximately 15°F as described in Section 2.1.1. The desired model attitude was established while the model was in the cooling manifold. When the cooling cycle was complete, the model was injected into the rear test section. The location of the model in this position is illustrated by dashed lines in Fig. 7b. The model remained in this position for approximately 2 sec while the axial-drive unit was being actuated. During this time the model was subject to impingement from a shock wave emanating from Pin A. The approximate location of the disturbance at Mach 4 (Ref. 3) is sketched in Fig. 7b. The model was then translated forward to clear the area of shock impingement. At the beginning of the injection cycle, the tunnel flow parameters were recorded. The data acquisition sequence was initiated before the model reached tunnel centerline and continued until the model reached the full-forward position in the test section. When reaching the full-forward position the model was immediately retracted from the tunnel and the cooling cycle repeated.

3.2.2 Aerothermal Tunnel (C)

The same basic procedure of cooling the model, establishing the desired model attitude, and injecting the model into the tunnel flow was followed in the Aerothermal Tunnel (C), with some differences: (1) the model was cooled to only 40 to 70°F; (2) the model was injected directly upward into the test section and did not have to be translated forward; and (3) because of the length of the 0.0175-scale model, an area at the rear of the external tank fell outside the Mach 4 free-jet boundary as shown in Fig. 6b. The data acquisition sequence was initiated at the start of the inject cycle and continued approximately 1.5 sec after the model reached tunnel centerline. The model was then retracted directly back into the tank area and the cooling cycle again started to cool the model to an isothermal state.

3.3 WIND TUNNEL DATA REDUCTION

All free-stream tunnel parameters were computed utilizing the measured pressure and temperature in the stilling chamber and the calibrated Mach number in the test section. Computations for Tunnel A were made based on a perfect-gas isentropic expansion from the stilling chamber. The computations for Tunnel C were modified to account for real-gas effects.

The reduction of the thin-skin-thermocouple data involves the calorimetric heat balance of the thin-skin material with a convective input which in coefficient form is

$$h(TR) = \frac{QDOT}{TR - TW} = \rho bc \frac{dT_W/dt}{TR - TW} \quad (1)$$

Thermal radiation and heat conduction are neglected in the above relationship, and data reduction requires evaluation of dT_W/dt from the temperature time data and determination of model-material properties.

The following procedure was used to aid in the data evaluation and to permit identification of conduction effects. Equation (1) was integrated assuming that the material parameters and TR remained constant which yields

$$\frac{h(TR)}{\rho bc} (t - t_i) = \ln \left[\frac{TR - TW_i}{TR - TW} \right] \quad (2)$$

Differentiation of Eq. (2) with respect to time gives

$$\frac{h(TR)}{\rho bc} = \frac{d}{dt} \ln \left[\frac{TR - TW_i}{TR - TW} \right] \quad (3)$$

Since the left side of Eq. (3) is a constant, the derivative (or slope) must also be constant if conduction effects are negligible.

The thin-skin-thermocouple data were evaluated using a linear least-squares curve fit of the selected data points to determine the value of the slope. The curve fit normally starts at approximately the time the model arrives on tunnel centerline. The data reduction for thermocouples on the external tank between $0.2 \leq X/L \leq 1.0$ was delayed approximately 2.5 sec after the model arrived on tunnel centerline in Tunnel A in order to allow the thermocouples influenced by the tunnel-induced shock to be translated forward out of this region of tunnel flow as discussed in Ref. 7.

The Schmidt-Boelter gages provided measurements of gage output, E, and surface-thermocouple output which were used to calculate the incident heat flux, QDOT, and wall temperature, TW. The gage output and surface thermocouple were sampled five consecutive times and then averaged. The average values of the gage output were then related to the incident heat flux through a calibration scale factor, S.F.:

$$QDOT = (S.F.) (E) \quad (4)$$

The average value of the gage thermocouple output was used to compute the wall temperature through the use of a curve fit of the National Bureau of Standards (NBS) tables for a Chromel-constantan thermocouple. The heat-transfer coefficient was evaluated using the following equation:

$$h(TR) = \frac{QDOT}{TR - TW} \quad (5)$$

The data reduction time for the Schmidt-Boelter gages was initiated when the model reached tunnel centerline. In Tunnel A the data reduction for the gages between $0.2 \leq X/L \leq 1.0$ was delayed 2.5 sec as was the case for the thermocouple data.

With the relatively low Tunnel A stagnation temperatures, TT, the difference between the model-wall temperature, TW, and the recovery temperature, TR, was generally small (<200°F). As this temperature difference becomes smaller, the calculation of the heat-transfer coefficient becomes more sensitive to deviations from the actual recovery temperature. Since the actual value of the recovery temperature, TR, at each measurement location is not known, an analytic method developed by Rockwell International was used as described in Refs. 1 and 2. In this method the value of the recovery temperature is defined as $TR = RTT$ where the following relationships were assumed:

$$R = \frac{TR}{TT} \quad (6)$$

$$TR = T_e \left(1 + \frac{\gamma - 1}{2} r M_e^2 \right) \quad (7)$$

where $r = 0.898$ for turbulent flow and

$$TT = T_e \left(1 + \frac{\gamma - 1}{2} M_e^2 \right) \quad (8)$$

$$M_e = M_e(M, \delta) \quad (9)$$

where δ is the local surface flow deflection angle.

Calculations of R were made for several values of M and δ using the tangent cone flow theory. The computations were curve fit and resulted in an equation of the form

$$R(M, \delta) = a_1 + a_2 \cdot (\sin \delta)^{a_3} \quad (10)$$

where a_1 , a_2 , and a_3 are constants for a turbulent boundary layer for a particular Mach number and were provided by Rockwell International. The values of R calculated for these data at $M = 4$ ranged from 0.922 to 1.0. The distribution of R on the external tank at alpha (α) = 0, beta (β) = 0 is presented in Fig. 10.

The values of heat-transfer coefficient, $h(RTT)$, were normalized using the Fay-Riddell stagnation point heat-transfer coefficient h_{REF} , Ref. 1. The calculation of h_{REF} was based on a hemispherical nose radius of 0.0175 ft (1.0 ft full-scale).

3.4 FLIGHT DATA REDUCTION

The flight data used in this report were obtained from the STS-4 raw measured data for the June 27, 1982 launch (Ref. 8). The trajectory data including altitude, velocity, alpha, beta, dynamic pressure, ambient temperature, ambient pressure, ambient density, and free-stream Mach number were obtained from the Best Estimate Trajectory for STS-4 (BET04). The hot-wall heating data corresponding to a given trajectory time were obtained from the STS Data Base (STS4DB).

The flight data of interest for comparison with the tunnel measurements were obtained at a time when the launch vehicle had obtained $M = 4.0$ and prior to SRB separation. A trajectory time of 119.8 sec fulfilled these requirements on STS-4. The launch vehicle attitude at this time was alpha = 0.75 deg and beta = -0.58 deg. The flight free-stream Reynolds number was $9.4 \times 10^4/\text{ft}$.

The flight heat-transfer coefficient was evaluated using Eq. (5). The hot-wall heat flux, QDOT, corresponding to the selected trajectory time was obtained from STS4DB for the desired DFI instrument. The wall-temperature measurements were not obtained on the flight vehicle; therefore, the gage temperatures were obtained from calculations using a Martin Marietta computer code and actual STS-4 aeroheating data. The free-stream stagnation temperature was calculated using the relationship

$$TT = T(1 + 0.2M^2), \text{ } ^\circ\text{R} \quad (11)$$

Equation (6) was used to calculate the value of recovery temperature, T_R , using the same value of R used to reduce the wind tunnel data at the same location. The resulting heat-transfer coefficient, $h(RTT)$, was normalized using the Fay-Riddell stagnation point heat-transfer coefficient, h_{REF} , calculated for a 1.0-ft-diam nose radius.

Discussions with personnel investigating possible correction factors to the flight heat-flux measurements on the external tank indicate that sizable (≈ 100 percent) correction factors may need to be applied to correct for surface temperature mismatch between the gage and the external tank insulating material. When a relatively "cold" gage is used in an insulating surface, a temperature profile as sketched in Fig. 11 will result. The surface temperature discontinuity will result in a gage measuring a heating rate much higher than that on the insulating surface. This effect has been studied by several investigators as discussed in Refs. 9, 10, and 11. Rubesin, Ref. 9, derived the following relationship to relate the average coefficient across the gage to the local coefficient that would exist in the undisturbed or isothermal case:

$$\frac{h(\text{with gage})}{h(\text{isothermal})} = F\left(\frac{L}{W}\right) + H\left(\frac{L}{W}\right) \left[\frac{TW_2 - TW_1}{TW_2 - TR} \right] \quad (12)$$

(see Fig. 11 for nomenclature)

The functions $F(L/W)$ and $H(L/W)$ are geometrical terms that Rubesin evaluated numerically and included plotted results in Ref. 9. Westkaemper modified the value of $H(L/W)$ to hold over a wider range of Reynolds number in Ref. 11. As the value of L/W approaches unity, the value of $F(L/W) = 1.0$ and $H(L/W) \approx 1.18$. Assuming that TW_1 approaches TR , Eq. (12) becomes

$$\frac{h(\text{with gage})}{h(\text{isothermal})} \approx 1.0 + 1.18(1.0) \approx 2.18$$

This correction factor (2.18) was used to correct the flight data that were compared to the tunnel data in this report. A more meaningful comparison between tunnel and flight would require that

1. gas-stream, surface, and gage temperatures be known,
2. the flow in the boundary layer at the surface approximates the flat-plate flow assumed in the analysis, and
3. the distance of the gage from the start of the boundary layer be known.

4.0 RESULTS AND DISCUSSION

4.1 WIND TUNNEL DATA COMPARISON

The initial step in examining the wind tunnel data from both tunnels was to compare test data to analytical calculations for each tunnel. Analytical values of turbulent heat-transfer coefficients for noninterference flow over the external tank were normalized using hREF and are presented in Fig. 12. The method of DeJarnette, Refs. 12, 13, and 14, was used to compute the heating levels with pressures calculated from modified Newtonian theory. The computed values are compared with data from each tunnel over the nose section of the external tank ($0 \leq X/L \leq 0.2$) where the flow was not influenced by the orbiter or the solid-propellant rocket boosters. The data from each tunnel agree well ($\approx \pm 10$ percent) with the computed values in this region of noninterference flow. The data downstream of $X/L = 0.3$ are in an interference-flow region and the analytical values apply only to noninterference flow.

The repeatability of the data from each tunnel was examined before comparing data between tunnels. The repeatability data were obtained at a model attitude of $\alpha = 0$ and $\beta = 0$. For reference purposes, the flow-field shadowgraph photographs at this model attitude are shown in Fig. 13. A random sample of instruments representing various values of X/L and θ was selected for each of four sections along the external tank. These sections consisted of (1) model nose section ($0 < X/L \leq 0.25$), (2) intertank section ($0.25 < X/L \leq 0.43$), (3) mid-tank section ($0.43 < X/L \leq 0.725$), and (4) the aft-tank section ($0.725 < X/L \leq 1.0$). The repeatability of measurements from these instruments for each tunnel is presented in Fig. 14. In general, the repeatability is best on the nose section but is good-to-excellent over the complete tank in each tunnel. The distribution of repeatability for all measurements recorded from the repeat runs is presented in Fig. 15 to

quantify the data repeatability for each tunnel. The repeatability in each tunnel was good with 91.6 percent of the measurements in Tunnel A and 97 percent of the measurements in Tunnel C repeating within 14 percent.

With the general level and the repeatability of the data examined in each tunnel, the next step was to investigate how the data compare between tunnels. The data were obtained by using the same model in both tunnels. Only those instruments that were operational in each tunnel could be used in this phase. Once again the measurements were compared for a model attitude of $\alpha = 0$ and $\beta = 0$. The percent variation was defined as the difference between $h(\text{RTT})/h(\text{REF})$ from each tunnel divided by the value in Tunnel C. The distribution of the percent variation of these measurements is presented in Fig. 16. As can be seen, only 62 percent of the measurements compared within 20 percent from tunnel to tunnel. To add more meaning to these data, the range of deviation of each comparable instrument is shown in the symbol legend in Figs. 9a and b. The measurements that did not repeat within ± 30 percent are presented as a solid symbol. Large variations occurred at the lower aft-end of the external tank where the model was outside the Tunnel C test rhombus (see Fig. 6b). Also, large variations ($> \pm 50$ percent) occurred at locations where conduction could be a factor, such as model joints where bulkheads were located or very near large protuberances. The data used in this report were subject to a posttest screening where erroneous and questionable gages were eliminated. However, since only representative samples of the data can be examined, some data that exhibit conduction effects may remain in the complete data set. Several of the instruments located in regions where conduction could be a factor were evaluated by plotting the value of $h(\text{RTT})/h(\text{REF})$ versus time. The value of $h(\text{RTT})/h(\text{REF})$ should be constant if conduction is not present. Conduction was not found to be a significant factor for the small amount of data examined. However, a few gages did exhibit significant conduction, one example is presented in Fig. 17.

A closer look at the data comparison between tunnels can be obtained by examining the heating distributions along specific rays on the external tank. The heating distribution on the nose of the tank near the cable tray ($\theta = 25$ deg) is shown in Fig. 18 for $\alpha = 0$. Comparative data were not available for this ray at angle of attack. Data for the bottom centerline ($\theta = 180$ deg) are shown in Fig. 19 for $\alpha = 0, 5,$ and -5 deg. The data located in regions of noninterference flow are generally in good agreement. Further back on the tank, $X/L > 0.3$, the data agree well except at $\alpha = -5$ deg. Although the data are limited, the trend could be indicative of tunnel interference caused when the model is exposed to the flow in the lower position of the tunnels.

Moving further aft on the external tank, two regions of interference flow were examined at several model attitudes. The heating distribution along the top centerline, in the region of

the orbiter bow-shock impingement, is presented in Fig. 20 for $\alpha = 0, 5,$ and -5 deg. The flow is, of course, very complex in this region as shown in the shadowgraph photographs (Fig. 13). The data at $\alpha = 0$ are in good agreement both upstream and downstream of the bow-shock disturbance. In the region of rapid changes in heating rate, only a slight change in the local flow conditions can change a reading at a discrete point significantly. The data downstream of the disturbance are in good agreement at $\alpha = 0$ but show wider variation at angle of attack. However, this variation does not indicate a trend caused by a tunnel disturbance. The second region of interference flow that was examined is in the region of the forward SRB attach strut ($\theta = 280$ deg). Data for this ray are presented in Fig. 21 for $\alpha = 0, 5,$ and -5 at $\beta = 0$ and $\alpha = 0$ at $\beta = 3$ and -3 deg. Low-temperature ($TT = 740^\circ\text{R}$) data in Tunnel C were not available for $\beta = 3$ and -3 deg. These data are interesting in the data trends that are presented as well as the consistency of all model attitudes. Excellent data comparability can be seen for all of the data between an $X/L = 0.31$ and 0.35 . At $X/L = 0.29$ the Tunnel A data show large deviations from the Tunnel C data. However, downstream of $X/L = 0.35$, large deviations are seen between each set of tunnel data. The consistent data comparability for the majority of the instruments on this ray presents further support to the basic comparability of the data between tunnels. The explanation for the larger deviations, both upstream and downstream of this region, is not evident when separated by data with such good comparability.

The heating distribution between the LO_2 anti-geyser line and the LO_2 feed line ($\theta = 32$ deg) is presented in Fig. 22. Although the instrumentation is widely spaced, these data were of interest because they were located between major protuberances. The comparability between $X/L = 0.4$ and 0.6 is generally good considering the location of the instruments. The poor agreement between tunnels at $X/L = 0.879$ could possibly be a result of the Tunnel A shock impingement.

The heating distribution further aft on the tank for $\theta = 68$ deg is presented in Fig. 23. This instrumentation is near the rear orbiter-to-tank attach strut. The data at $X/L = 0.926$ are just upstream of the SRB/ET aft attach strut. Details of this region are shown in Fig. 8d. Once again, the data are in reasonable agreement and show no major difference between tunnels. The largest difference was just upstream of the SRB/ET attach strut where a rapid increase in heating rate is experienced.

Data from several instruments located on or near the bottom and top centerline of the tank are plotted in Fig. 24 as a function of the temperature difference between the tunnel stagnation temperature, TT , and the gage temperature, TW . A general tendency is for the value of $h(RTT)/hREF$ to decrease slightly (≈ 15 percent) as the temperature difference is reduced to approximately 200°R (see Appendix A for further discussion of this figure).

4.2 WIND TUNNEL-TO-FLIGHT DATA COMPARISON

The flight data used in this comparison were obtained from STS-4 at a trajectory time of 119.8 sec when the fully integrated vehicle had attained $M = 4$. The launch vehicle attitude was $\alpha = 0.75$ and $\beta = -0.58$ deg. The flight Reynolds number based on vehicle length was 14.4×10^6 , whereas the wind tunnel length Reynolds number was 18.6×10^6 . While this 29-percent difference in length Reynolds number is not insignificant, it will be shown that "data adjustment" caused by instrument problems is the dominating consideration.

Data from selected instruments on the model that correspond to DFI locations on the flight vehicle are compared in Fig. 25. The instruments were located primarily on the nose section of the tank. The flight data were reduced according to the procedures in Section 3.4. The uncorrected values of $h(RTT)/hREF$ are plotted along with the corrected values using the Rubesin method as modified by Westkaemper. The corrected flight values are in good agreement with the wind tunnel data (flagged symbols) taken at the same attitude as the flight vehicle. The corrected flight data also compare favorably with data fairings of the Tunnel A and Tunnel C data obtained for a model attitude of $\alpha = 0$ and $\beta = 0$ and a $Re/ft = 4 \times 10^6$. However, the magnitude of the flight data correction degrades the value of the comparison. The method of Rubesin is well recognized, but several assumptions were required to evaluate the correction factor for the flight data.

5.0 CONCLUDING REMARKS

The primary objective of this study was to compare data obtained in Aerothermal Tunnel (C) with a larger temperature driving potential ($900^\circ R$) to data obtained in Tunnel A with a much lower driving potential ($200^\circ R$). Data from each tunnel were compared at several locations on the Shuttle external tank. Based on these comparisons, the following observations are made:

1. The repeatability in each tunnel was good with 91.6 percent of the measurements in Tunnel A and 97 percent of the measurements in Tunnel C repeating within 14 percent.
2. The data between the two tunnels compare well (≈ 10 percent) in regions of noninterference flow, such as the nose section of the external tank. This establishes that no basic differences exist between the tunnels (see Appendix A for further discussion).
3. In regions of interference heating, large deviations (> 50 percent) were found in some measurements that were in close proximity to the good (< 10 percent) measurements. These large deviations may have been caused by

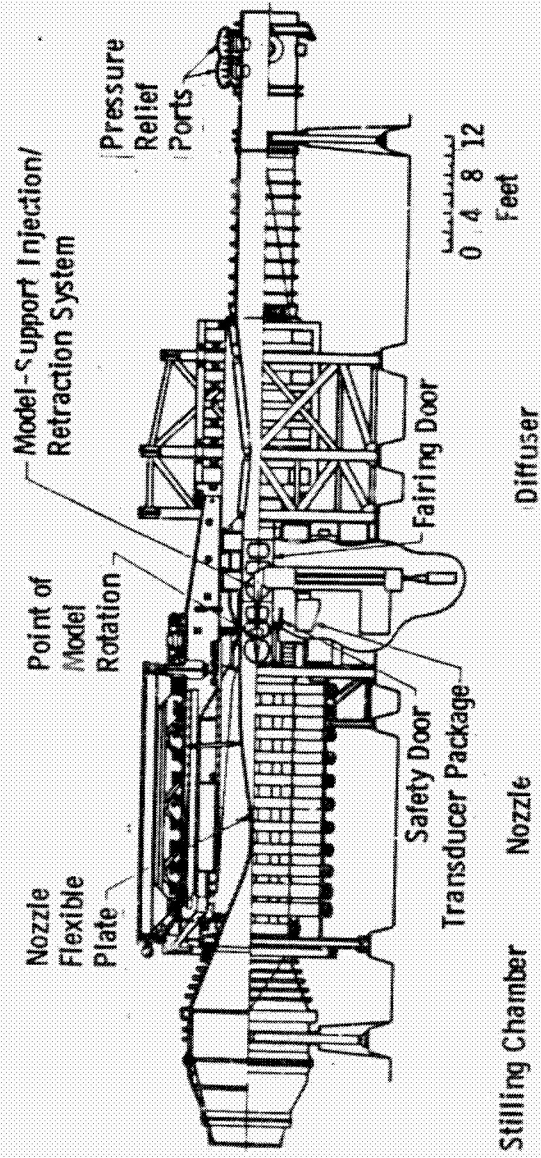
- small shifts in flow interaction regions,
- localized conduction effects,
- tunnel-induced flow disturbances, and
- wall temperature ratio (TW/TT) effects.

A combination of these or other unknown factors resulted in only 62 percent of the measurements comparing within 20 percent from tunnel to tunnel.

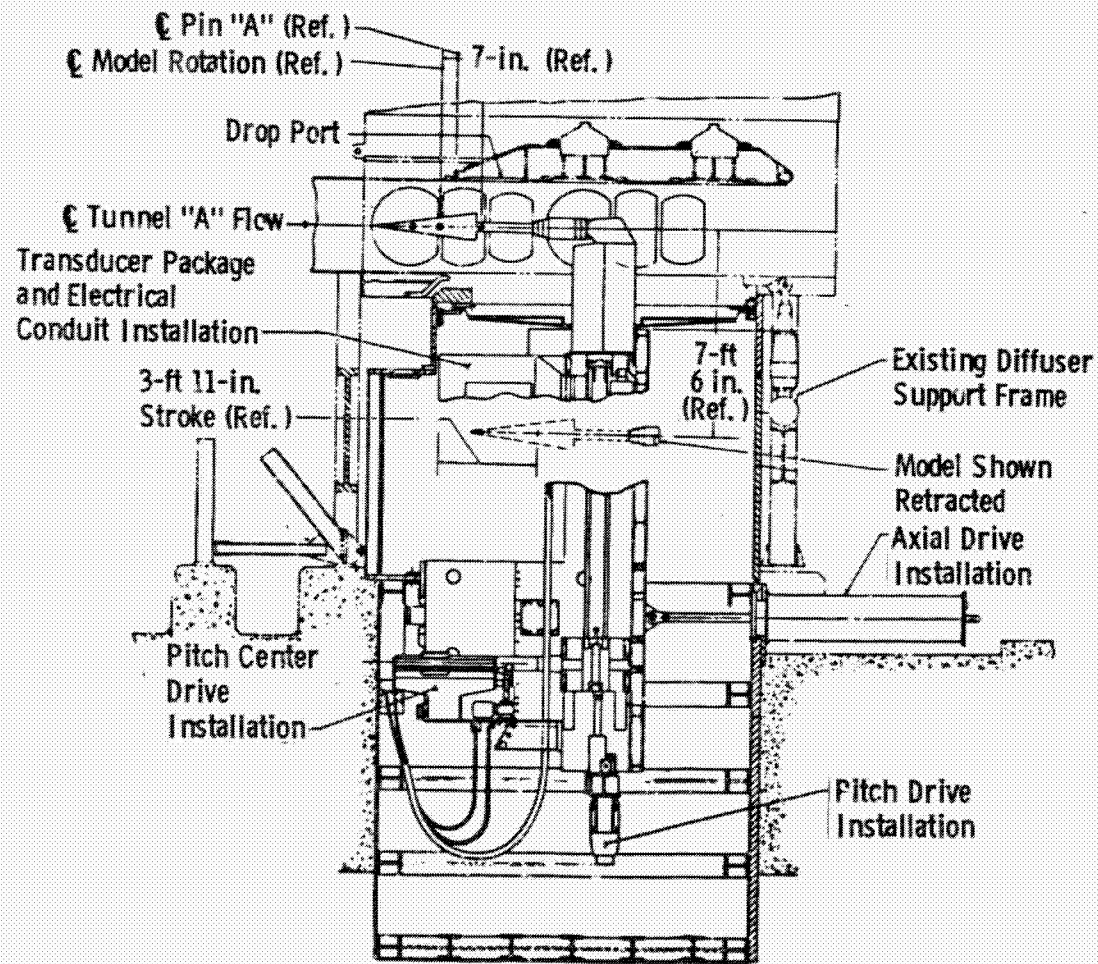
REFERENCES

1. Crain, William K. and Nutt, Kenneth W. "NASA/AEDC External Tank Interference Heating Test." AEDC-TSR-83-V2 (AD-A131688), December 1982.
2. Crain, William K. and Nutt, Kenneth W. "NASA/Rockwell International IH-97 Space Shuttle Heating Test." AEDC-TSR-82-V37 (AD-A128063), December 1982.
3. Boudreau, A. H. "Performance and Operational Characteristics of AEDC/VKF Tunnels A, B, and C." AEDC-TR-80-48 (AD-A102614), July 1981.
4. Hilsch, R. "The Use of the Expansion of Gases in a Centrifugal Field as a Cooling Process." *The Review of Scientific Instruments*, Vol. 18, No. 2, February 1947.
5. Strike, W. T., Jr. "Calibration and Performance of the AEDC/VKF Tunnel C, Mach Number 4, Aerothermal Wind Tunnel." AEDC-TR-82-6 (AD-A116279), June 1982.
6. Kidd, C. T. "A Durable, Intermediate Temperature, Direct Reading Heat Flux Transducer for Measurements in Continuous Wind Tunnels." AEDC-TR-81-19 (AD-A107729), November 1981.
7. Nutt, K. W. and Martindale, W. R. "Heat-Transfer Tests of a 0.0175-Scale Model of the Space Shuttle at Mach Numbers 2.5, 3.5, 4.5, and 5.5." AEDC-TR-75-153 (AD-A025080), June 1976.
8. Hulsey, D. R. and Praharaj, S. C. "STS-4 Raw Measured Data for the Space Shuttle External Tank." Remtech, Inc. RTN 041-12, July 1982.
9. Rubesin, M. W. "The Effect of an Arbitrary Surface Temperature Variation Along a Flat Plate on the Convective Heat Transfer in an Incompressible Turbulent Boundary Layer." NACA TN 2345, April 1951.

10. Bachmann, R. C., Chambers, J. T., and Geidt, W. H. "Investigation of Surface Heat-Flux Measurements with Calorimeters." *ISA Transactions*, Vol. 4, No. 2, April 1965, pp. 143-151.
11. Westkaemper, J. C. "On the Error in Plug-Type Calorimeters Caused by Surface-Temperature Mismatch." *Journal of the Aerospace Sciences*, Vol 28, No. 11, November 1961, pp. 907-909.
12. DeJarnette, Fred R. "Calculations of Inviscid Surface Streamlines on Shuttle Type Configurations, Part I - Description of Basic Method." NASA CR-111921, August 1971.
13. DeJarnette, Fred R. and Jones, Michael H. "Calculations of Inviscid Surface Streamlines and Heat Transfer on Shuttle Type Configurations, Part 2 - Description of Computer Program." NASA CR-111922, August 1971.
14. DeJarnette, Fred R. "Calculation of Heat Transfer on Shuttle-Type Configurations Including the Effects of Variable Entropy at the Boundary Layer Edge." NASA CR-112180, October 1972.



a. VKF Tunnel A
Figure 1. Schematic view of Tunnel A.



b. Model injection system
Figure 1. Concluded.

OF FOUR QUARTS

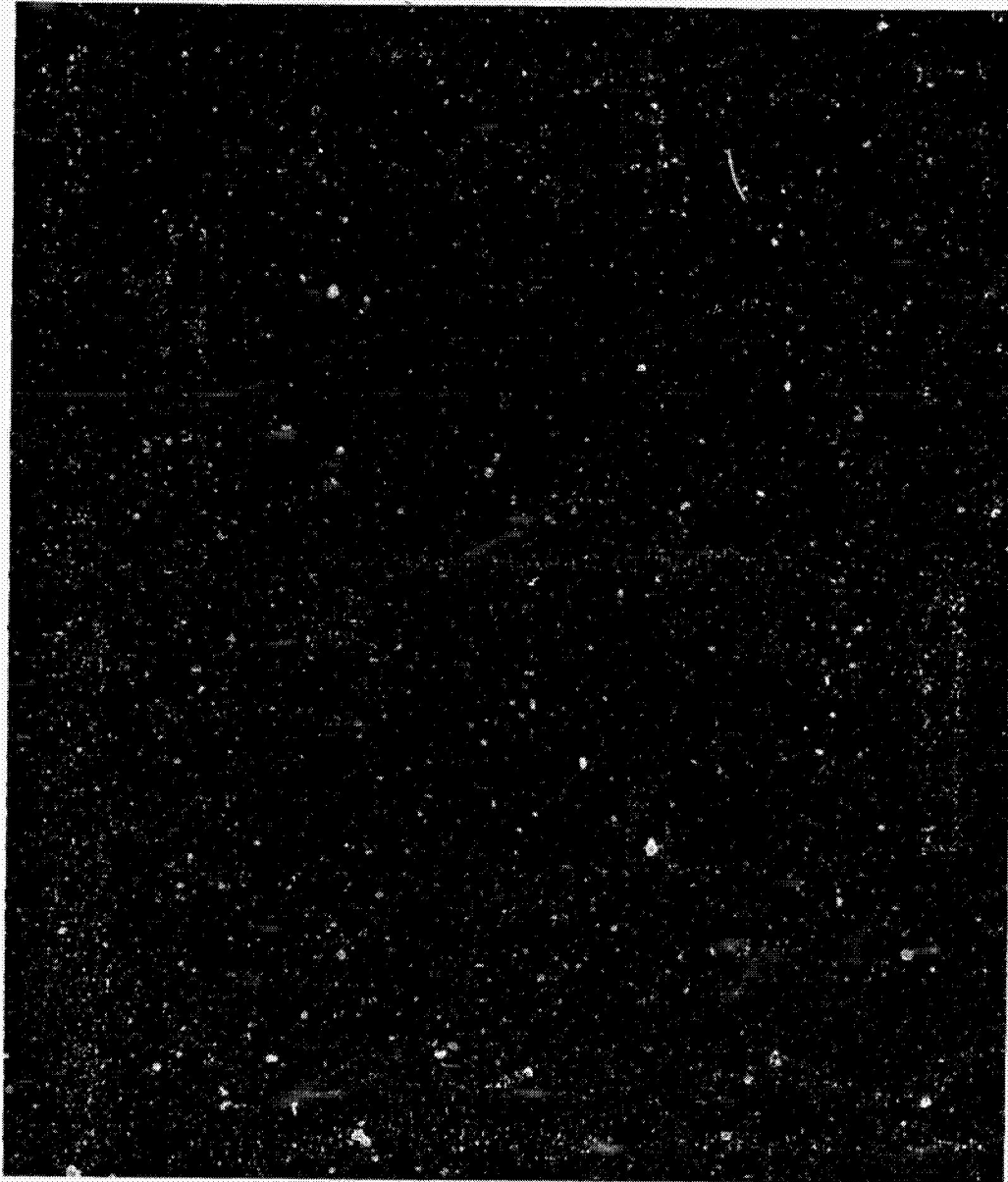


Figure 2. Tunnel A model-cooling manifold.

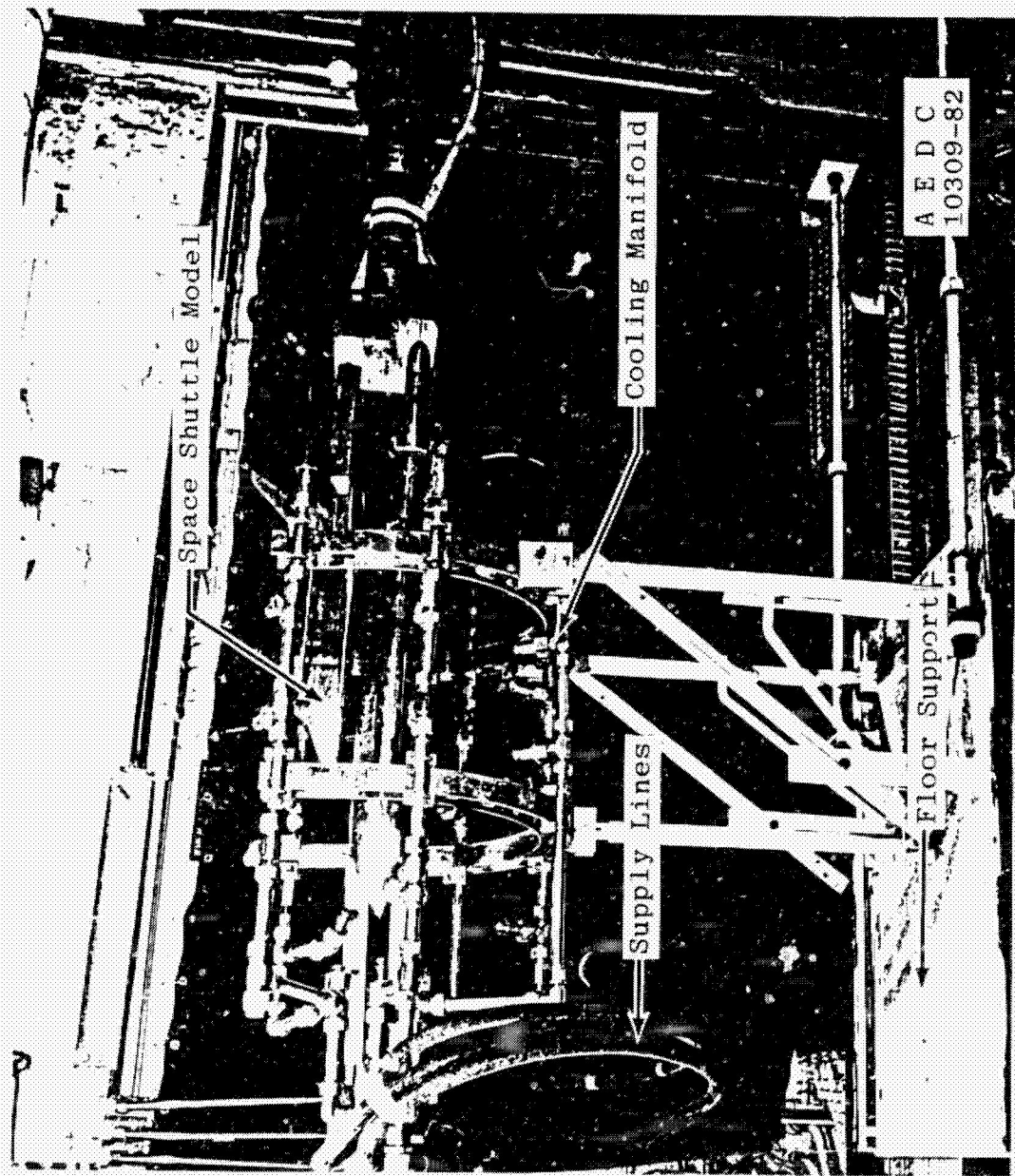
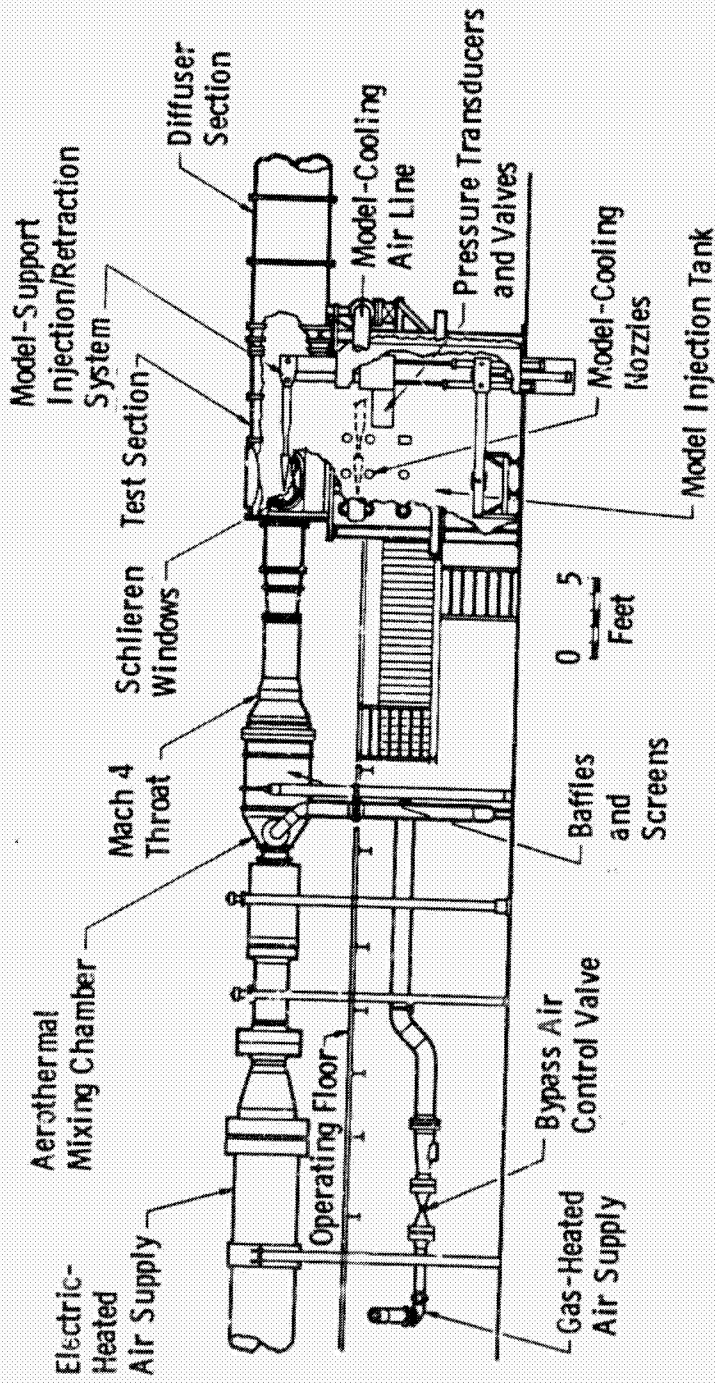
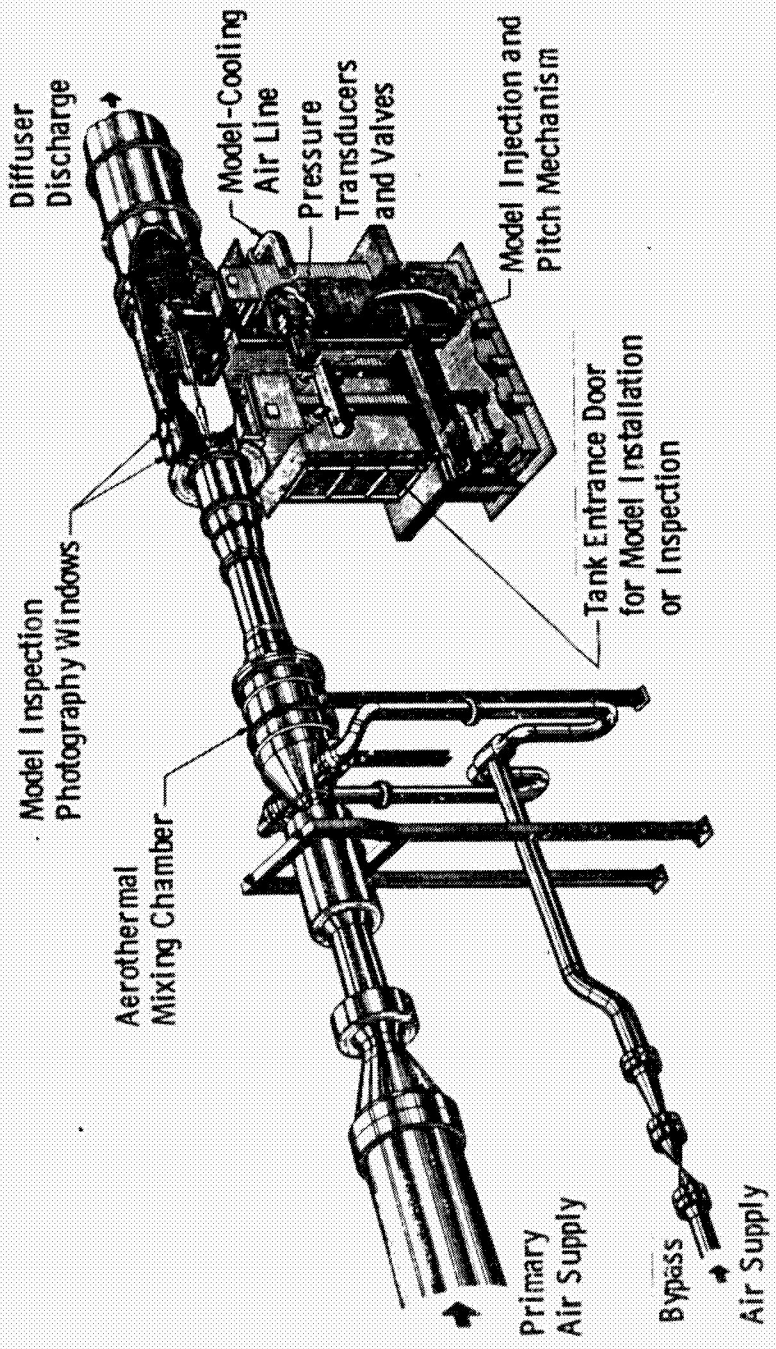


Figure 2. Tunnel A model-cooling manifold.
TR-84-3

10170



a. Tunnel assembly
 Figure 3. Tunnel C Mach: 4.0 configuration.



b. Perspective of tunnel test section area
Figure 3. Concluded.

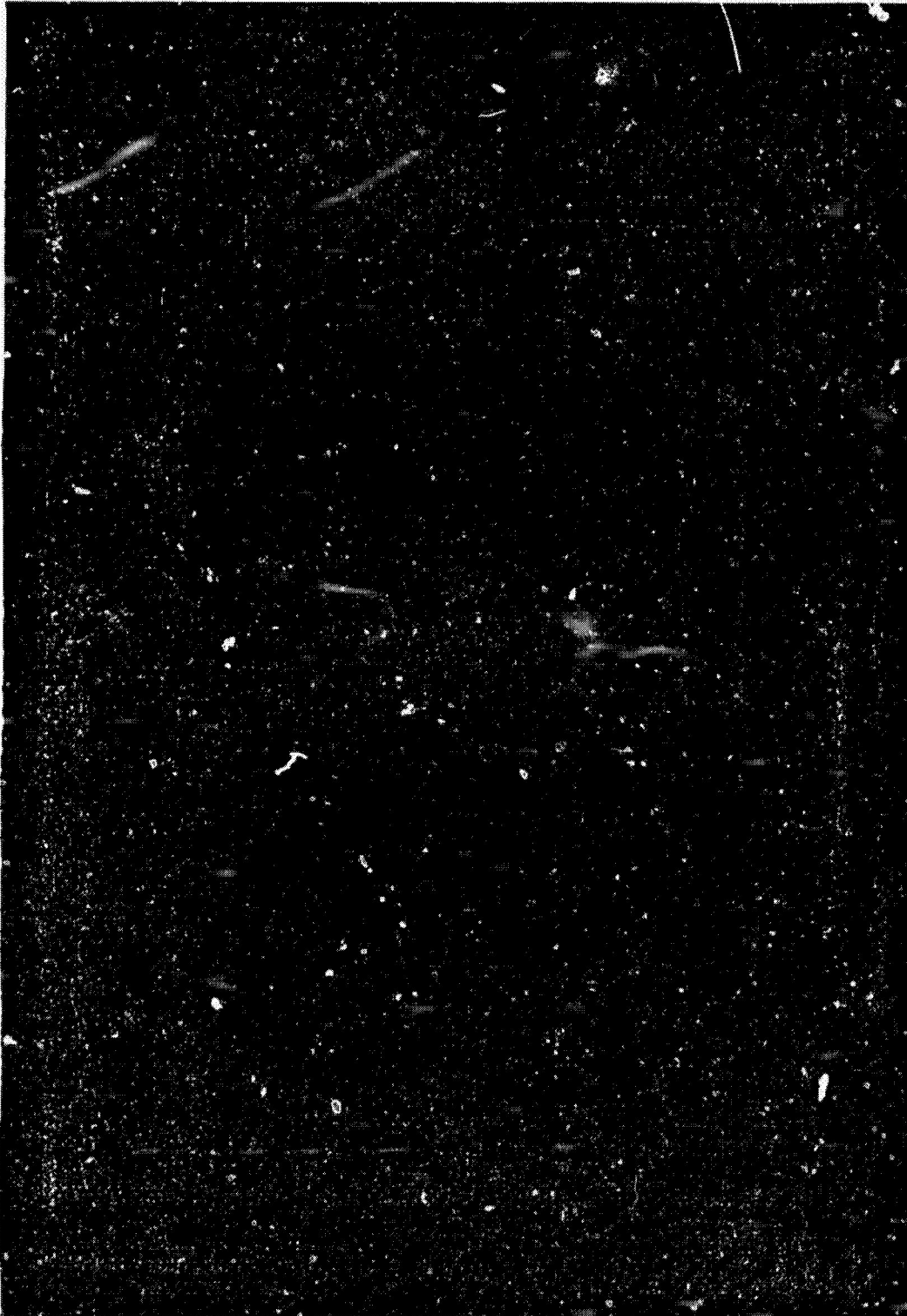
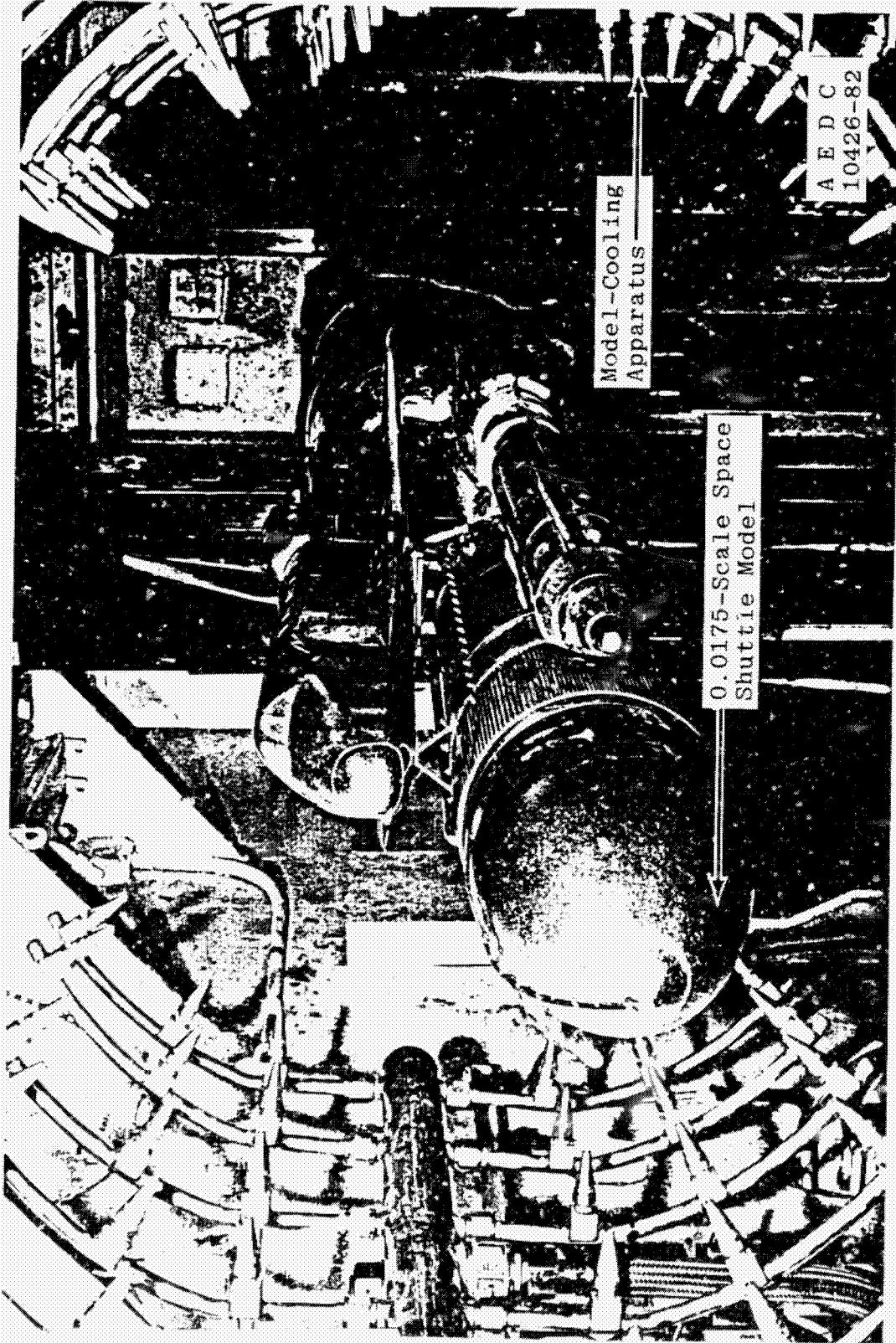


Figure 4. Tunnel C model-cooling manifold.



OF POOR QUALITY

A E D C
10426-82

Model-Cooling
Apparatus

0.0175-Scale Space
Shuttle Model

10201

Figure 4. Tunnel C model-cooling manifold.
TR-84-3

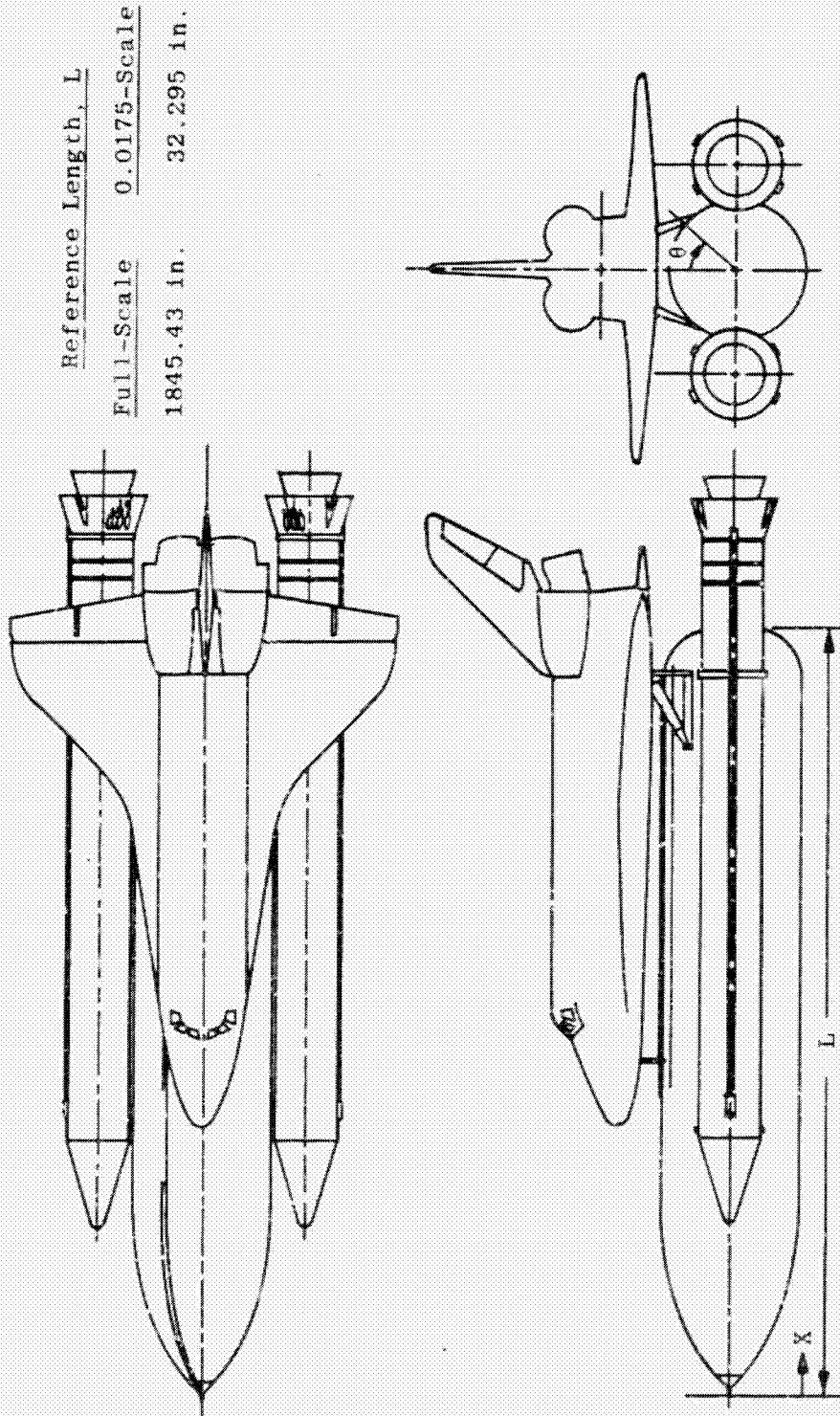
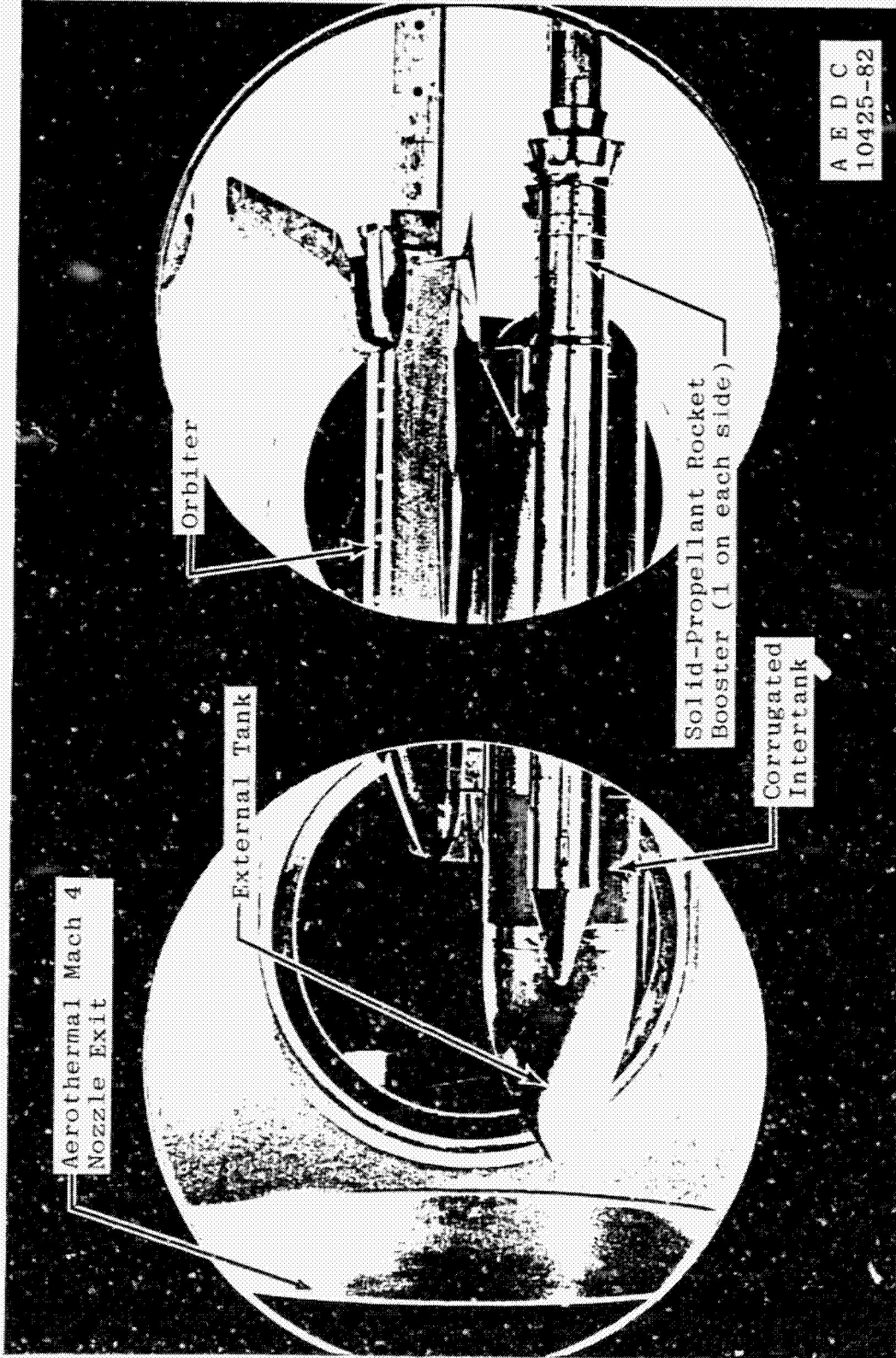


Figure 5. Model sketch.

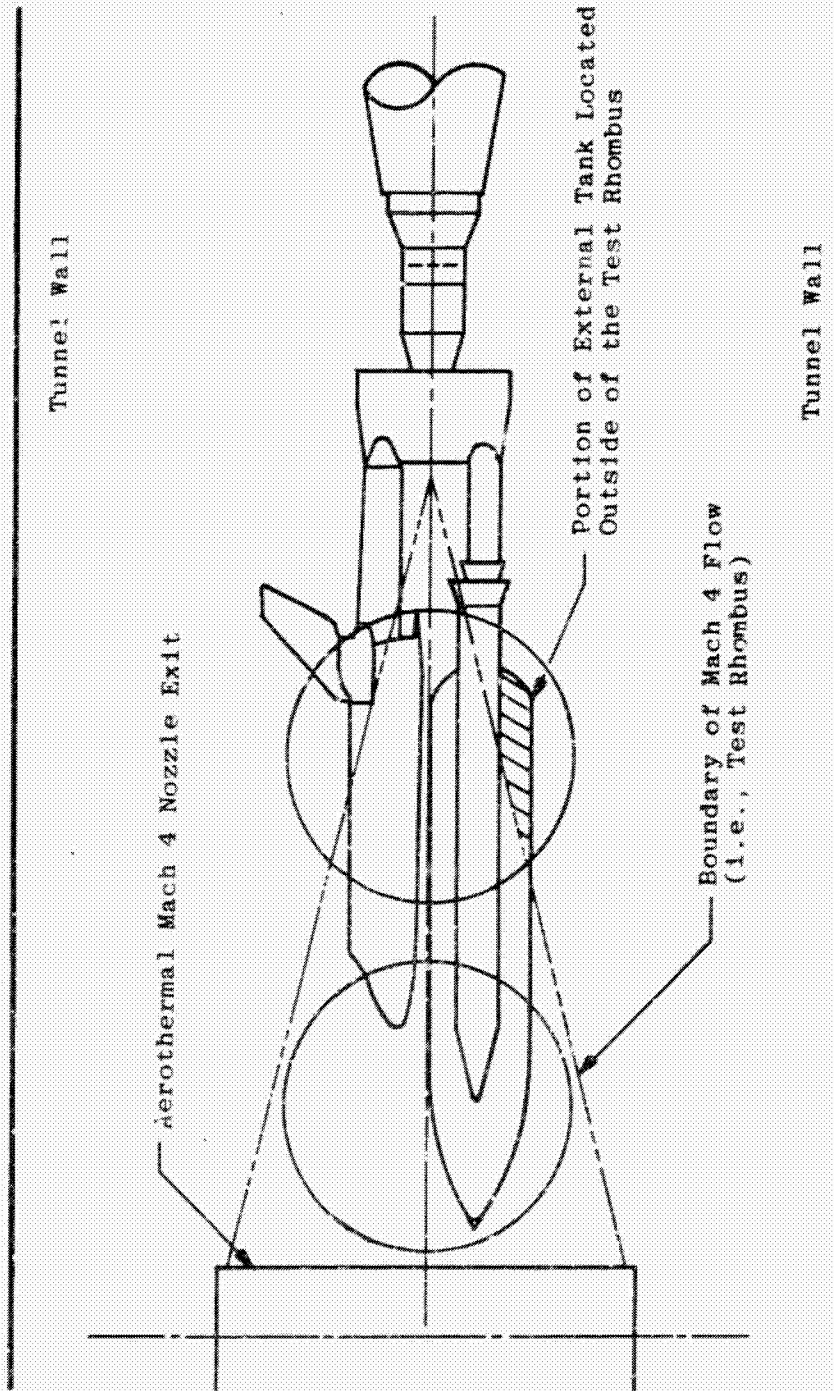


a. Installation photograph
Figure 6 Model installation in Aerothermal Tunnel (C).

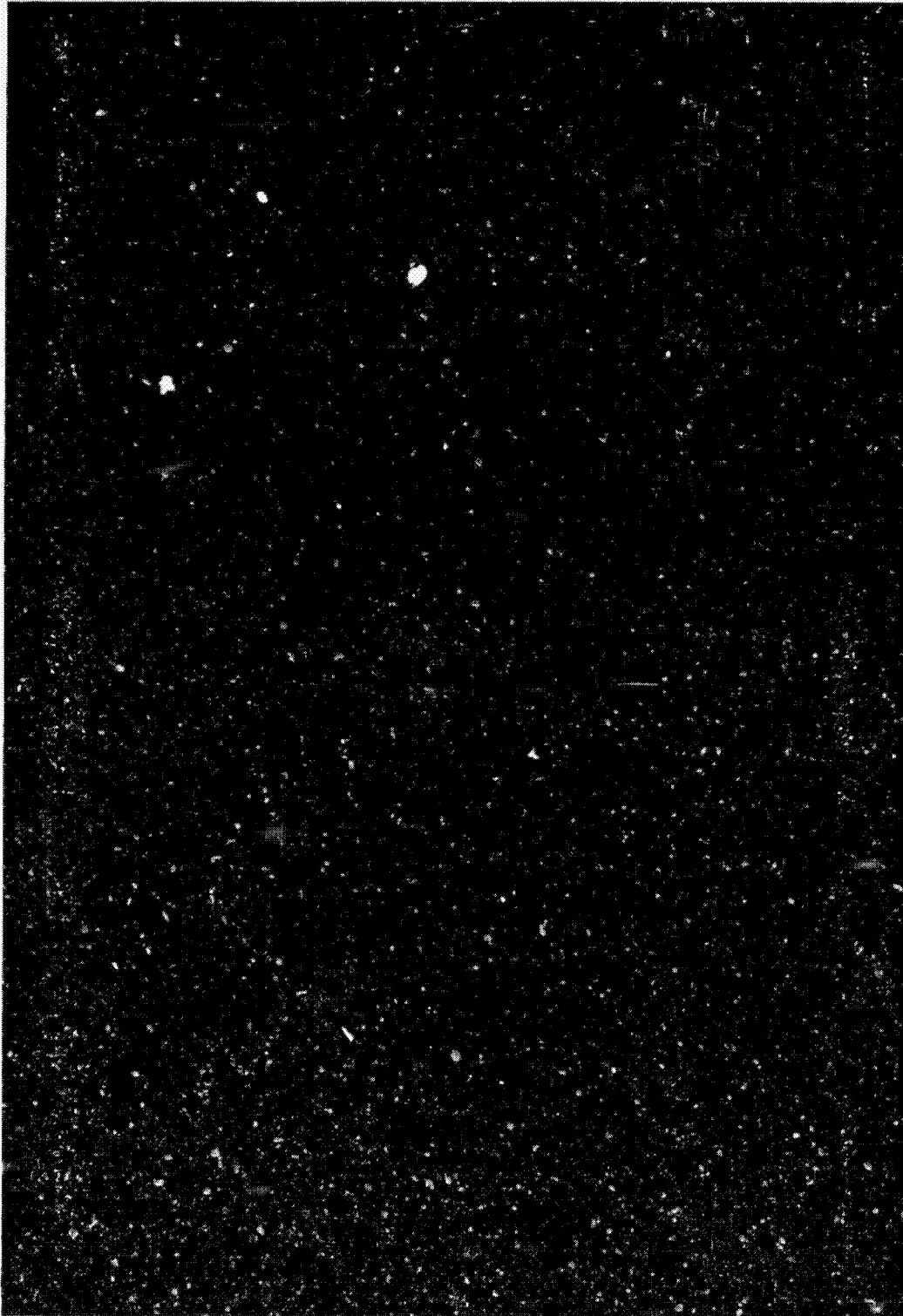


a. Installation photograph
Figure 6. Model installation in Aerothermal Tunnel (C).
TR-84-3

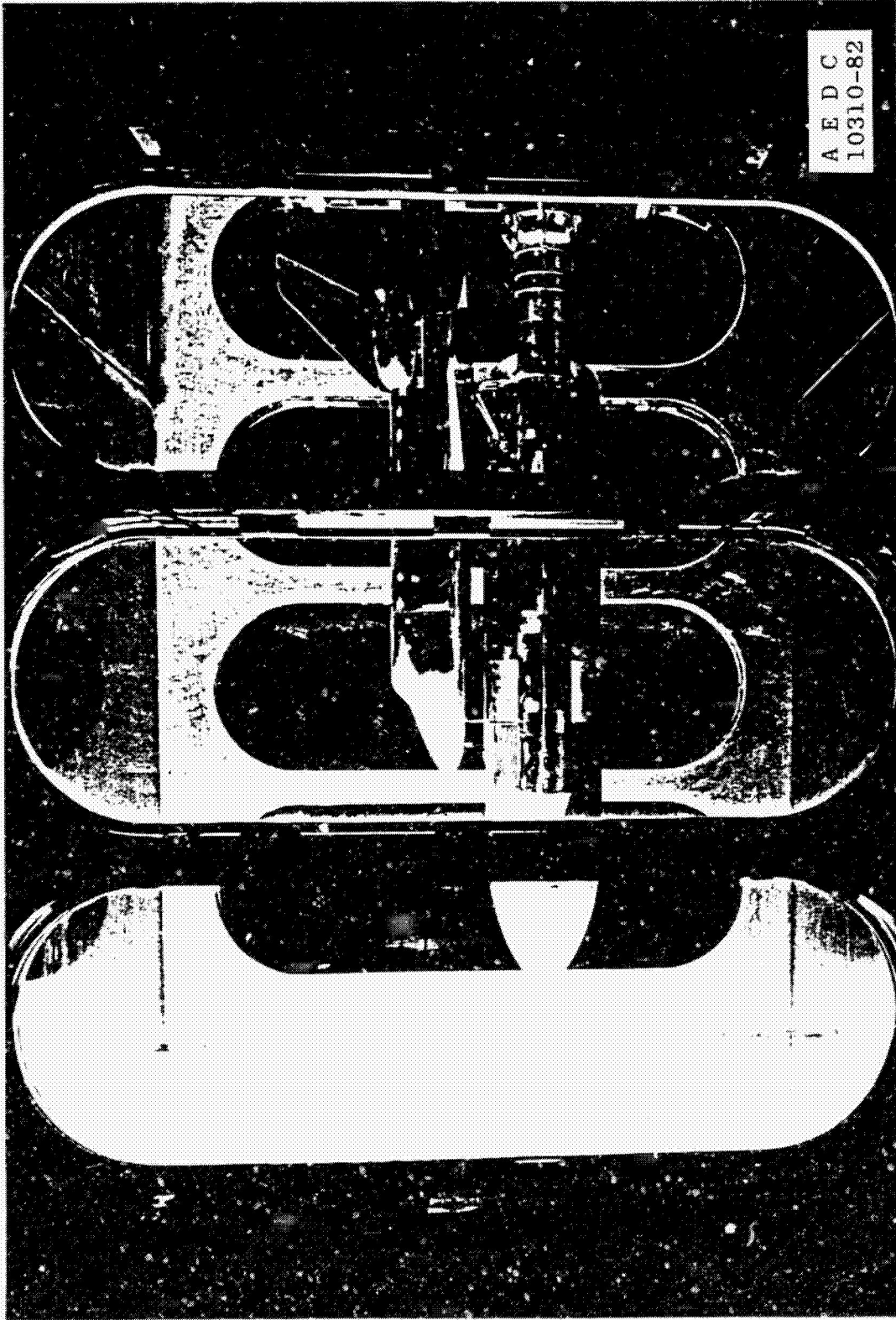
45910



b. Installation sketch
Figure 6. Concluded.

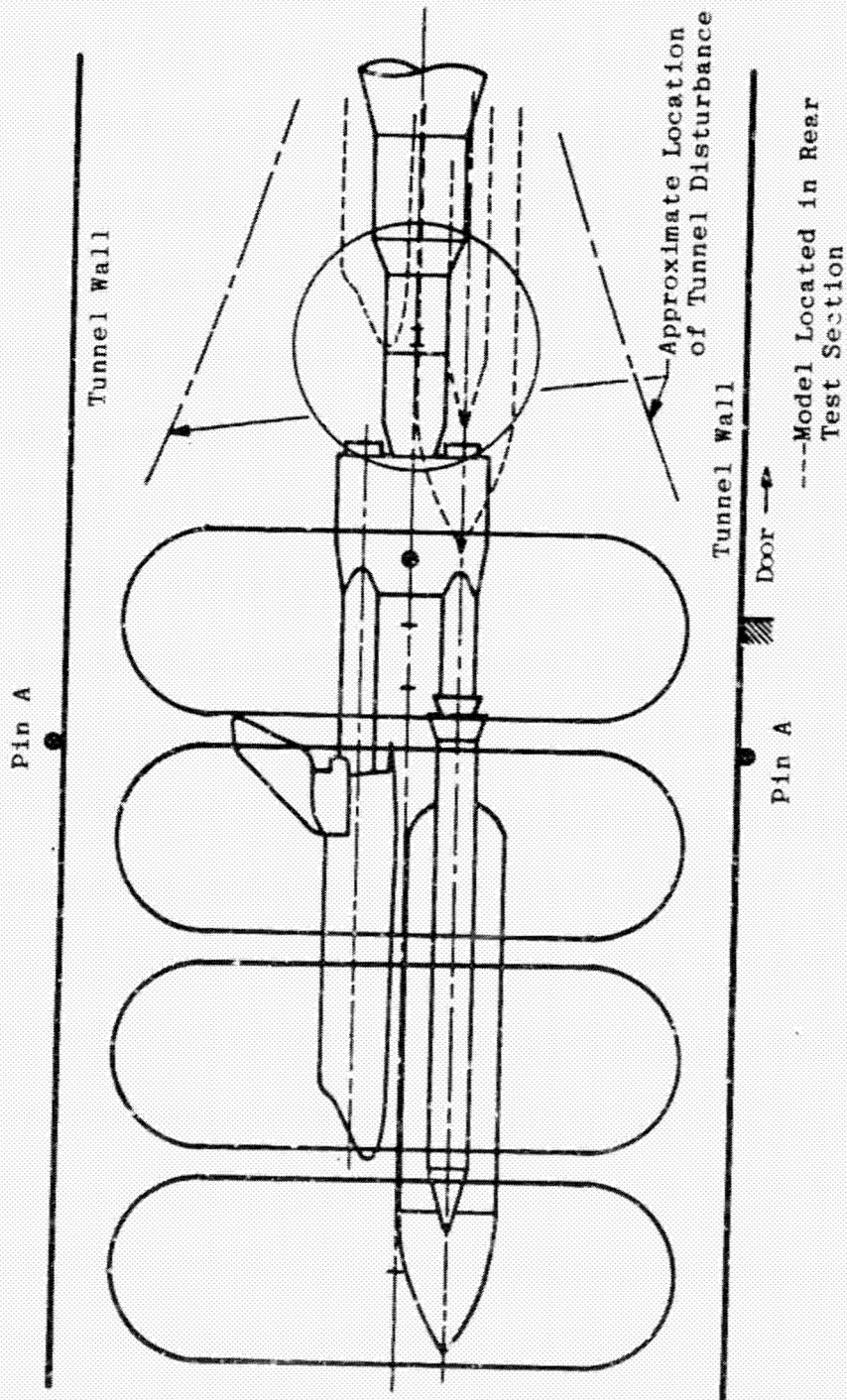


a. Installation photograph
Figure 7. Model installation in Tunnel A.

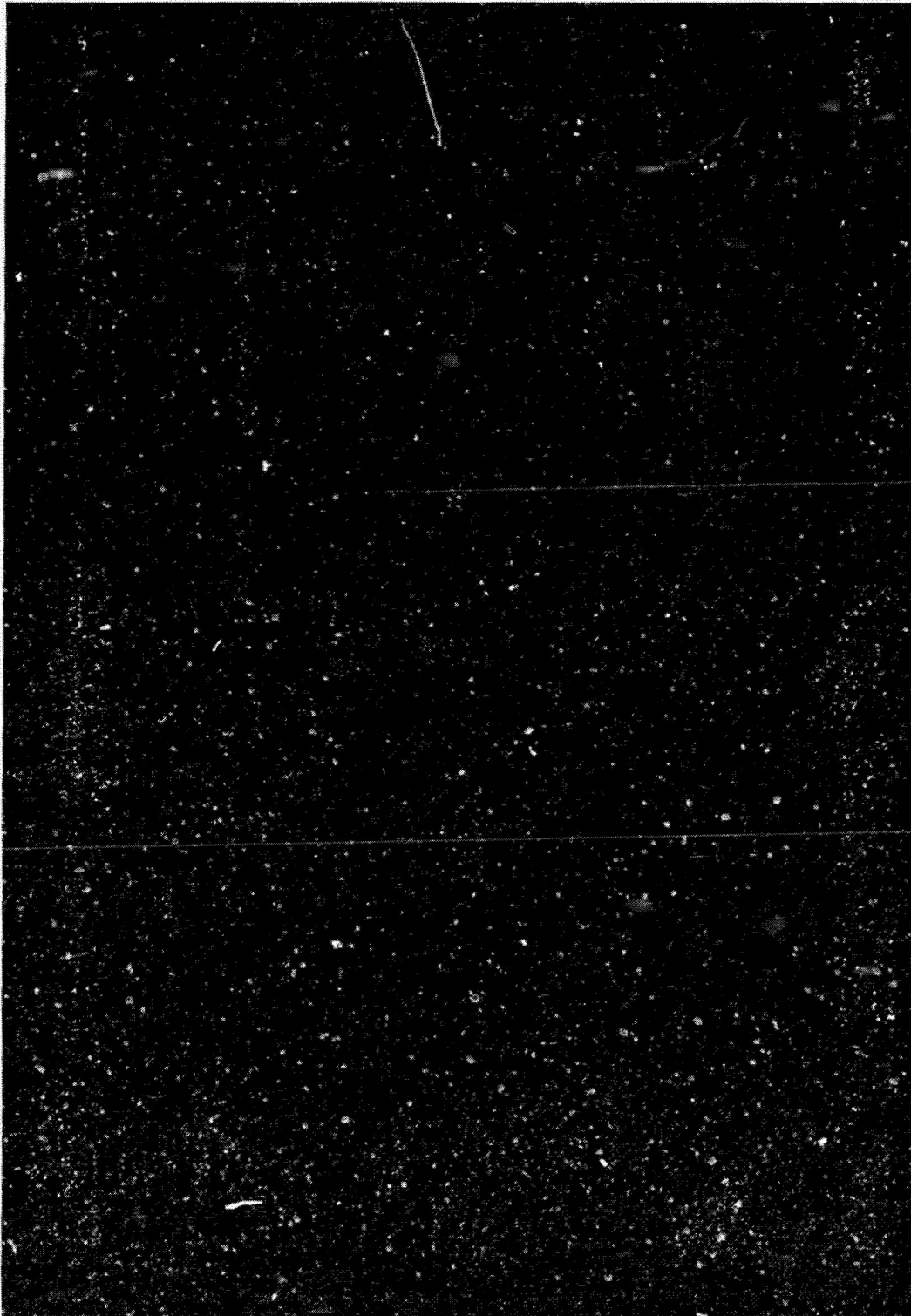


a. Installation photograph
Figure 7. Model installation in Tunnel A.
TR-84-3

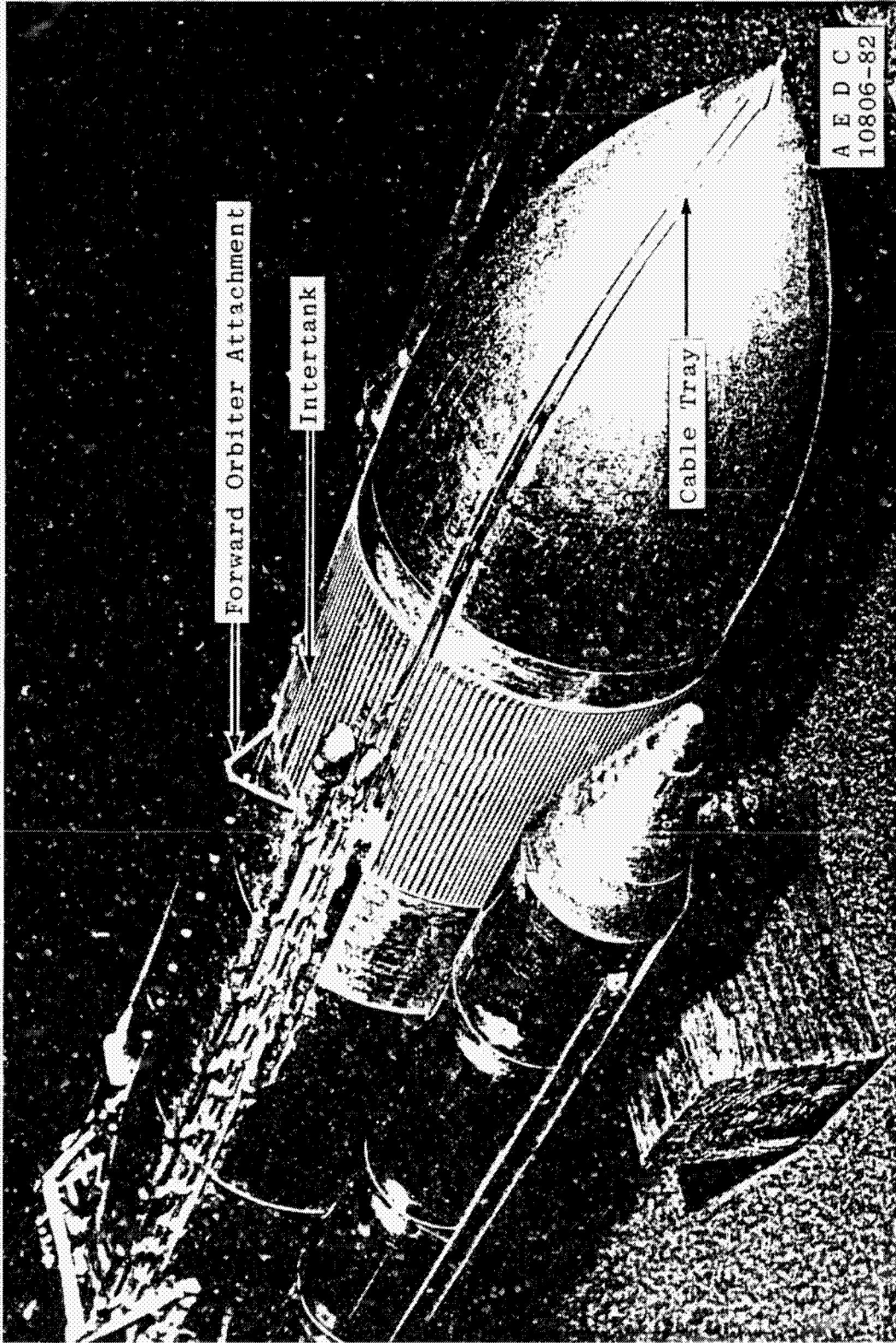
10097



b. Installation sketch
Figure 7. Concluded.

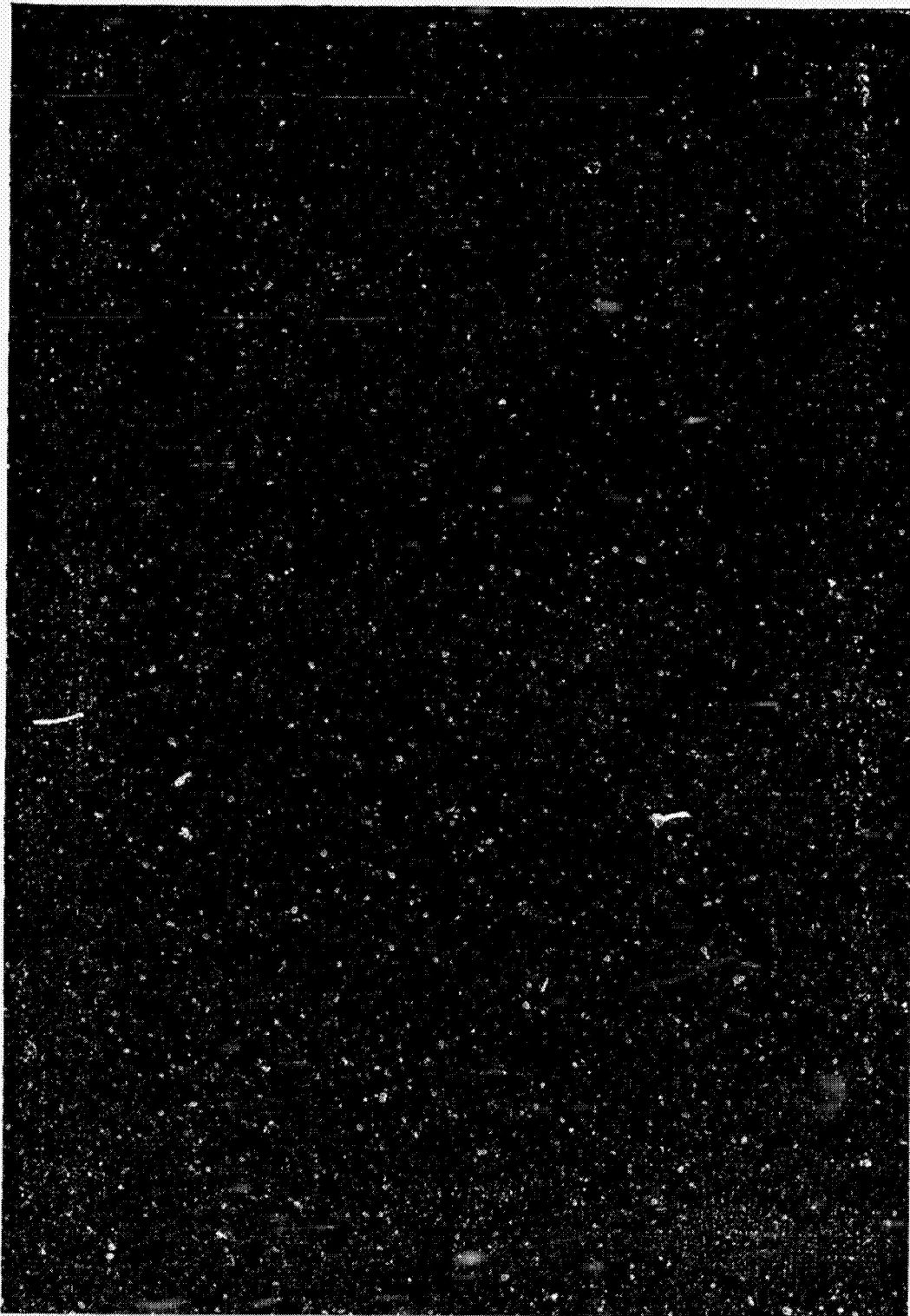


a. Right side of nose, intertank, and mid-tank section
Figure 8. Details of 0.0175-scale external tank.



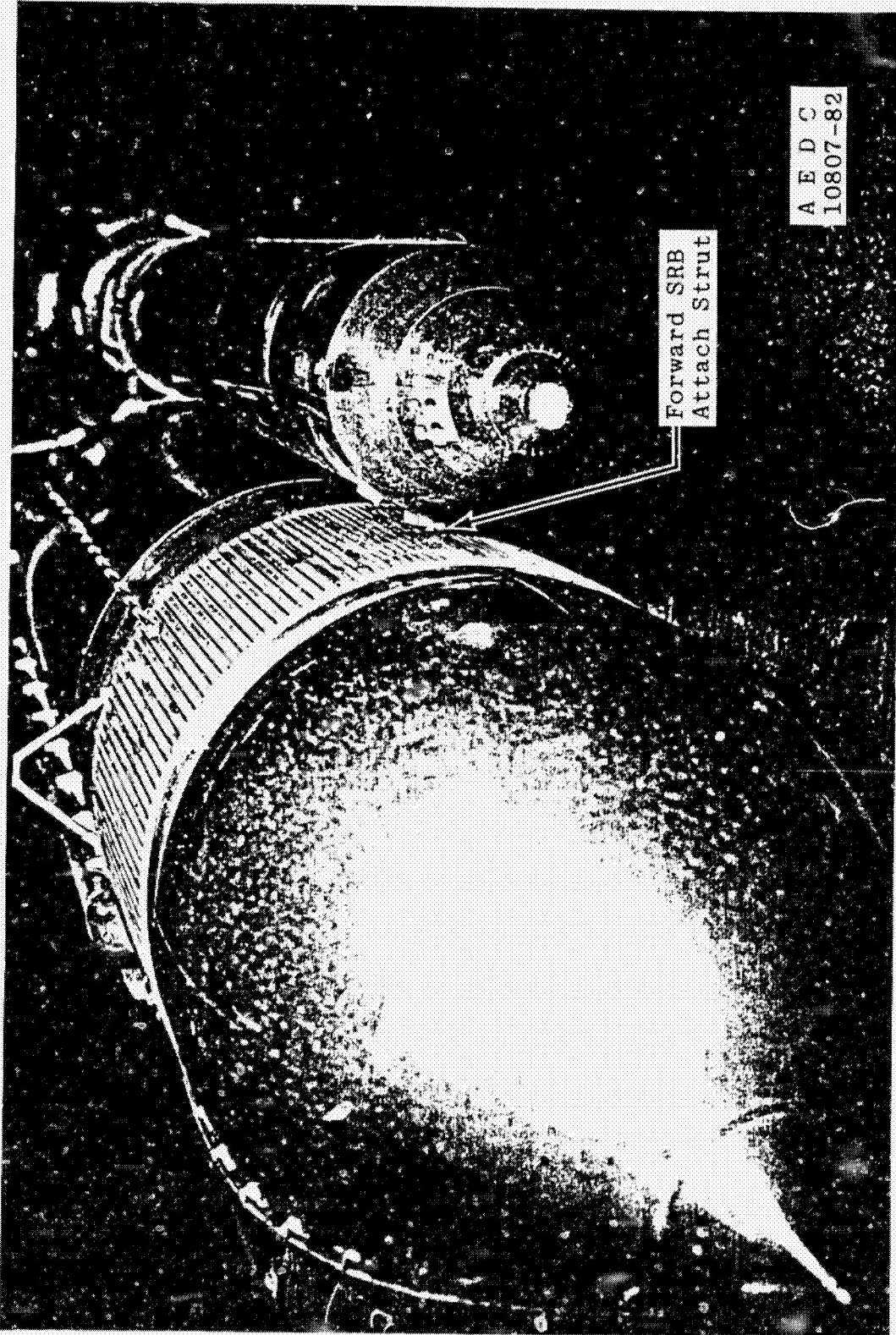
a. Right side of nose, intertank, and mid-tank section
Figure 8. Details of 0.0175-scale external tank.
TR-84-3

10090



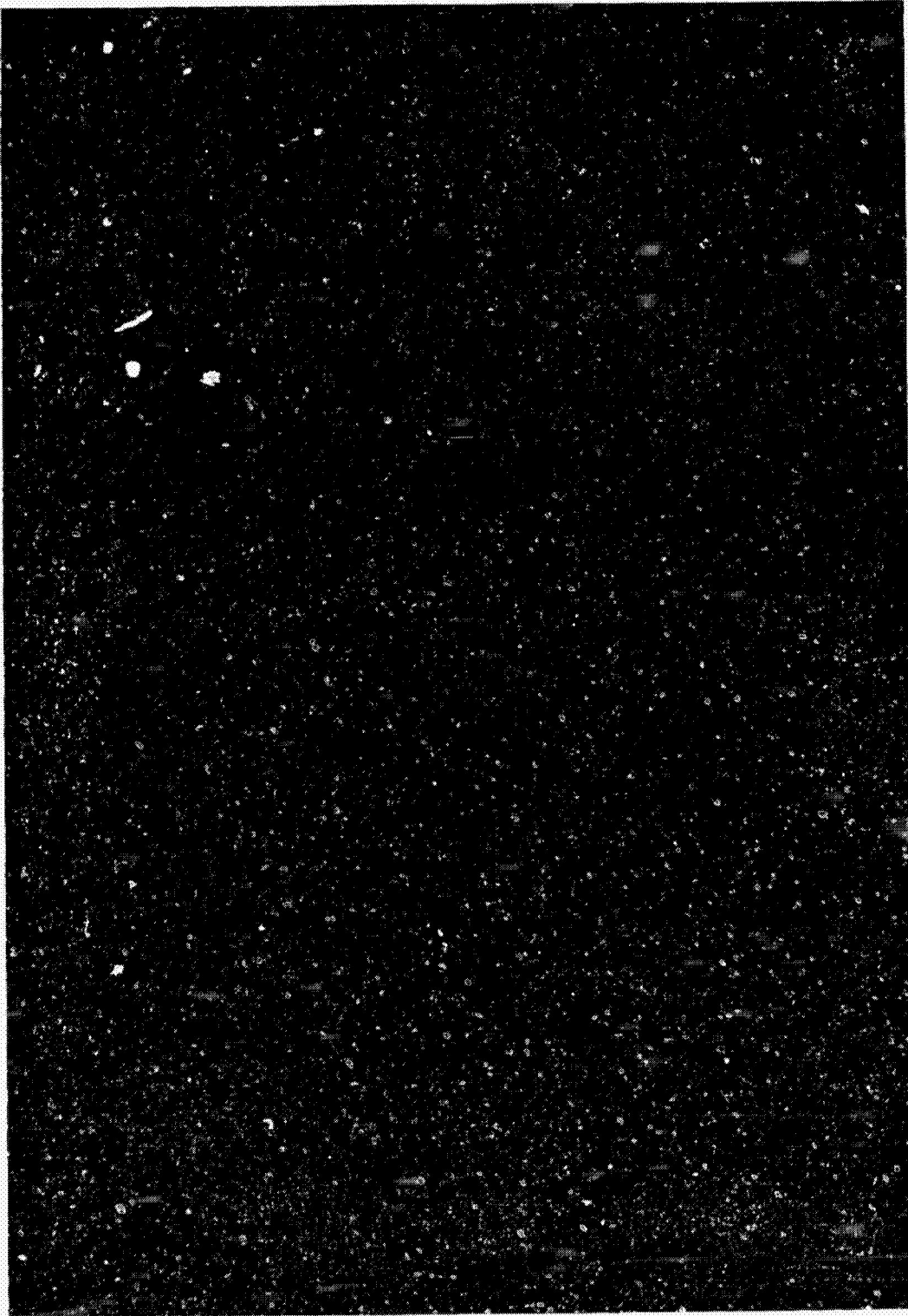
b. Left side of nose and intertank section.
Figure 8. Continued.

ORIGINAL SOURCE
OF PGOR QUALITY



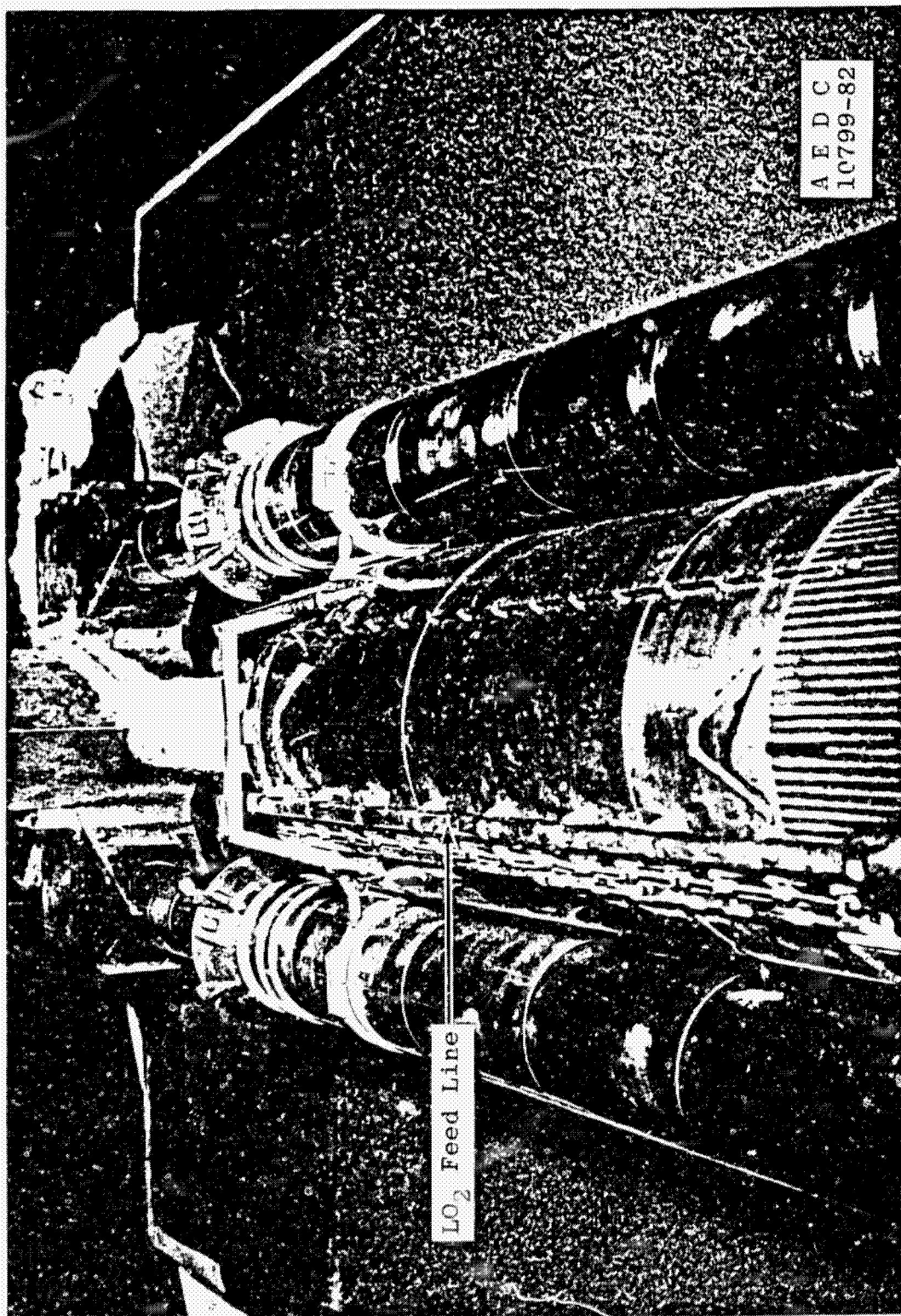
b. Left side of nose and intertank section
Figure 8. Continued. TR-84-3

11600



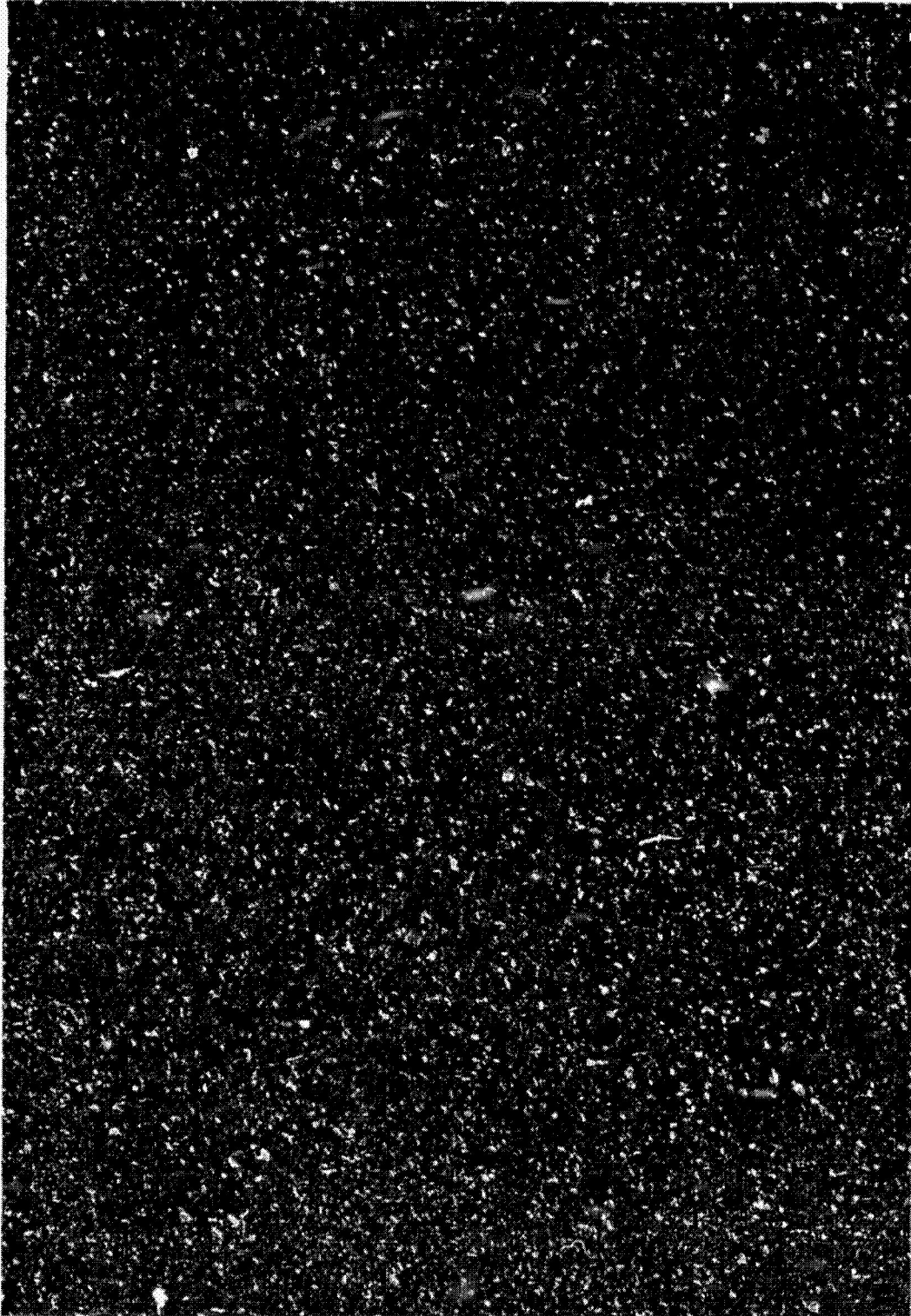
c. Mid- and aft-tank section
Figure 8. Continued.

OF POOR QUALITY



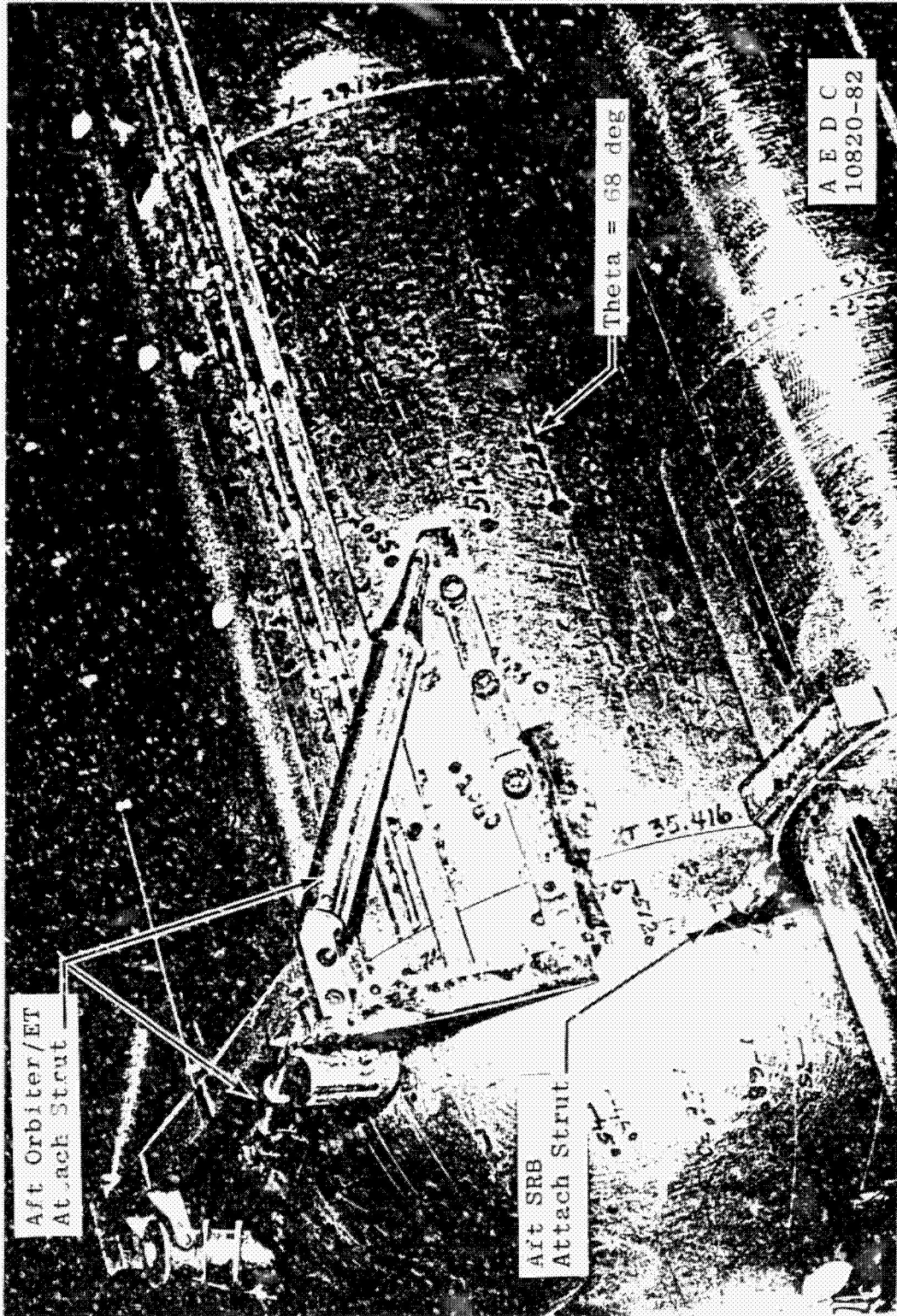
c. Mid- and aft-tank section
Figure 8. Continued. TR-84-3

100%



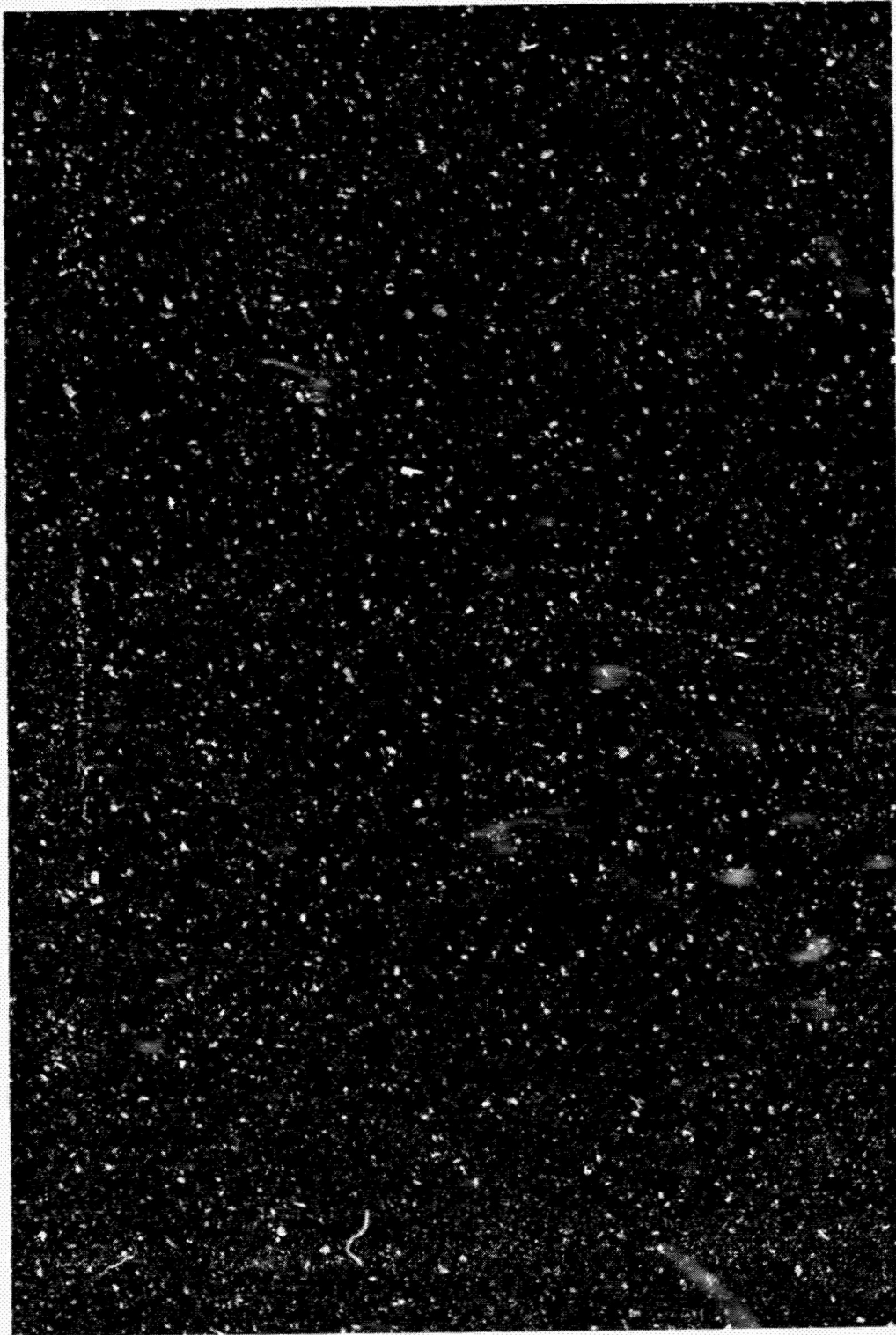
d. Right side of aft-tank section
Figure 8. Continued.

SECTION
OF POOR QUALITY

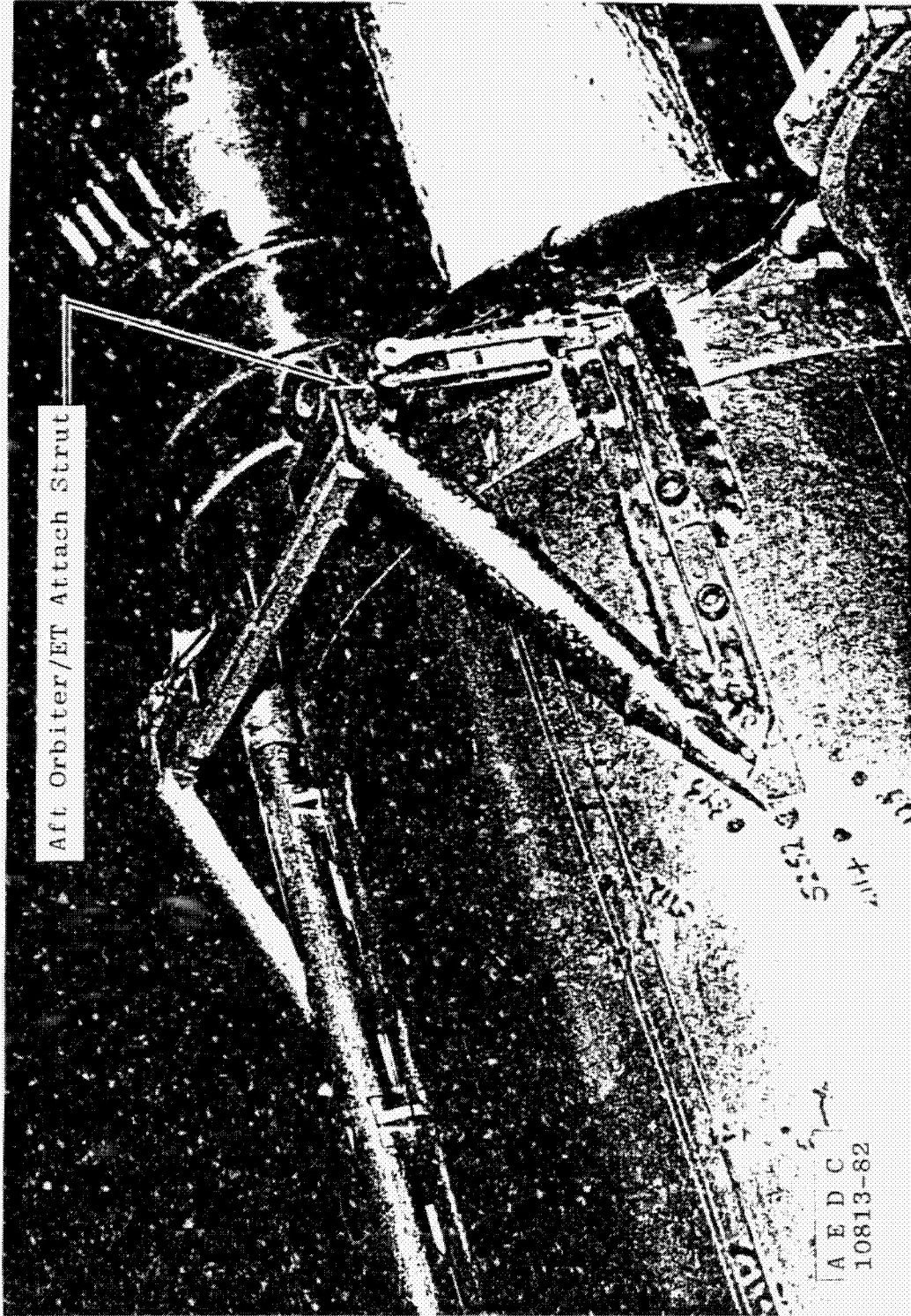


d. Right side of aft-tank section
Figure 8. Continued.

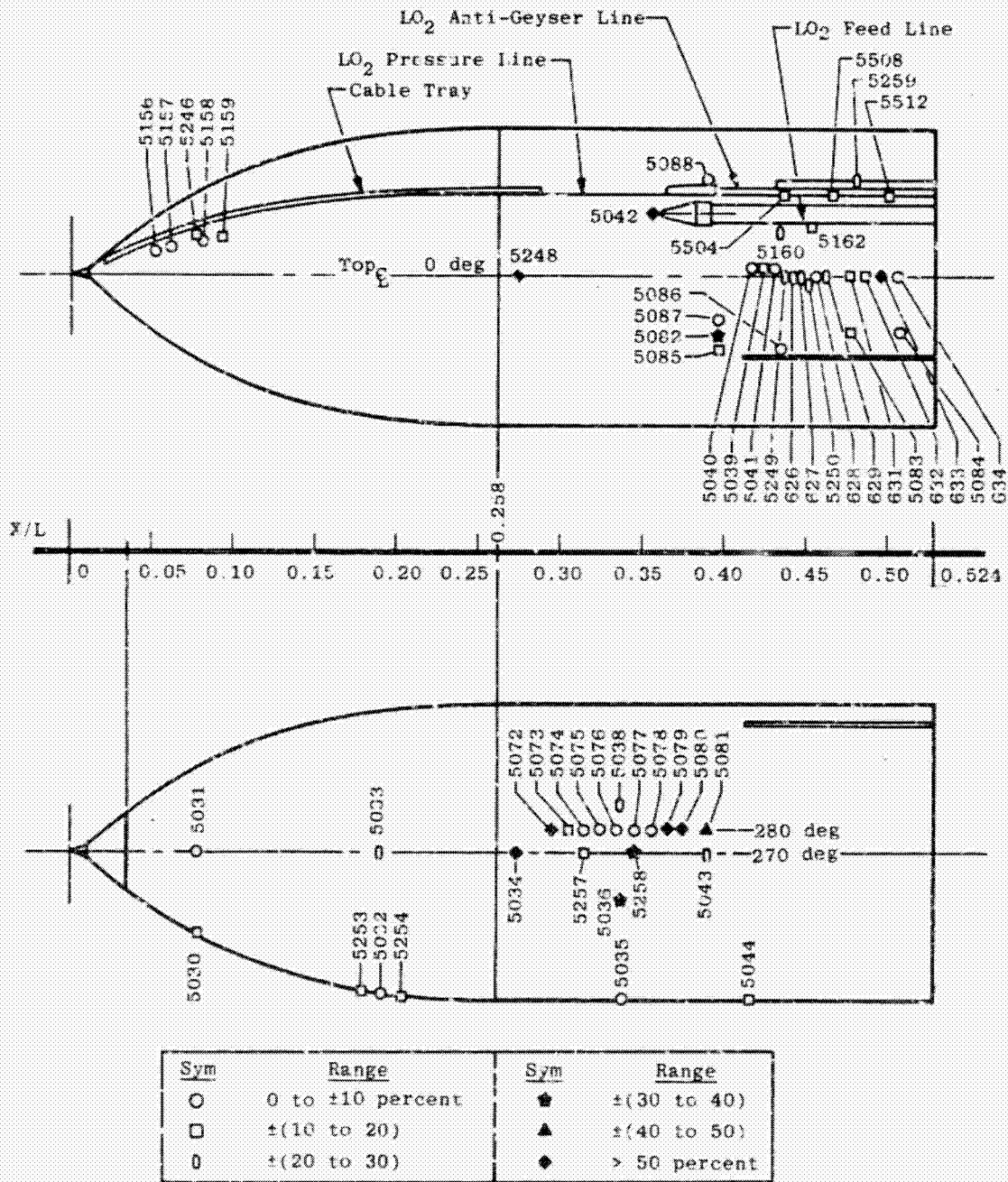
109c



c. Left side of aft-tank section
Figure 8. Concluded.

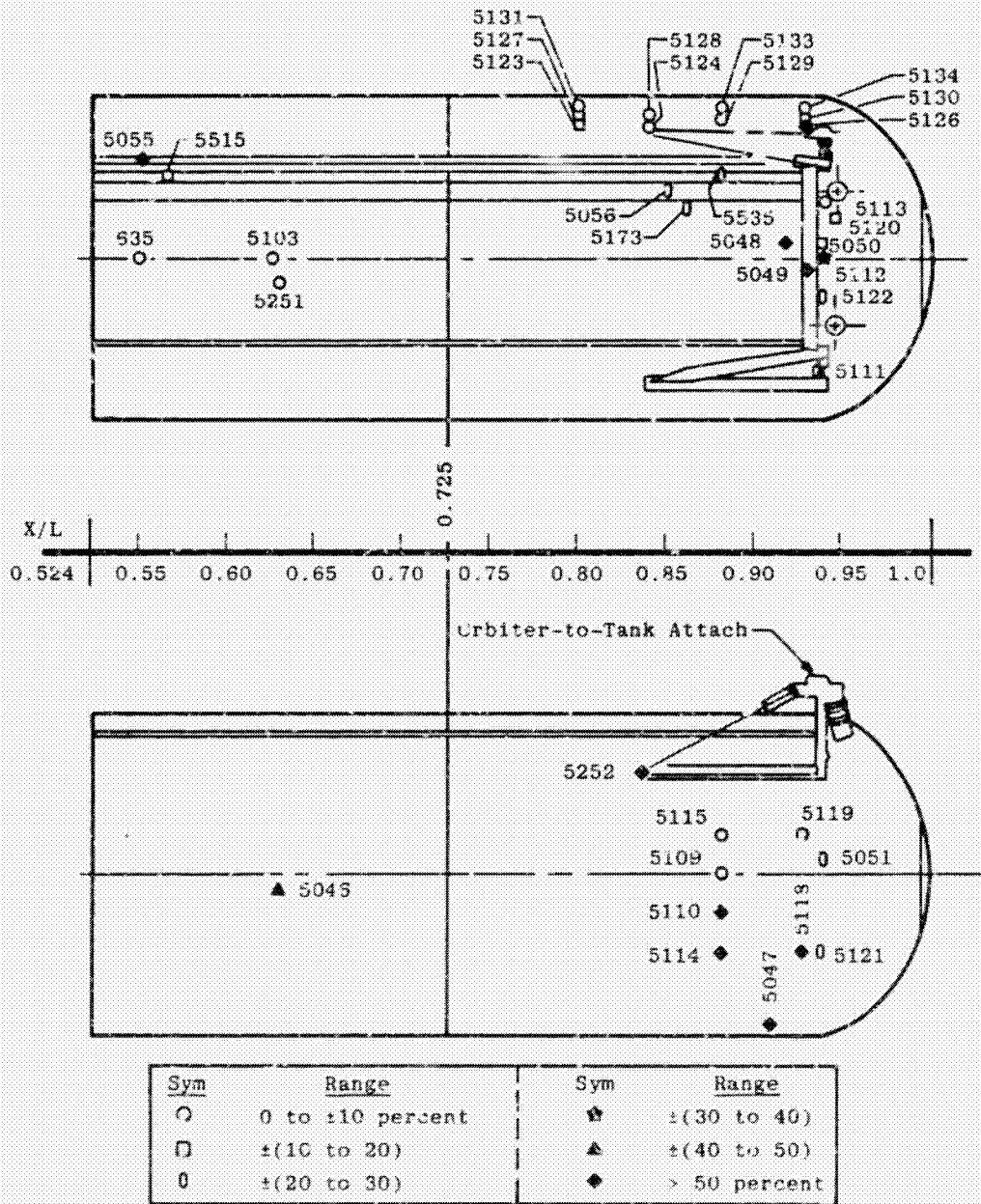


e. Left side of aft-tank section
Figure 8. Concluded.



a. Forebody

Figure 9. Model instrumentation locations.



b. Aft-body
Figure 9. Concluded.

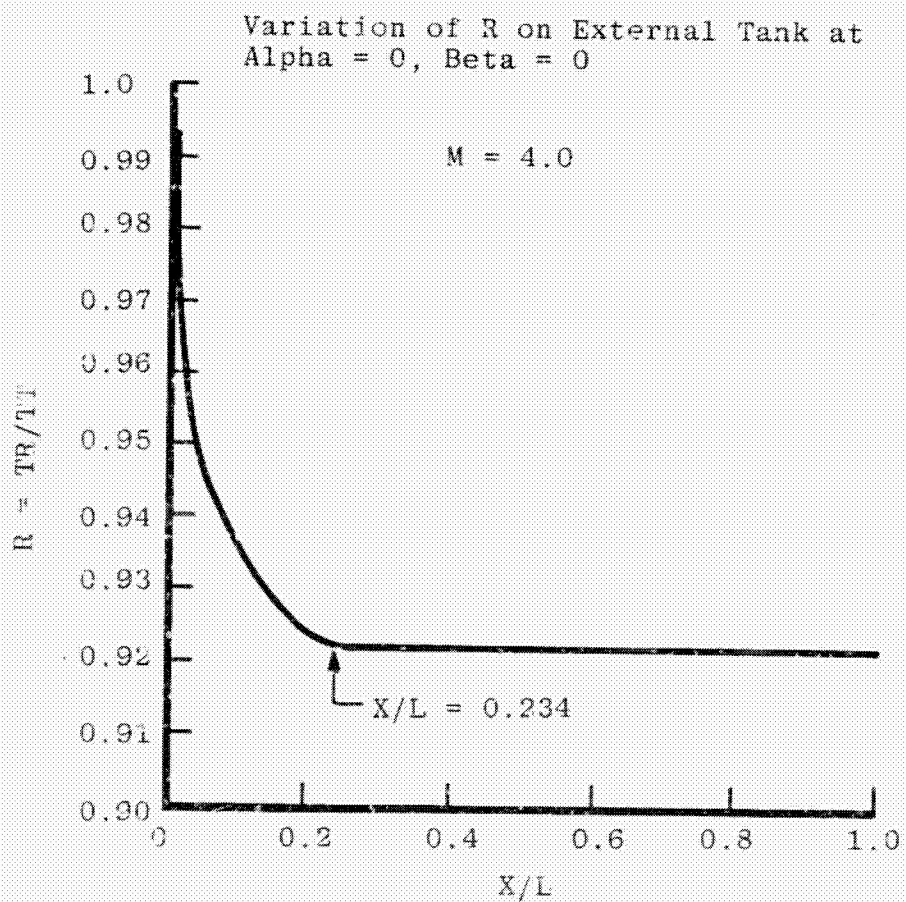


Figure 10. Variation of R on external tank.

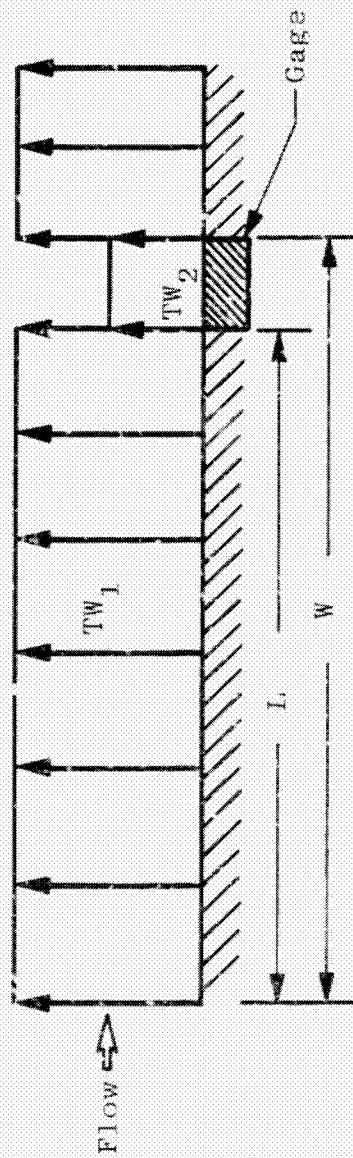


Figure 11. Temperature profile caused by presence of gage in an insulating material.

Sym	Source	TT, °R	hREF
○	Tunnel A	740	0.051
△	Tunnel C	1440	0.089
—	Refs. 12 to 14	730	0.051
- - -	Refs. 12 to 14	1400	0.091

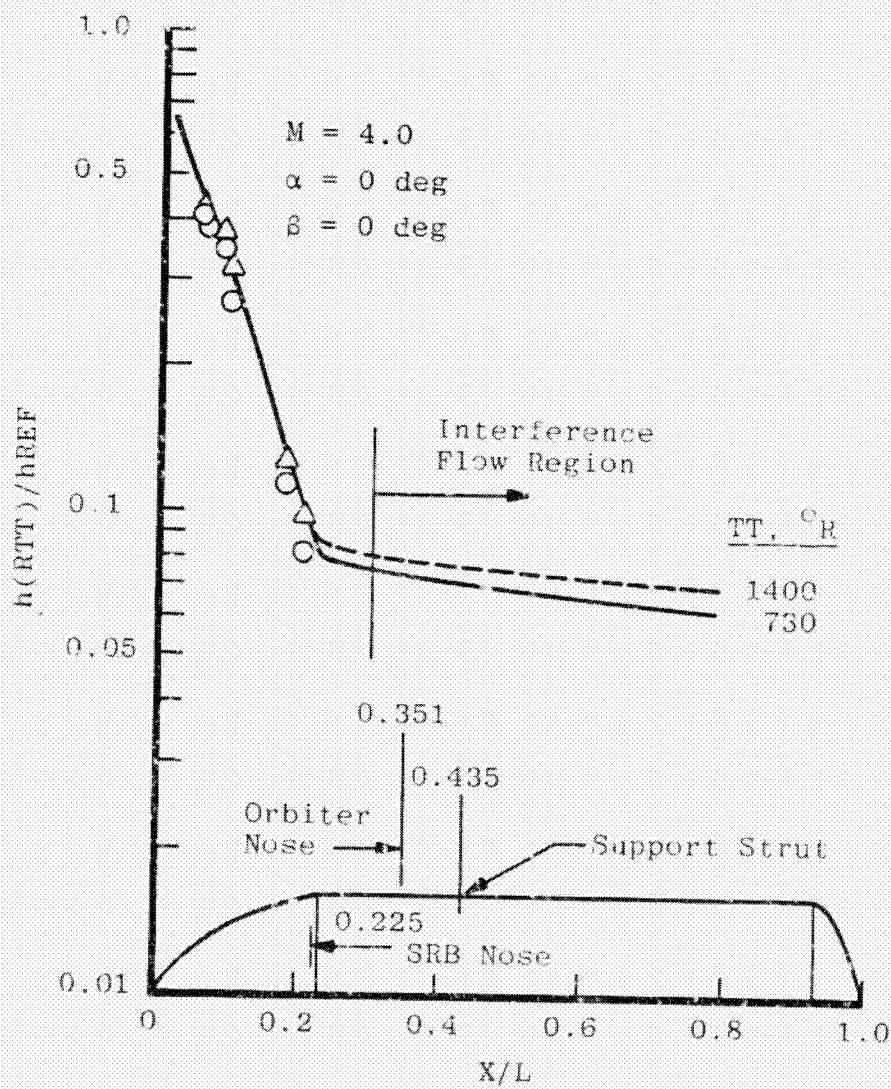
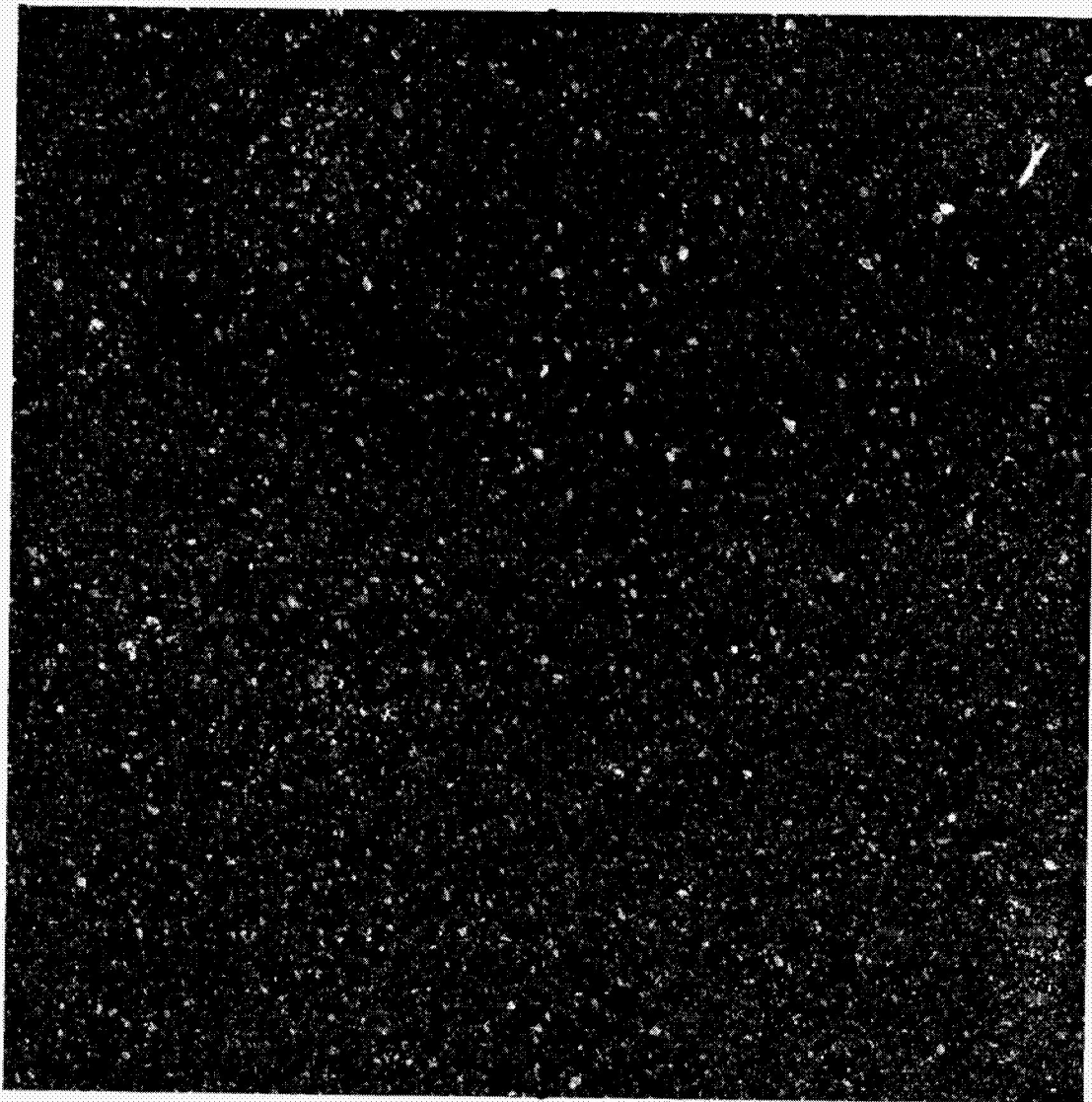


Figure 12. Data comparison with analytical turbulent heat-transfer-rate distributions on the external tank alone.

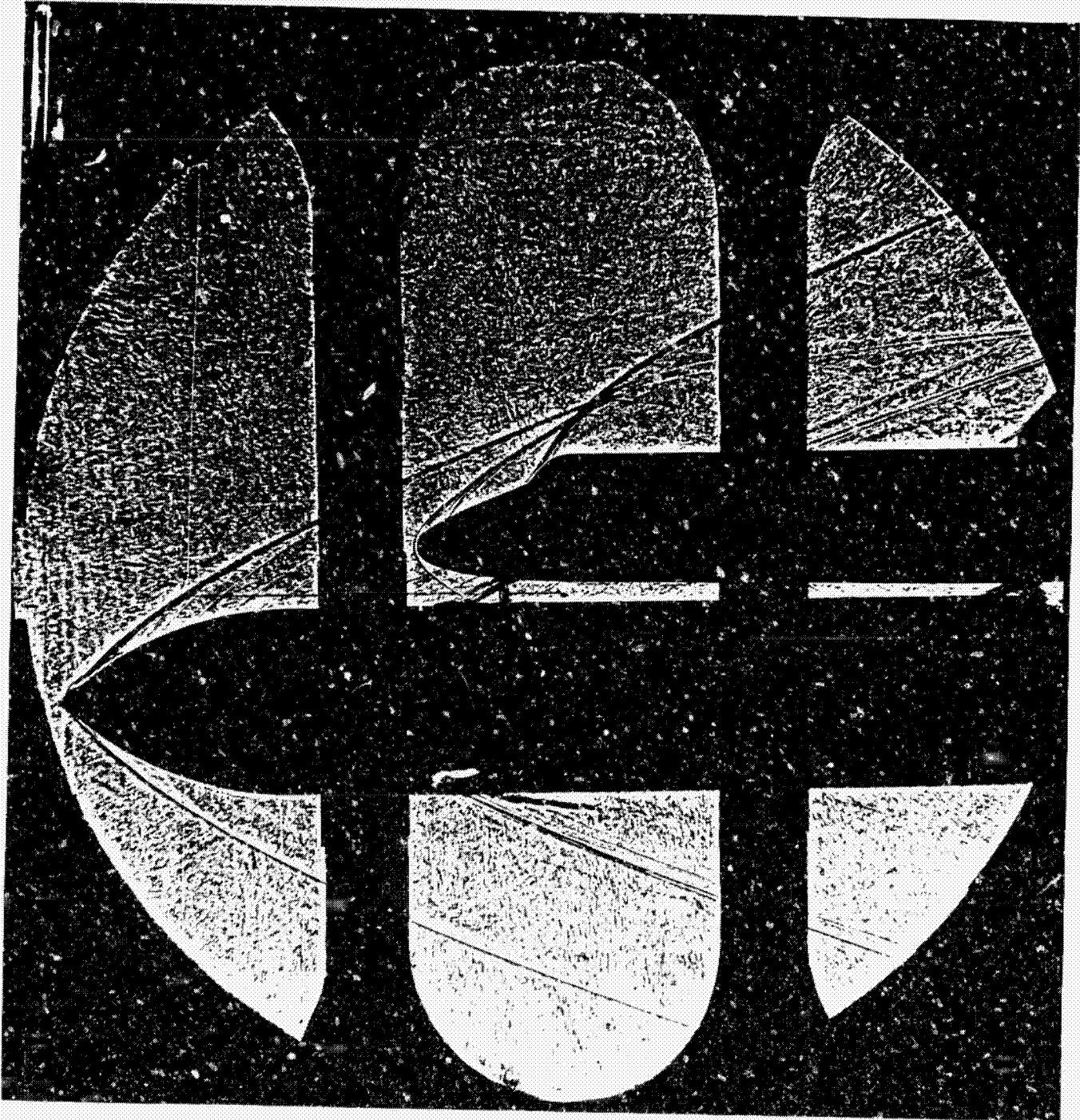
ORIGINAL FILED IN
OF POOR QUALITY



a. Tunnel A ($IT = 740^\circ R$)

Figure 13. Model shadowgraph photographs for $\alpha = 0$, $\beta = 0$.

SHOCK WAVES
OF POOR QUALITY

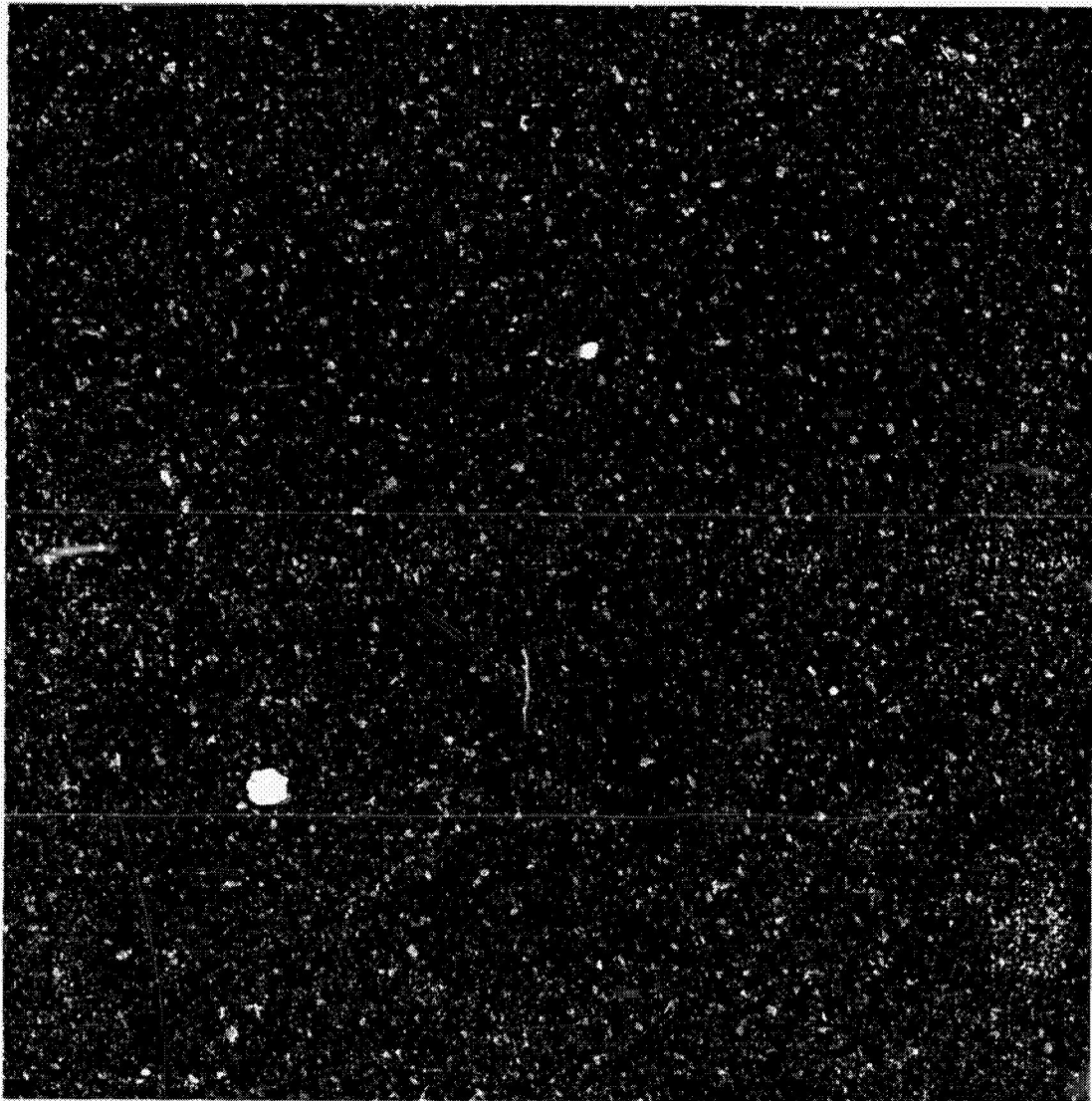


a. Tunnel A ($TT = 740^{\circ}R$)
Figure 13. Model shadowgraph photographs
for $\alpha = 0$, $\beta = 0$.

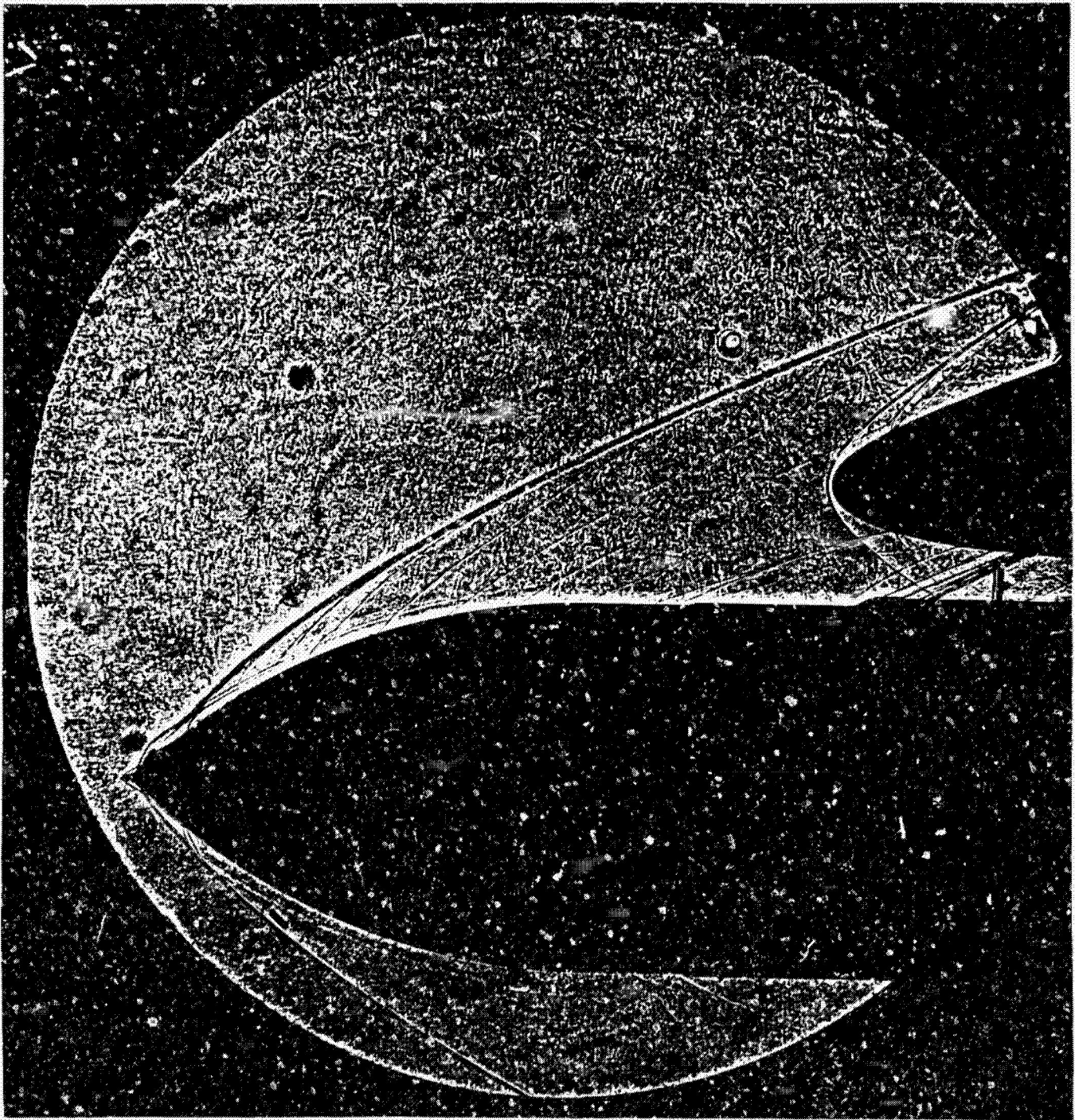
TR-84-3

983

ORBITAL REENTRY
OF RECONSTITUTED



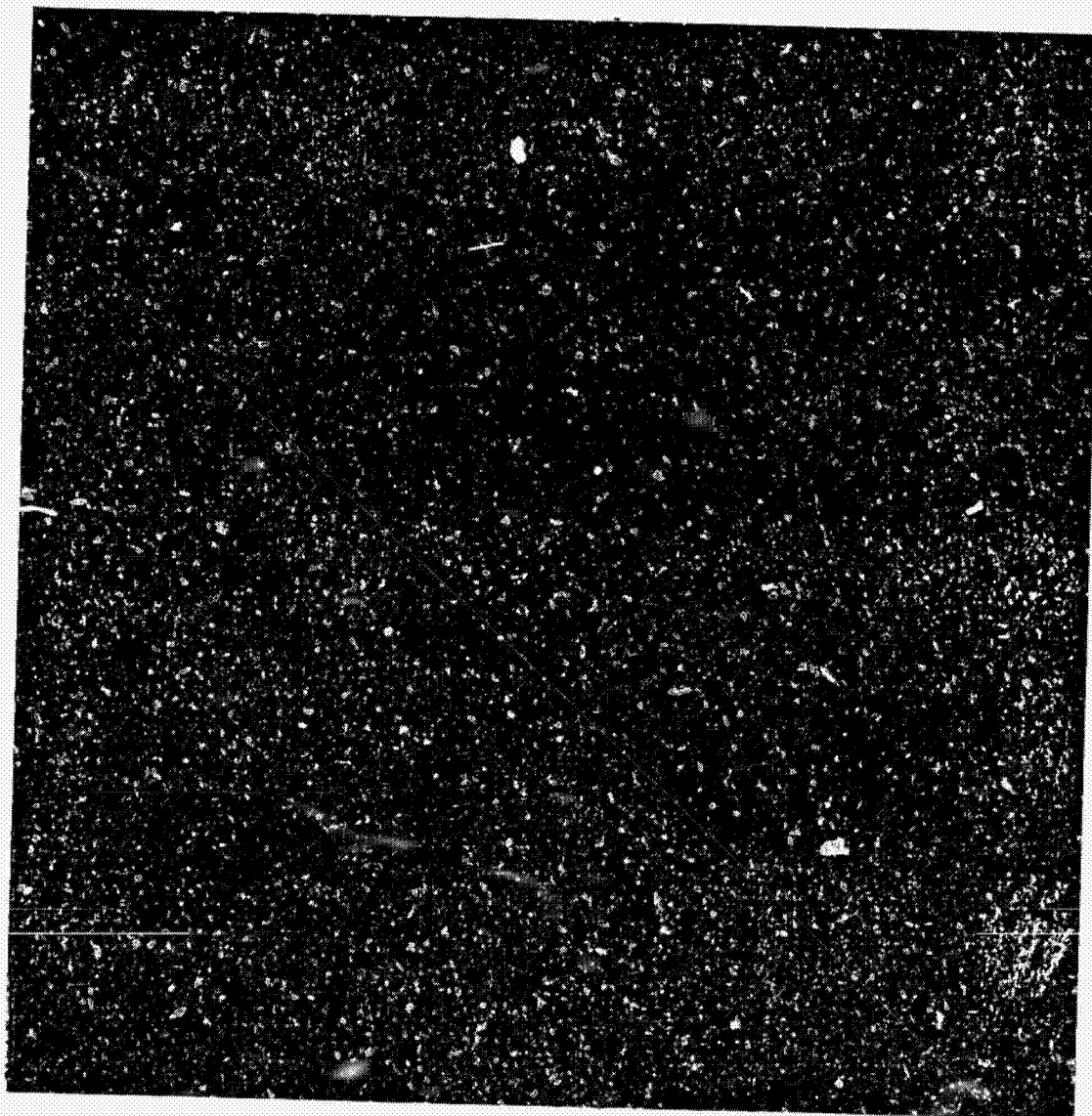
b. Model forebody, Tunnel C (TT = 1440°R)
Figure 13. Continued.



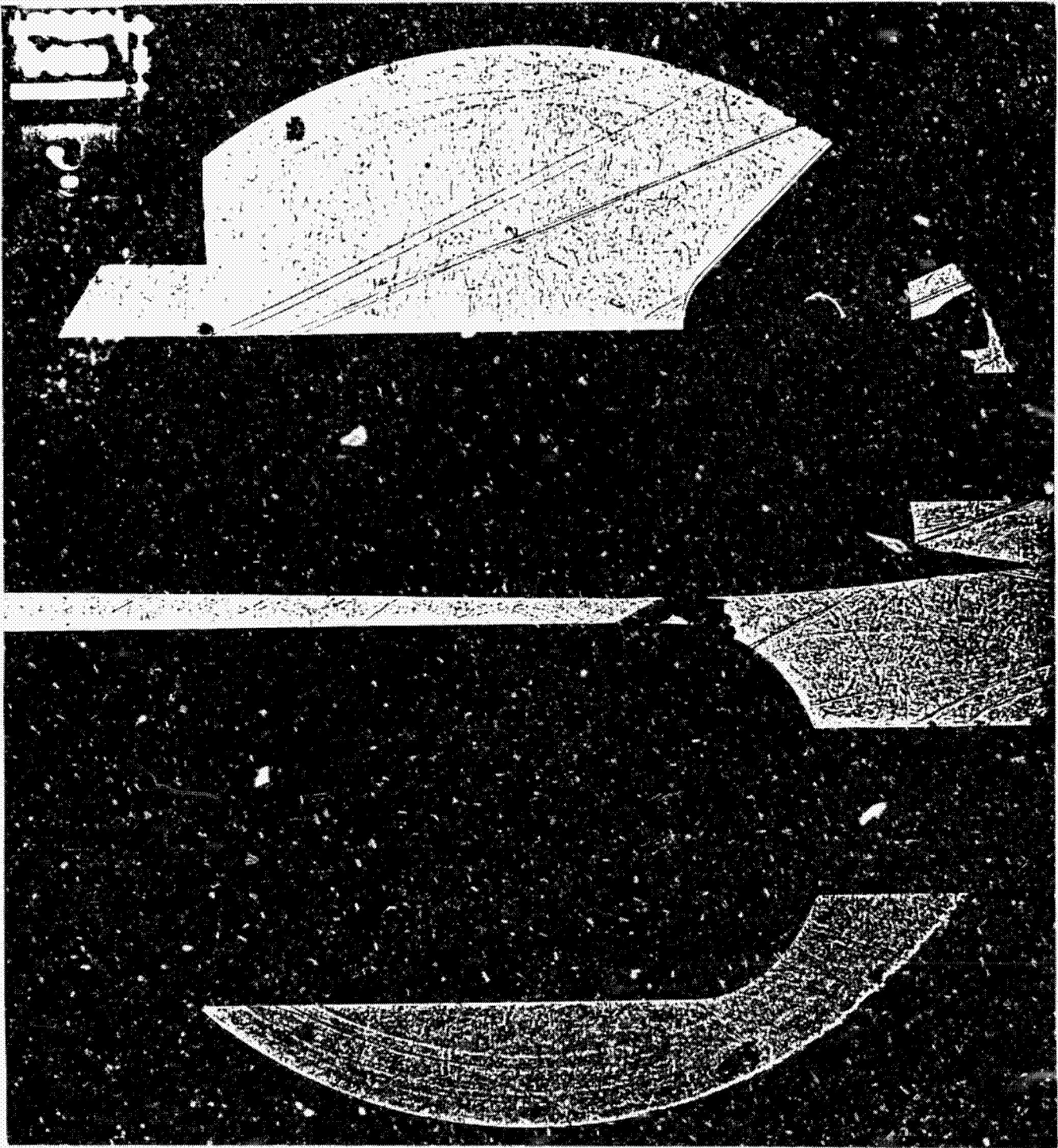
b. Tunnel C (TT = 1440⁰R)
Figure 13. Continued.
TR-84-3

42/10

PHOTO QUALITY

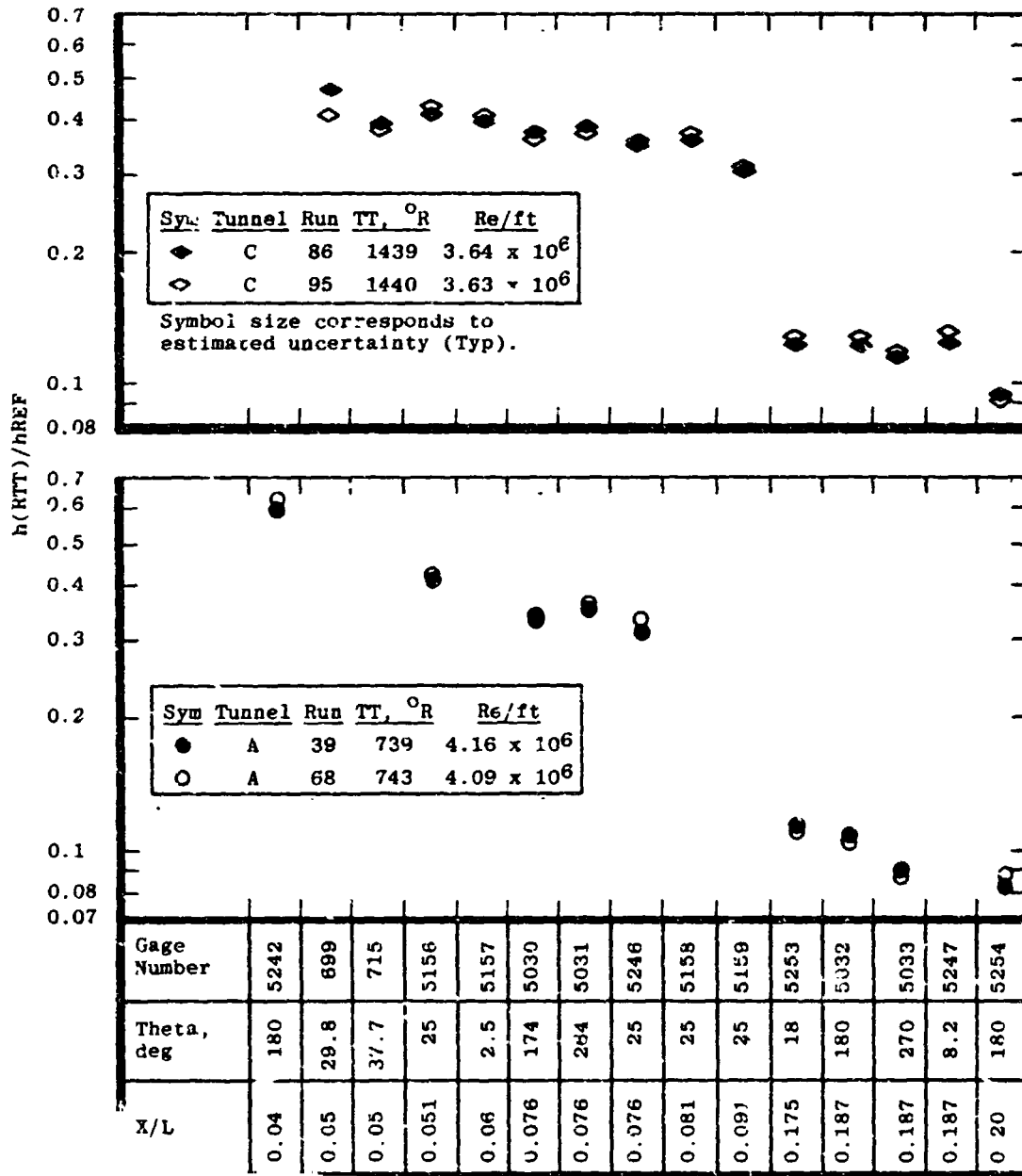


c. Model aft-body, Tunnel C (TT = 1440°R)
Figure 13. Concluded.

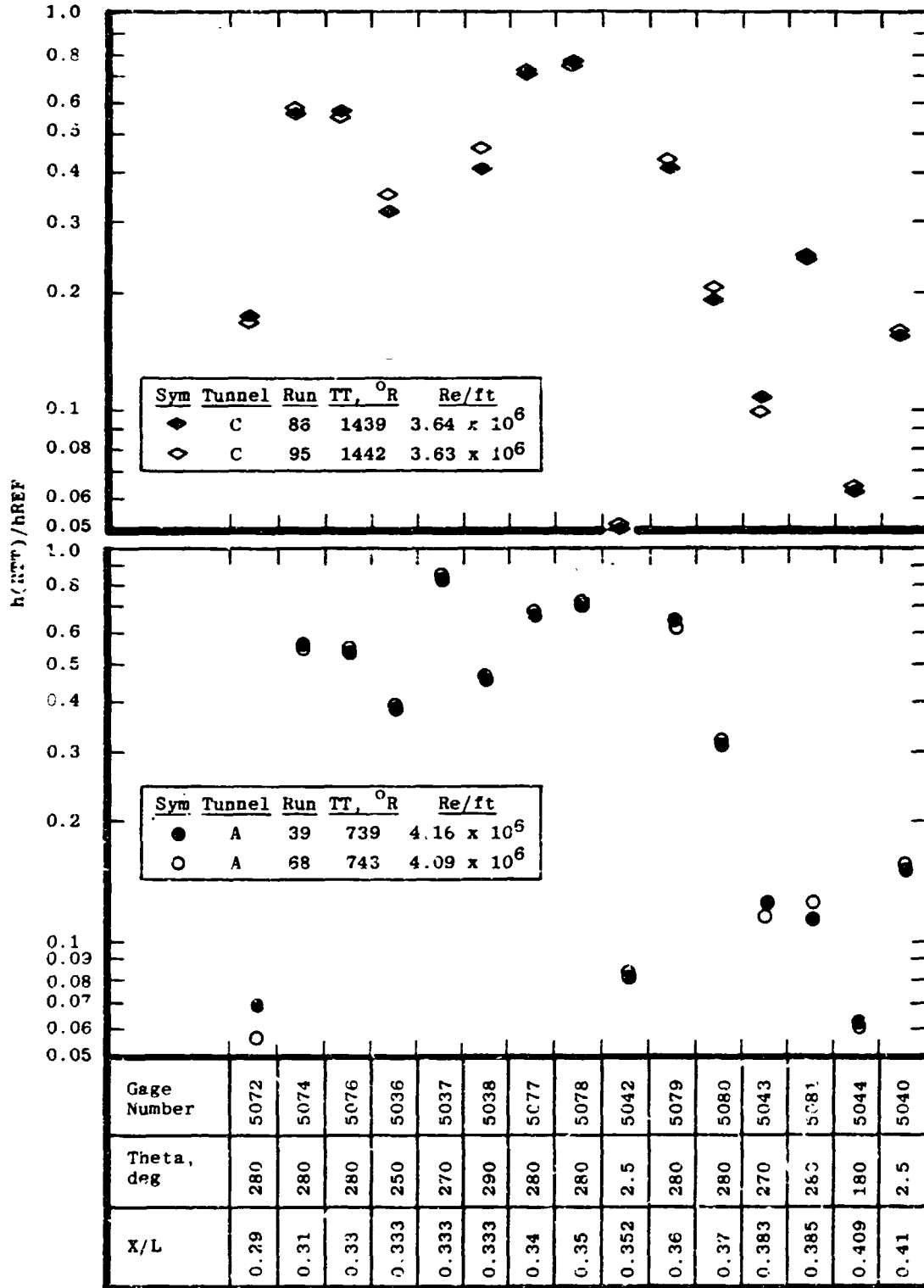


c. Tunnel C (TT = 1440°R)
Figure 13. Concluded.
TR-84-3

8.2.11

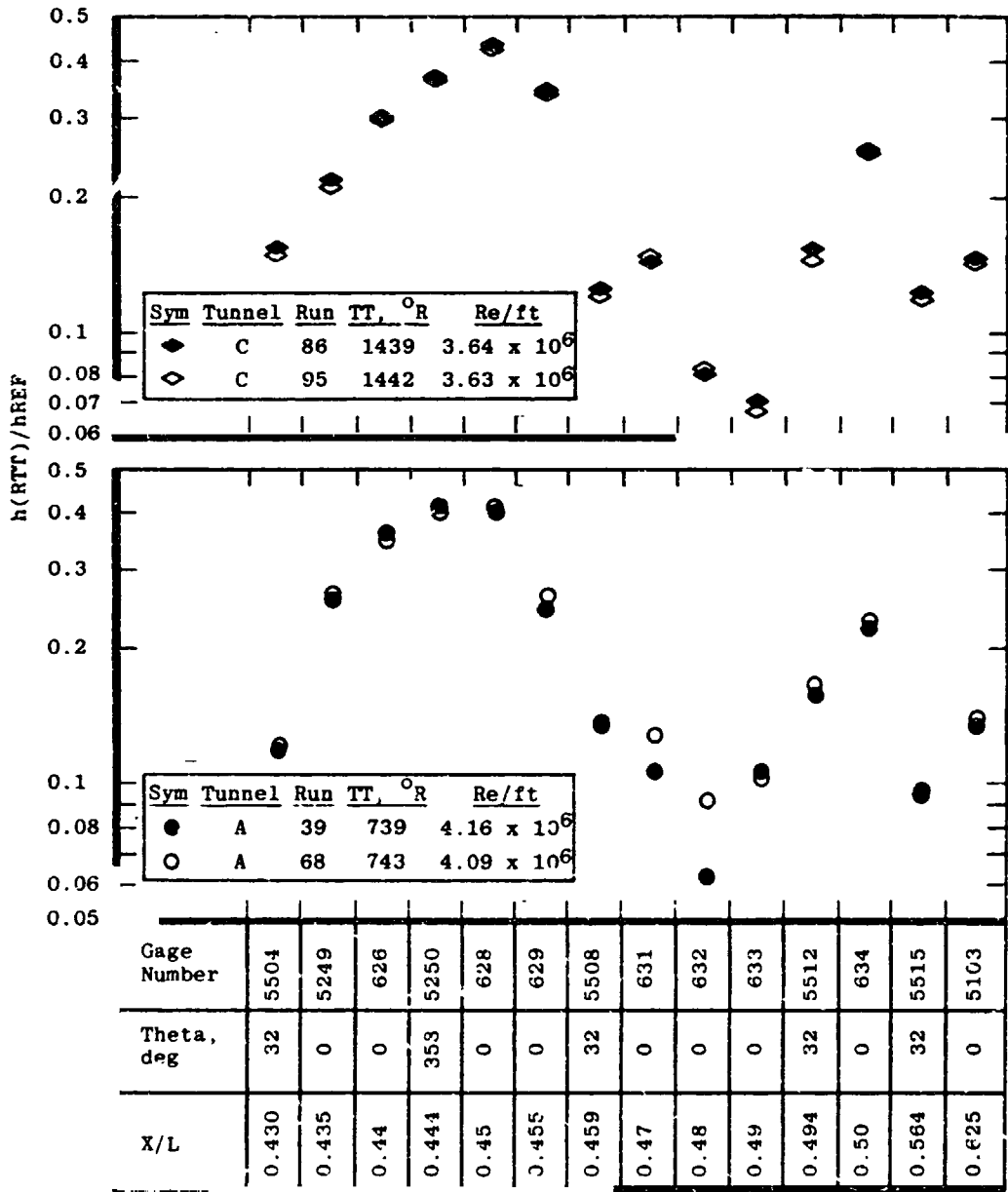


a. $0 < X/L \leq 0.25$
 Figure 14. Data repeatability.

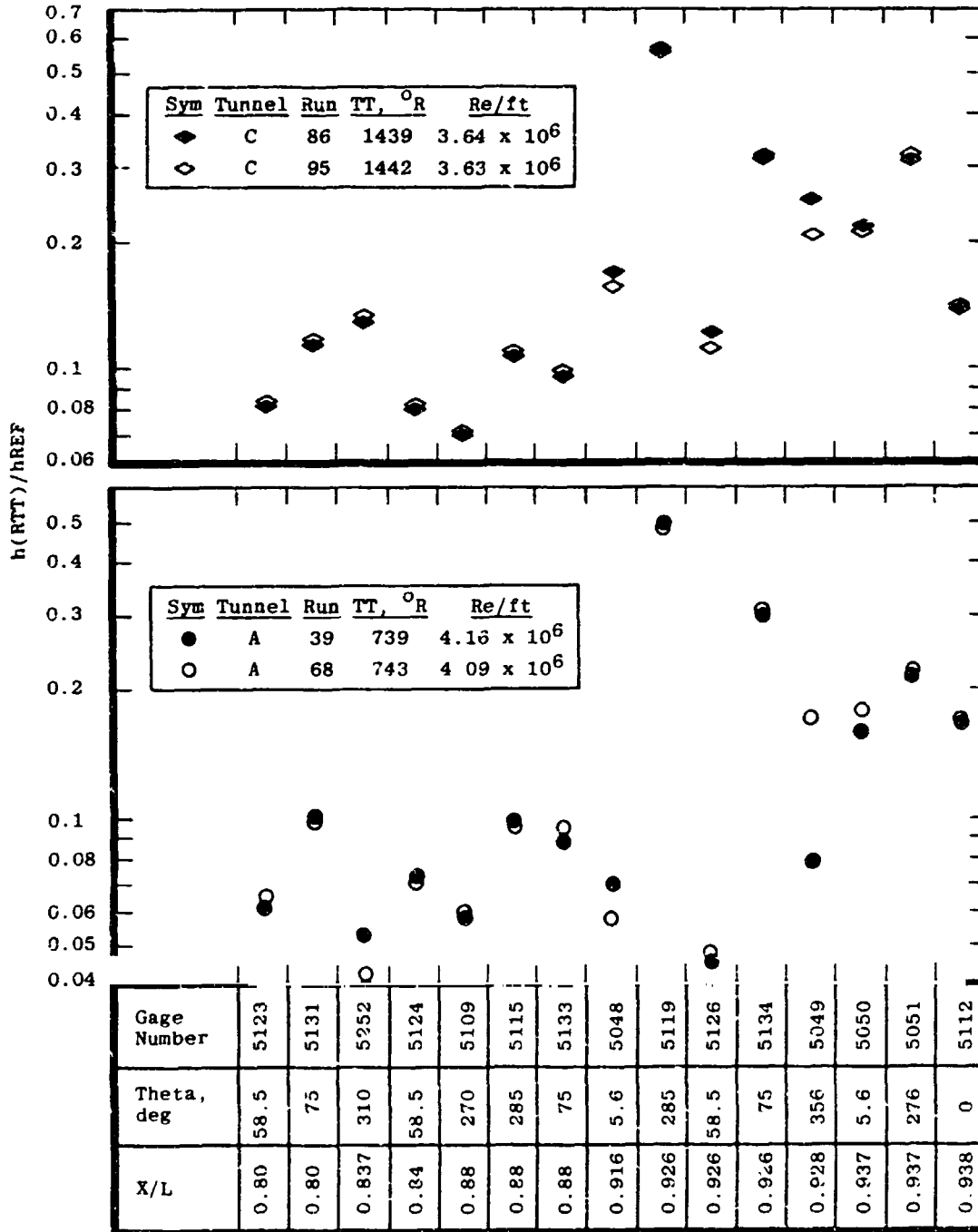


b. $0.25 < X/L \leq 0.43$

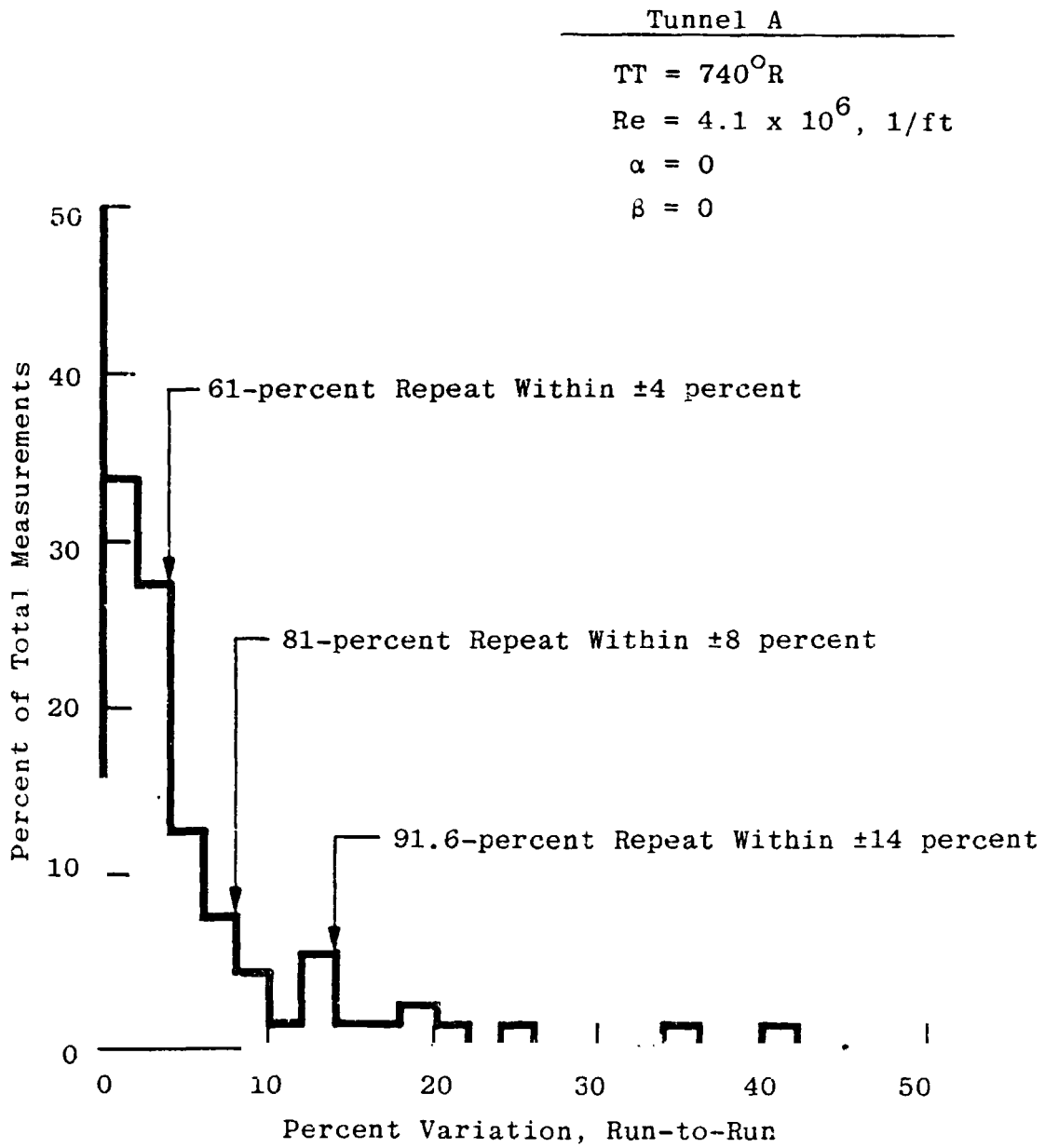
Figure 14. Continued.



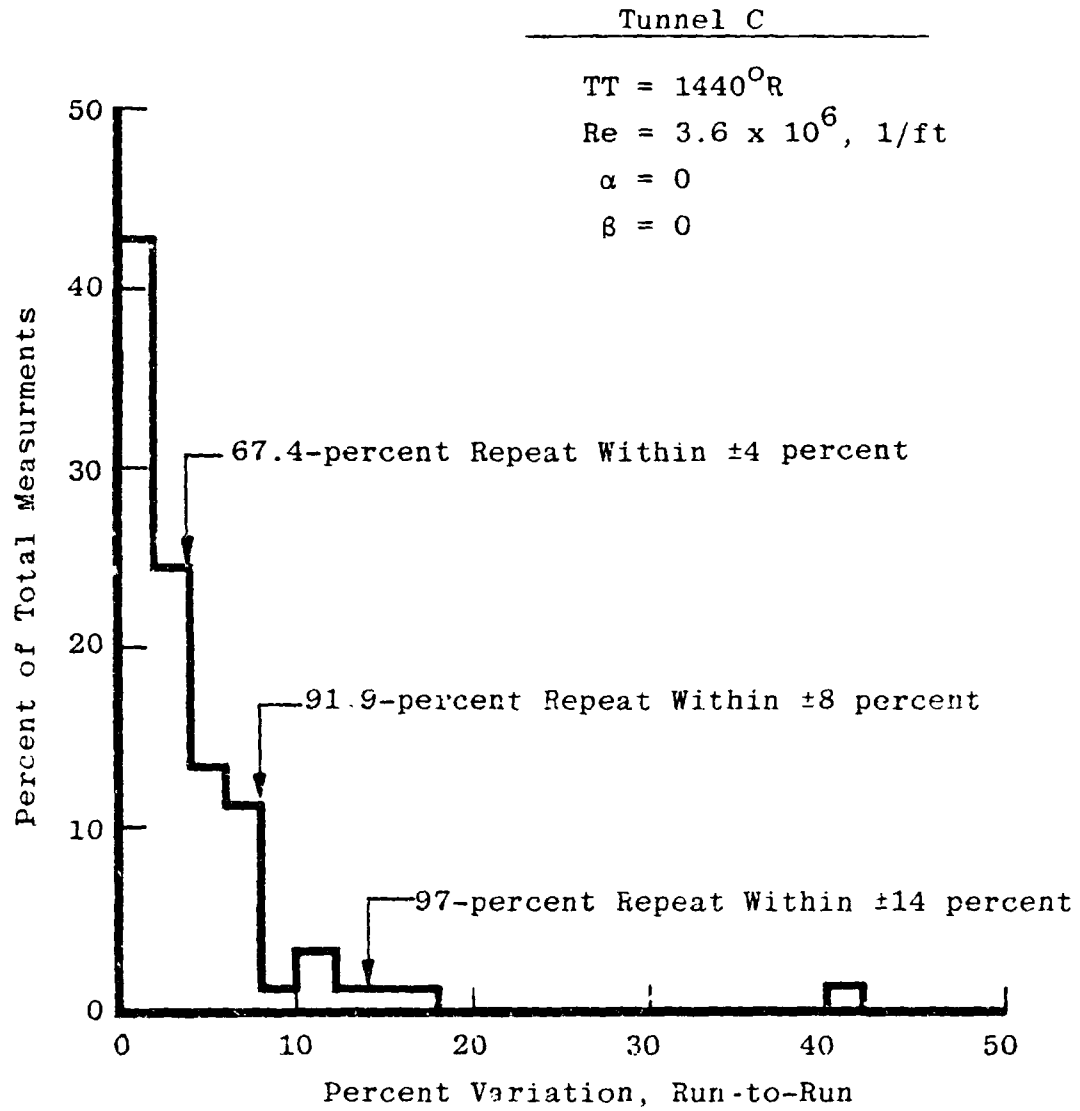
c. $0.43 < X/L \leq 0.725$
 Figure 14. Continued.



d. $0.725 < X/L \leq 1.0$
 Figure 14. Concluded.



a. Tunnel A
Figure 15. Distribution of measurement repeatability.



b. Tunnel C
Figure 15. Concluded.

$$\text{Percent Variation} = \left| \frac{\left(\frac{h(RTT)}{hREF}\right)_{\text{Tunnel A}} - \left(\frac{h(RTT)}{hREF}\right)_{\text{Tunnel C}(1440^{\circ}\text{R})}}{\left(\frac{h(RTT)}{hREF}\right)_{\text{Tunnel C}(1440^{\circ}\text{R})}} \right|$$

$\alpha = 0$

$\beta = 0$

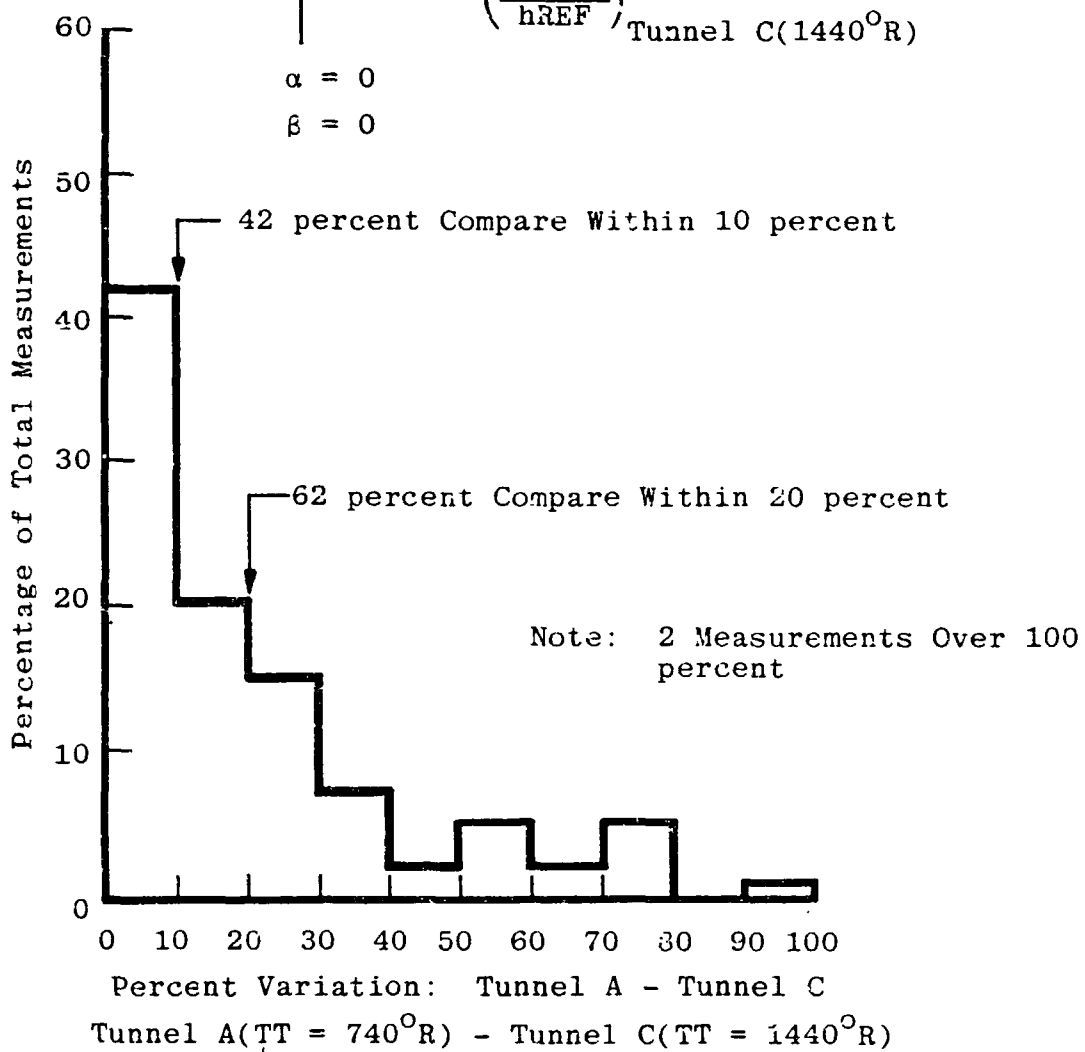


Figure 16. Comparability of Tunnel A to Tunnel C measurements.

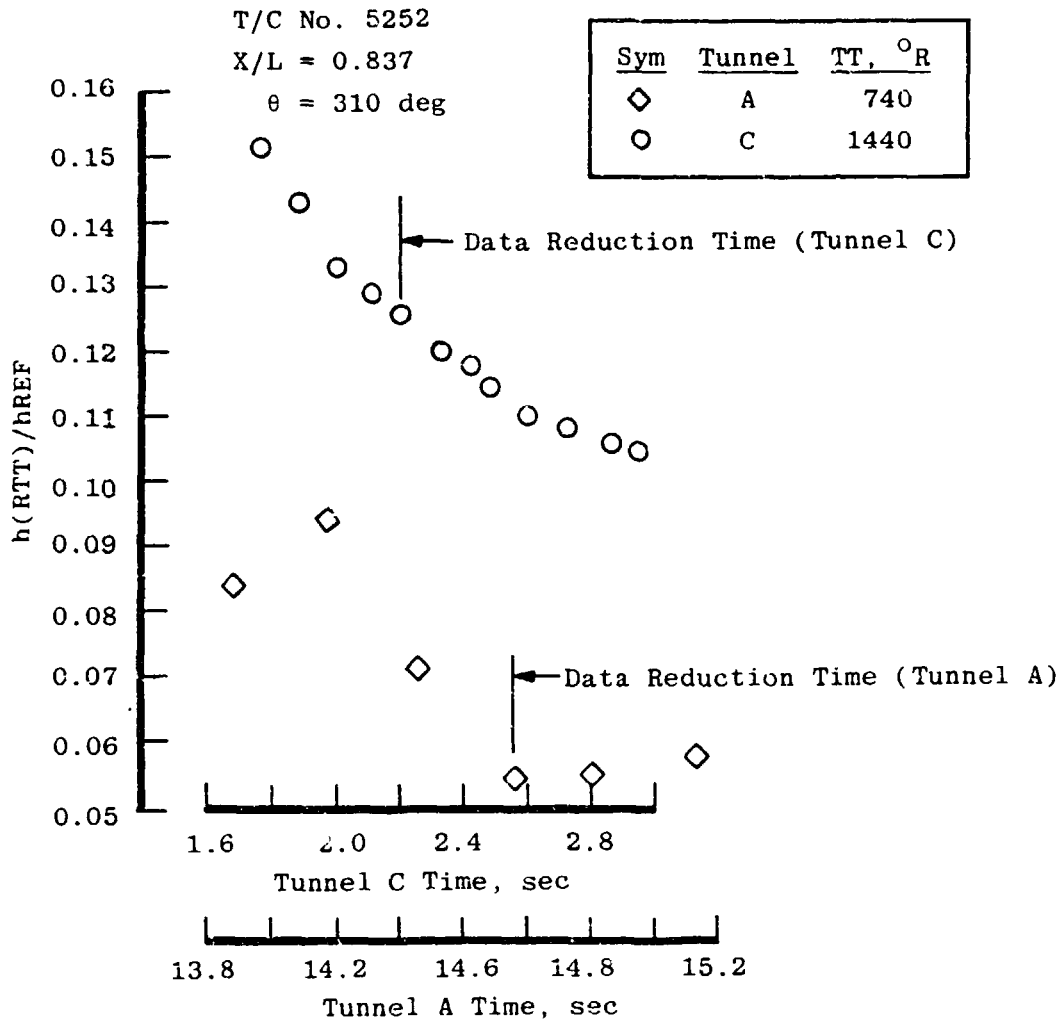


Figure 17. Gage measurement influenced by thermal conduction.

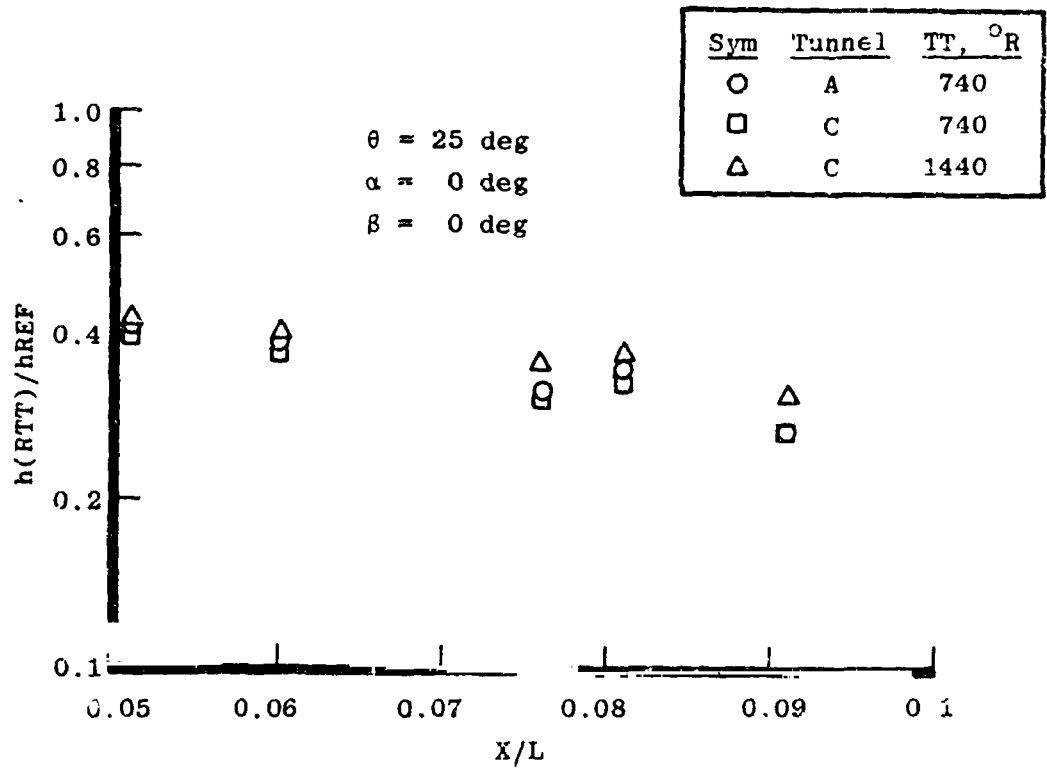
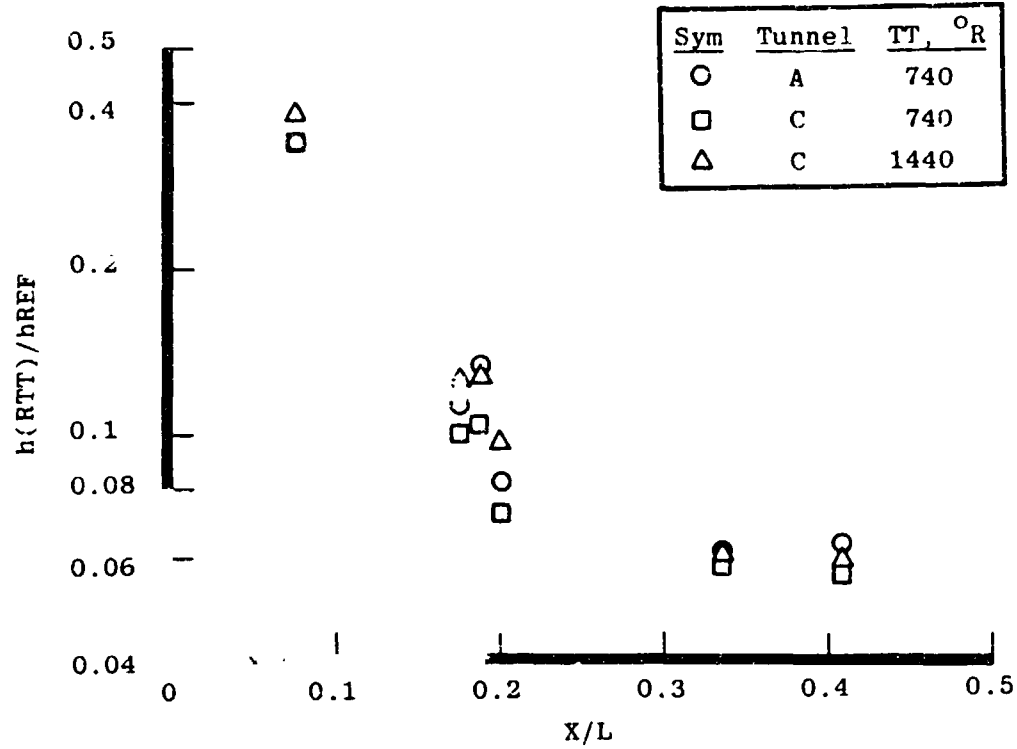
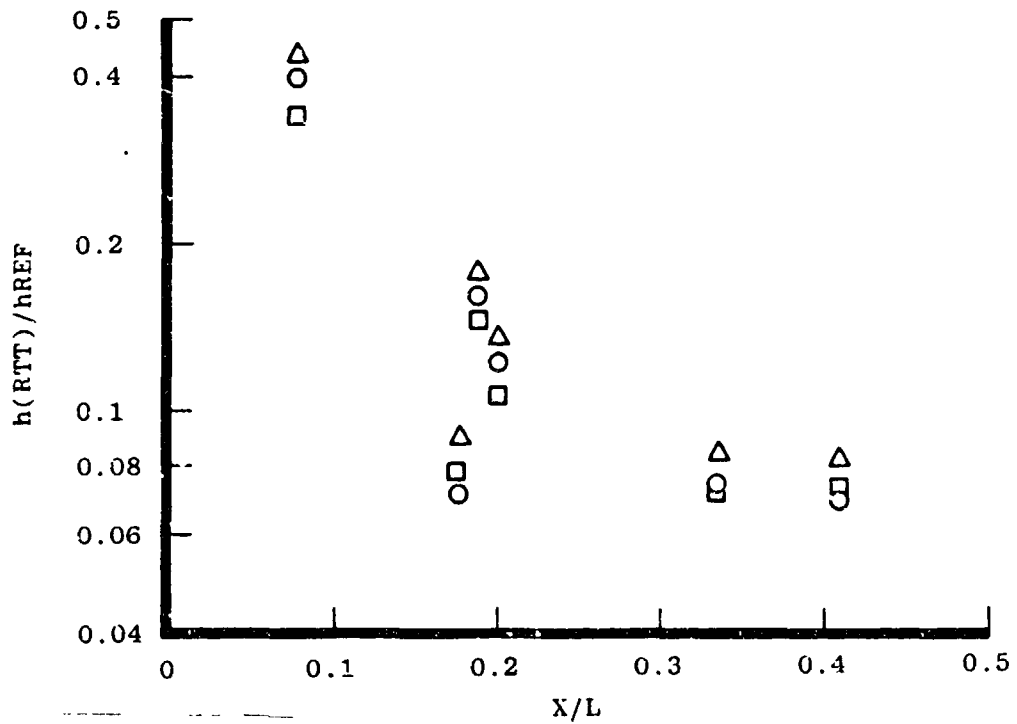


Figure 18. Heating distribution on nose section (theta = 25 deg).

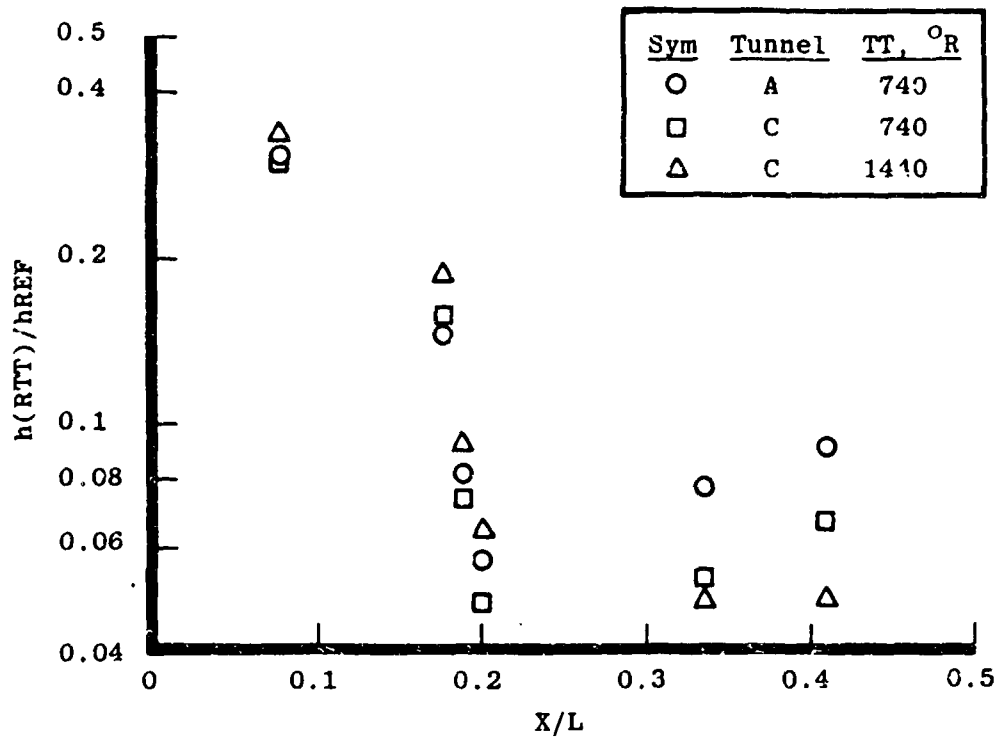


a. Alpha = 0 deg

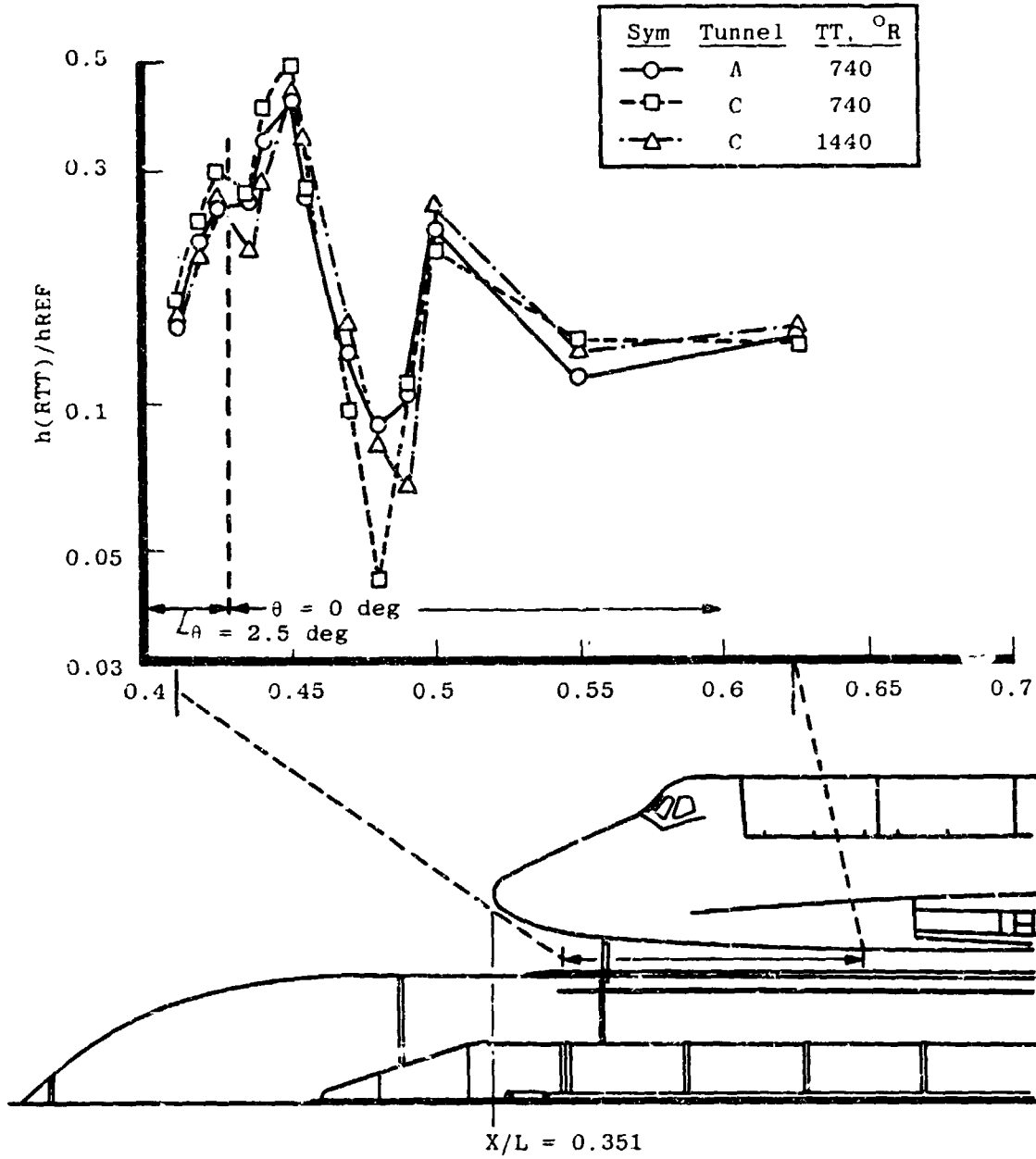


b. Alpha = 5 deg

Figure 19. Heating distribution on bottom centerline (theta = 180 deg).

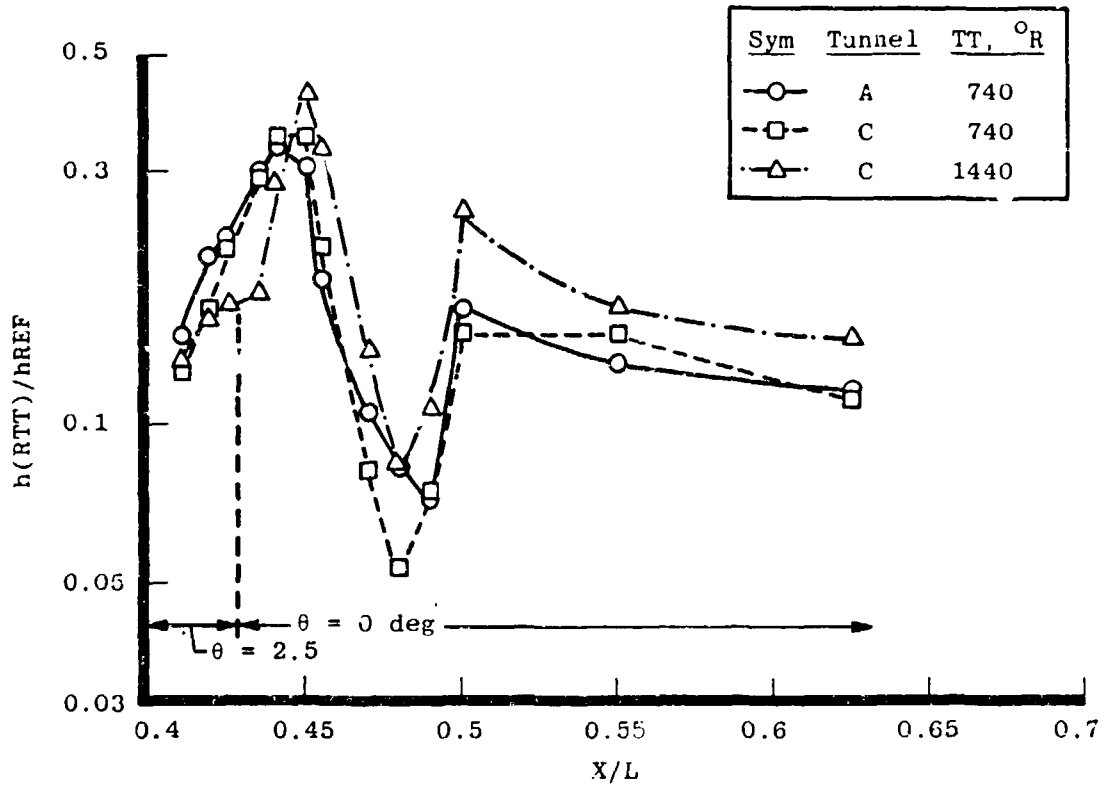


c. Alpha = --5 deg
 Figure 19. Concluded.

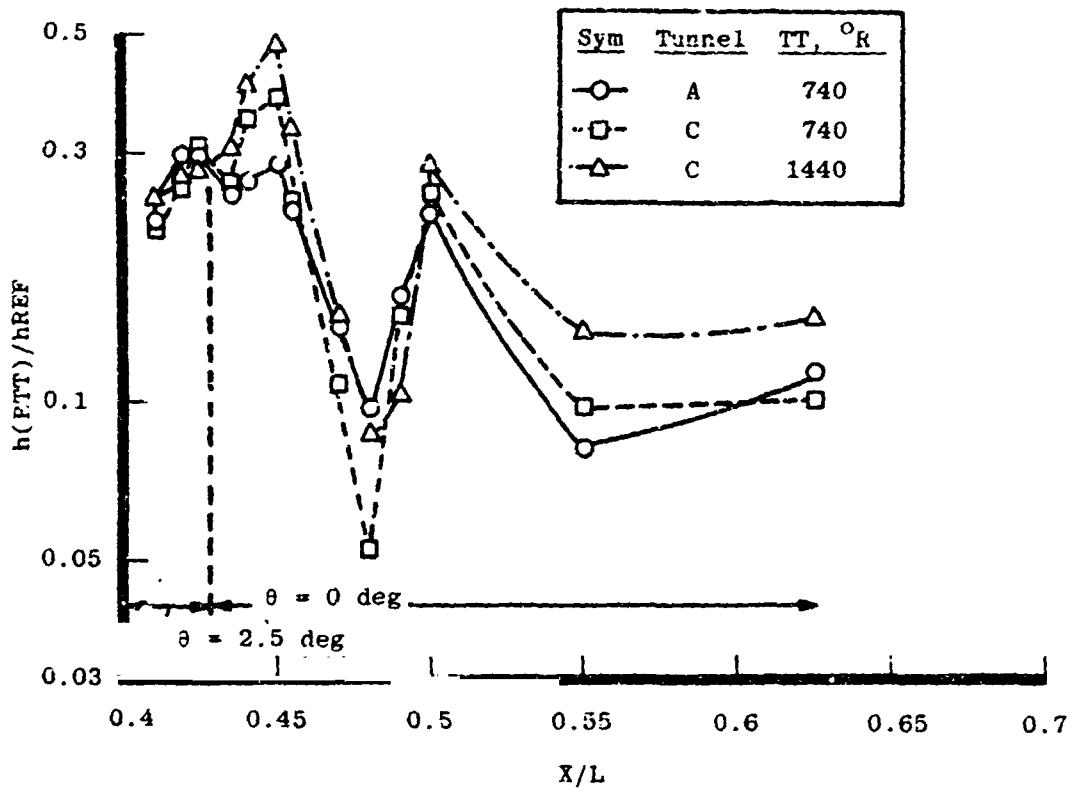


a. Alpha = 0 deg

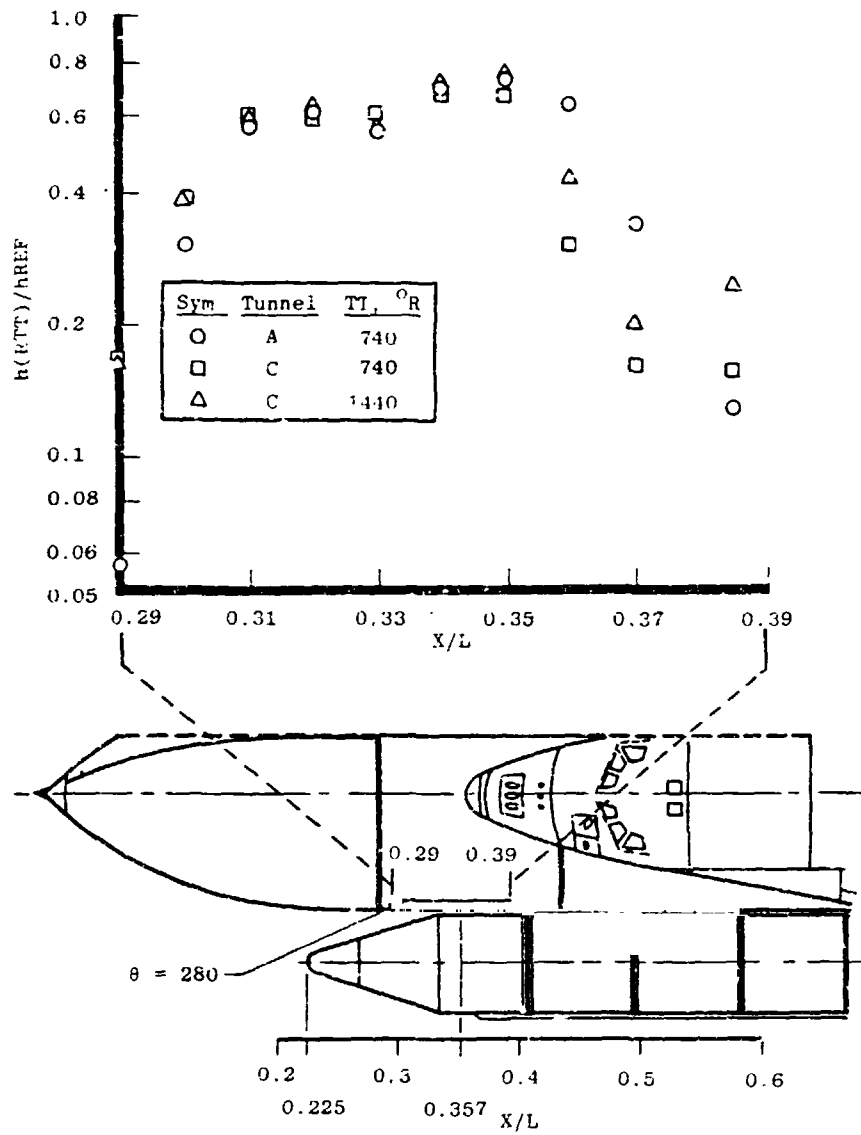
Figure 20. Heating distribution on top centerline of external tank in region of orbiter bow-shock impingement.



b. Alpha = 5 deg
 Figure 20. Continued.

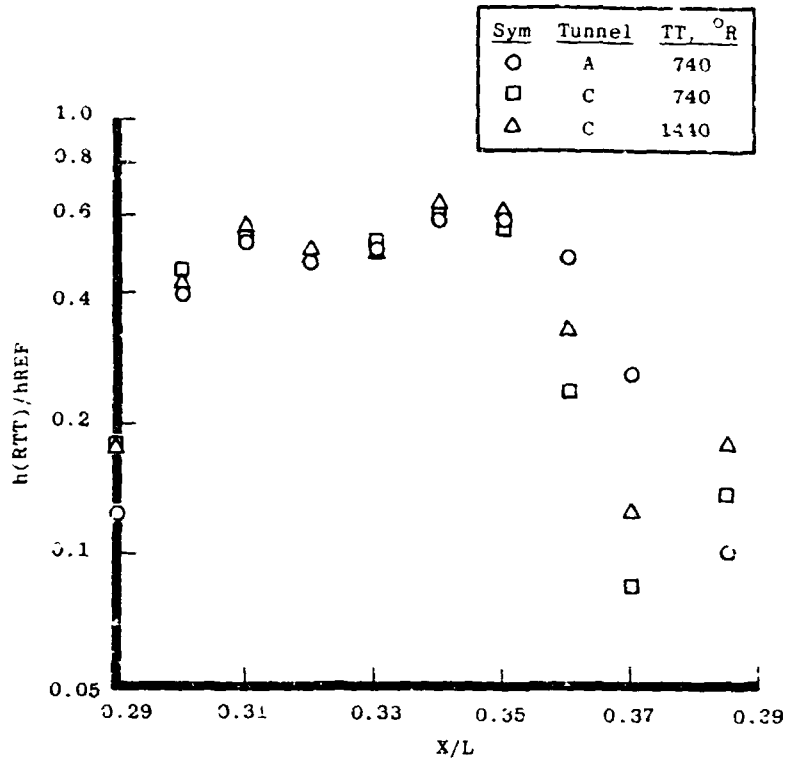


c. Alpha = -5 deg
 Figure 20. Concluded.

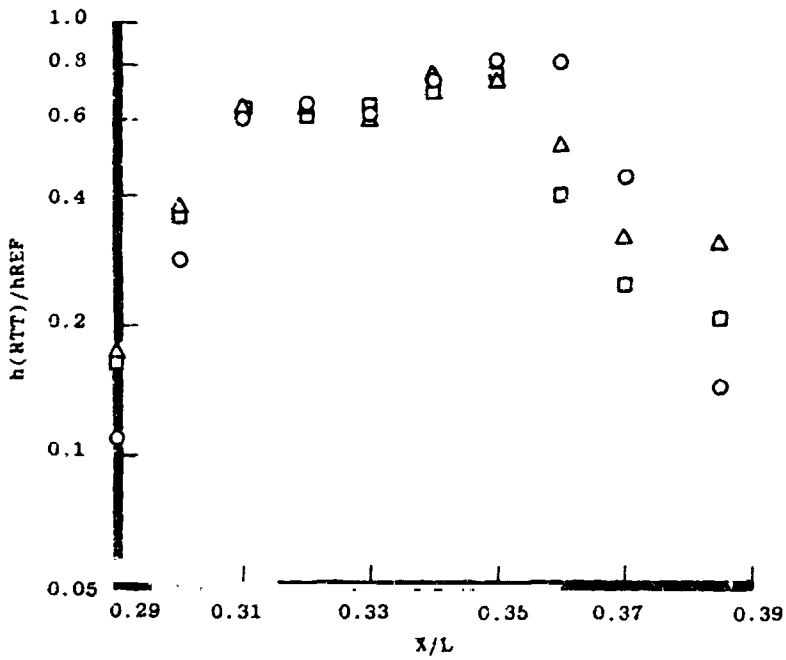


a. Alpha = 0 deg, beta = 0 deg

Figure 21. Heating distribution in the region of forward SRB attach strut (theta = 280 deg).

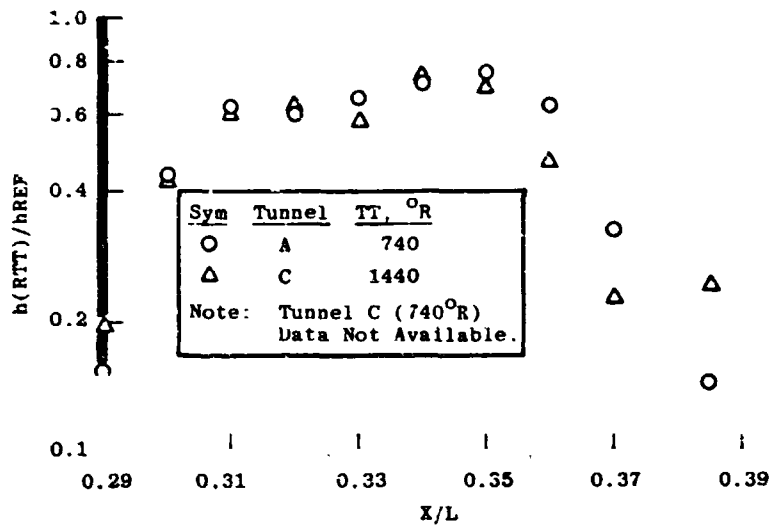


b. Alpha = 5 deg, beta = 0 deg

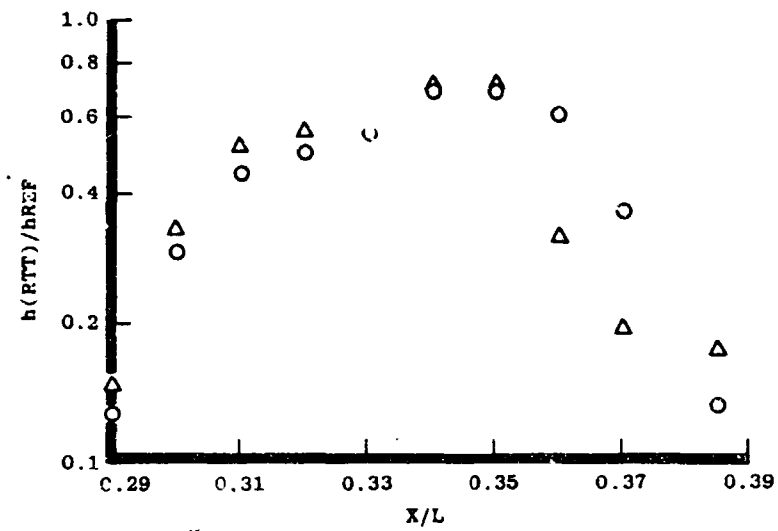


c. Alpha = -5 deg, beta = 0 deg

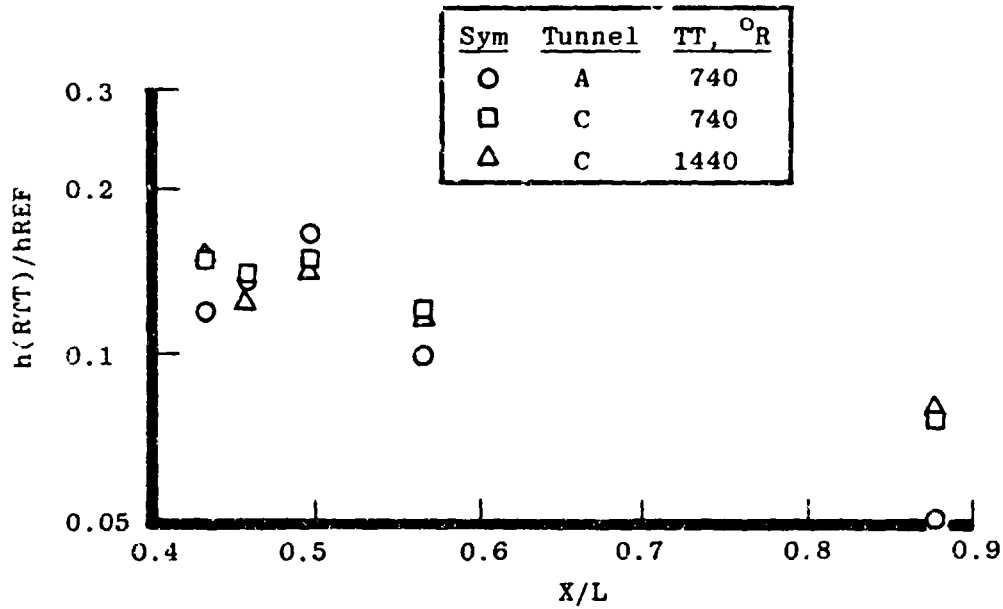
Figure 21. Continued.



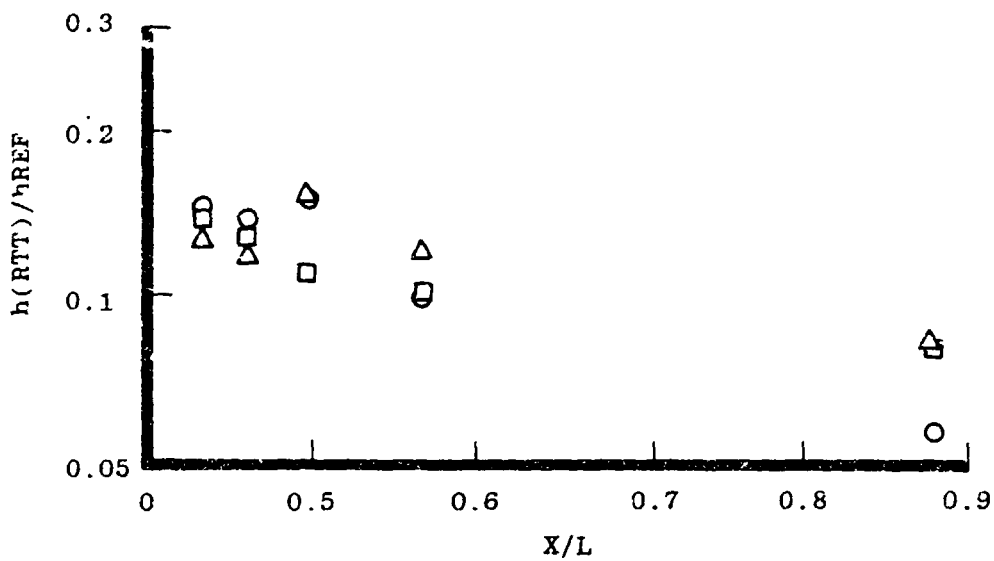
d. Alpha = 0 deg, beta = -3 deg



e. Alpha = 0 deg, beta = 3 deg
Figure 21. Concluded.

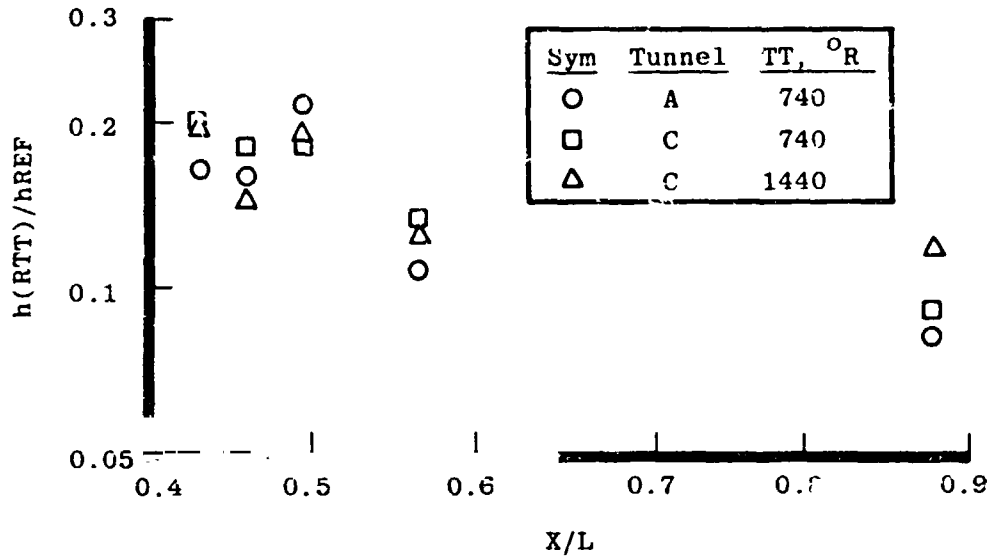


a. Alpha = 0 deg, beta = 0 deg

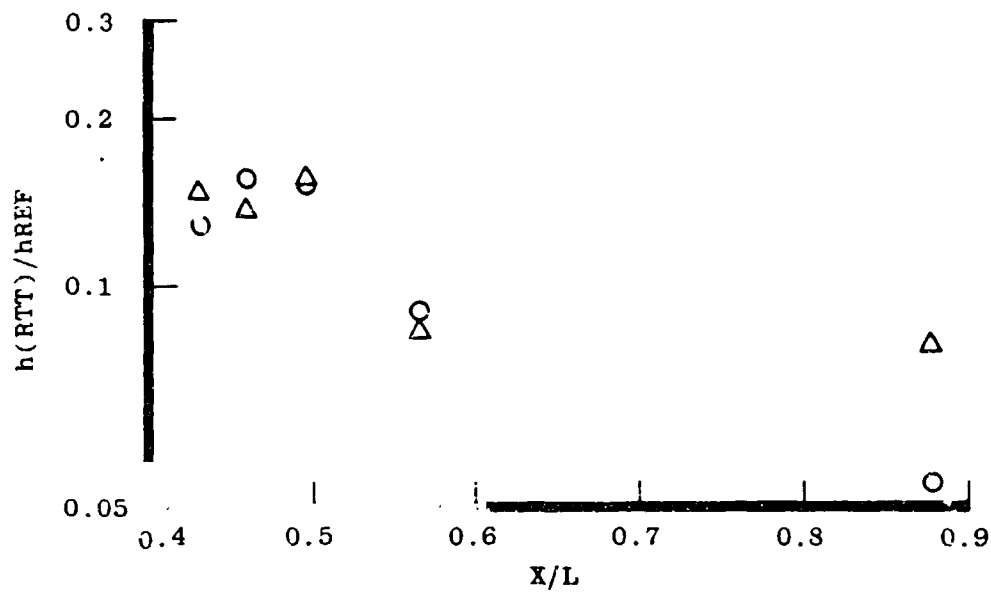


b. Alpha = 5 deg, beta = 0 deg

Figure 22. Heating distribution between LO₂ anti-geyser and LO₂ feed lines (theta = 32 deg).

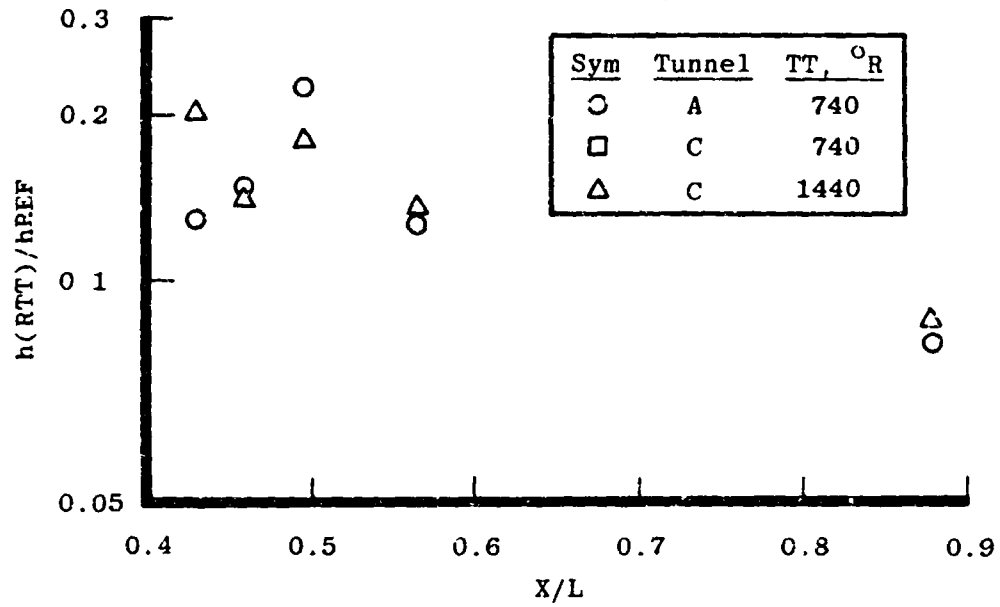


c. Alpha = -5 deg, beta = 0 deg

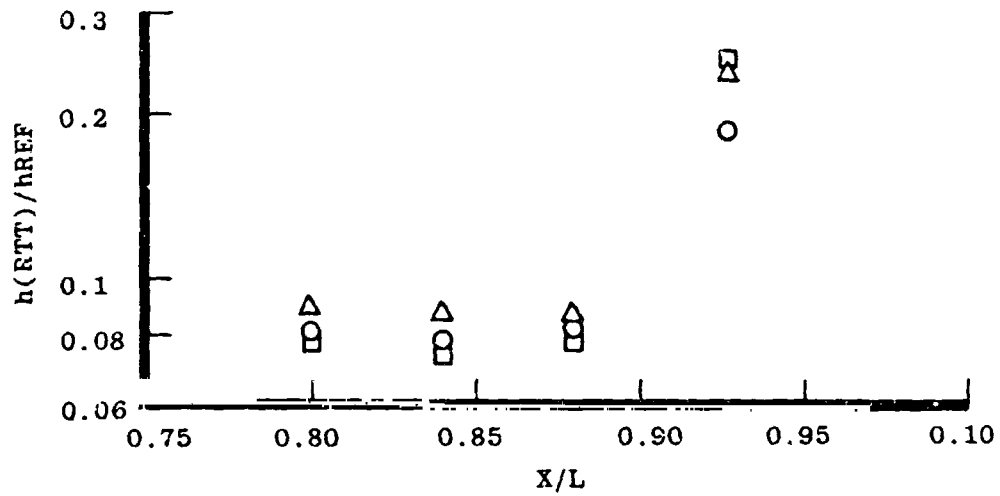


d. Alpha = 0 deg, beta = -3 deg

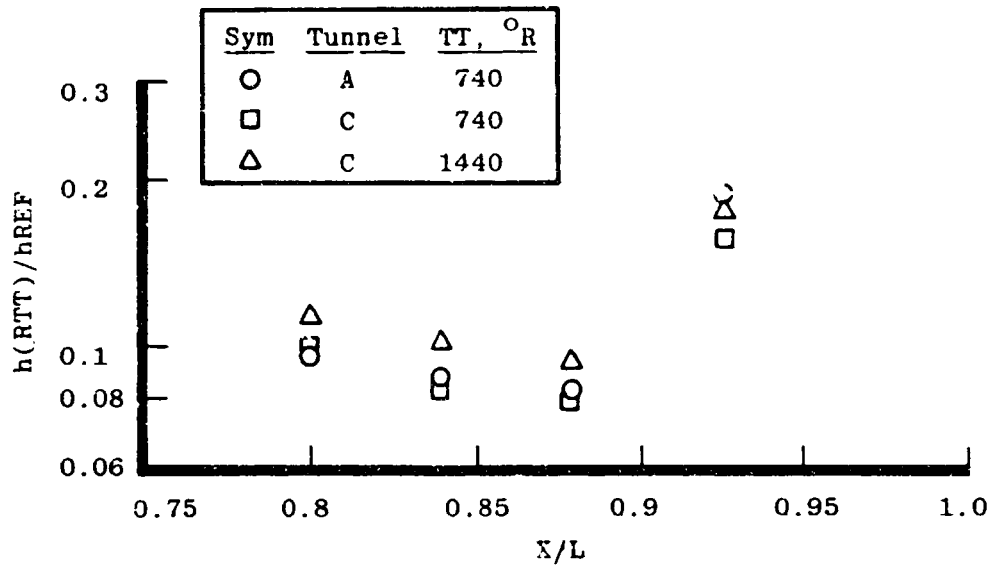
Figure 22. Continued.



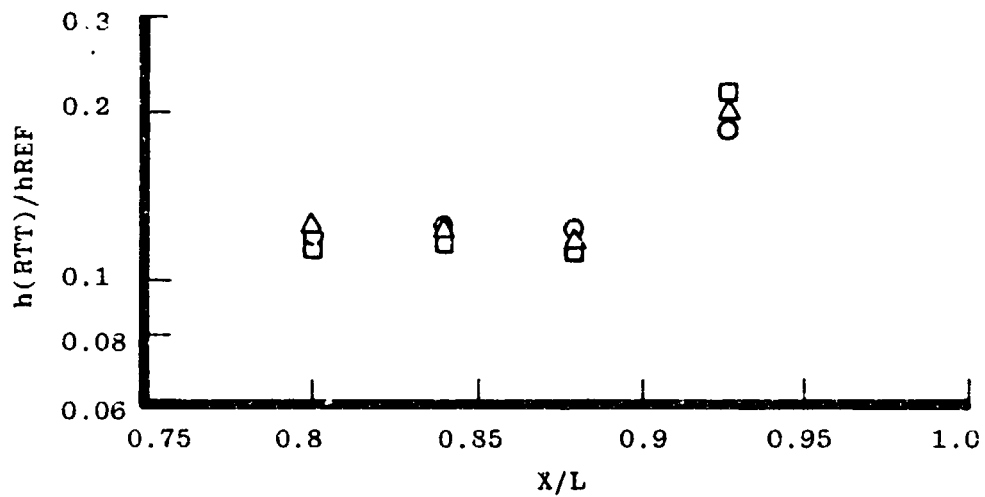
e. Alpha = 0 deg, beta = 3 deg
Figure 22. Concluded.



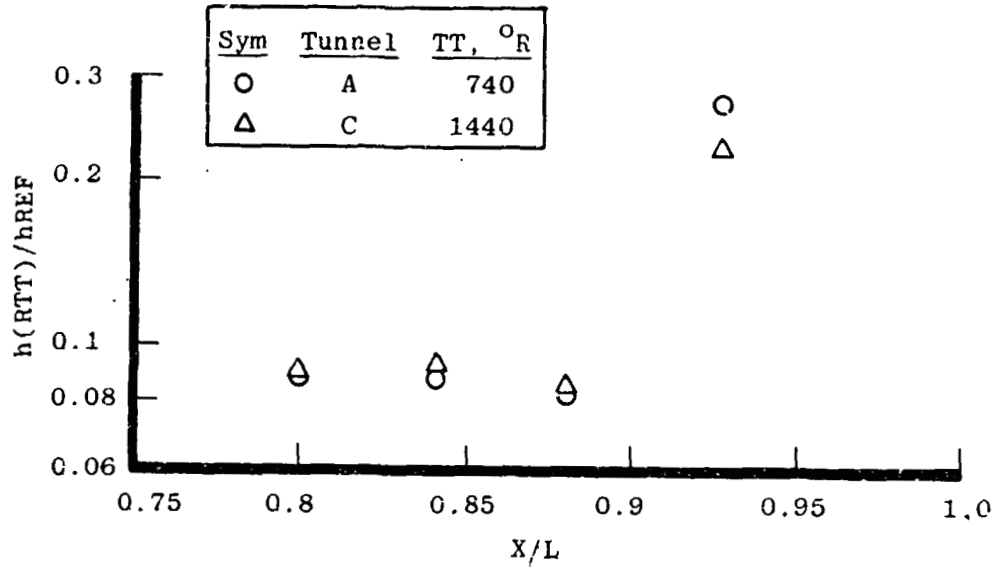
a. Alpha = 0 deg, beta = 0 deg
Figure 23. Heating distribution near the rear orbiter-to-tank attach strut
(theta = 68 deg).



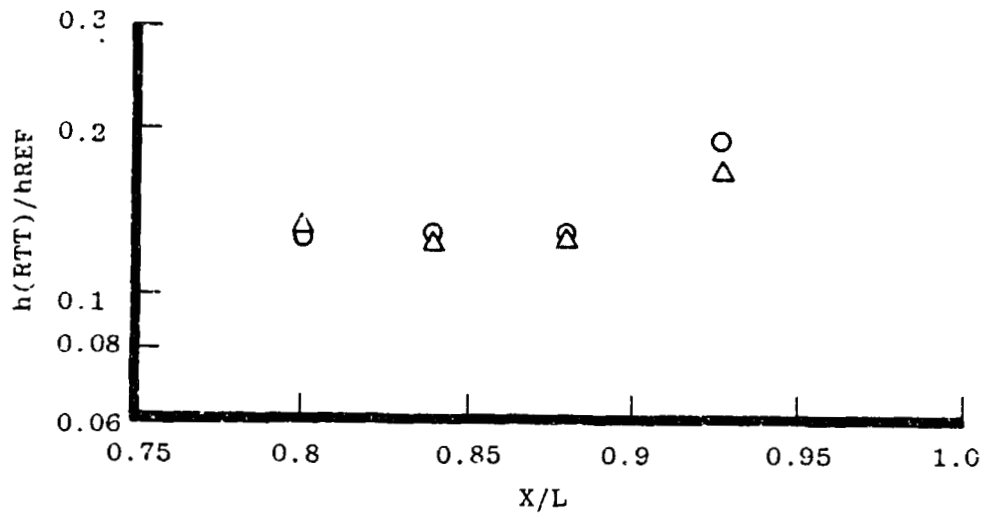
b. Alpha = 5 deg, beta = 0 deg



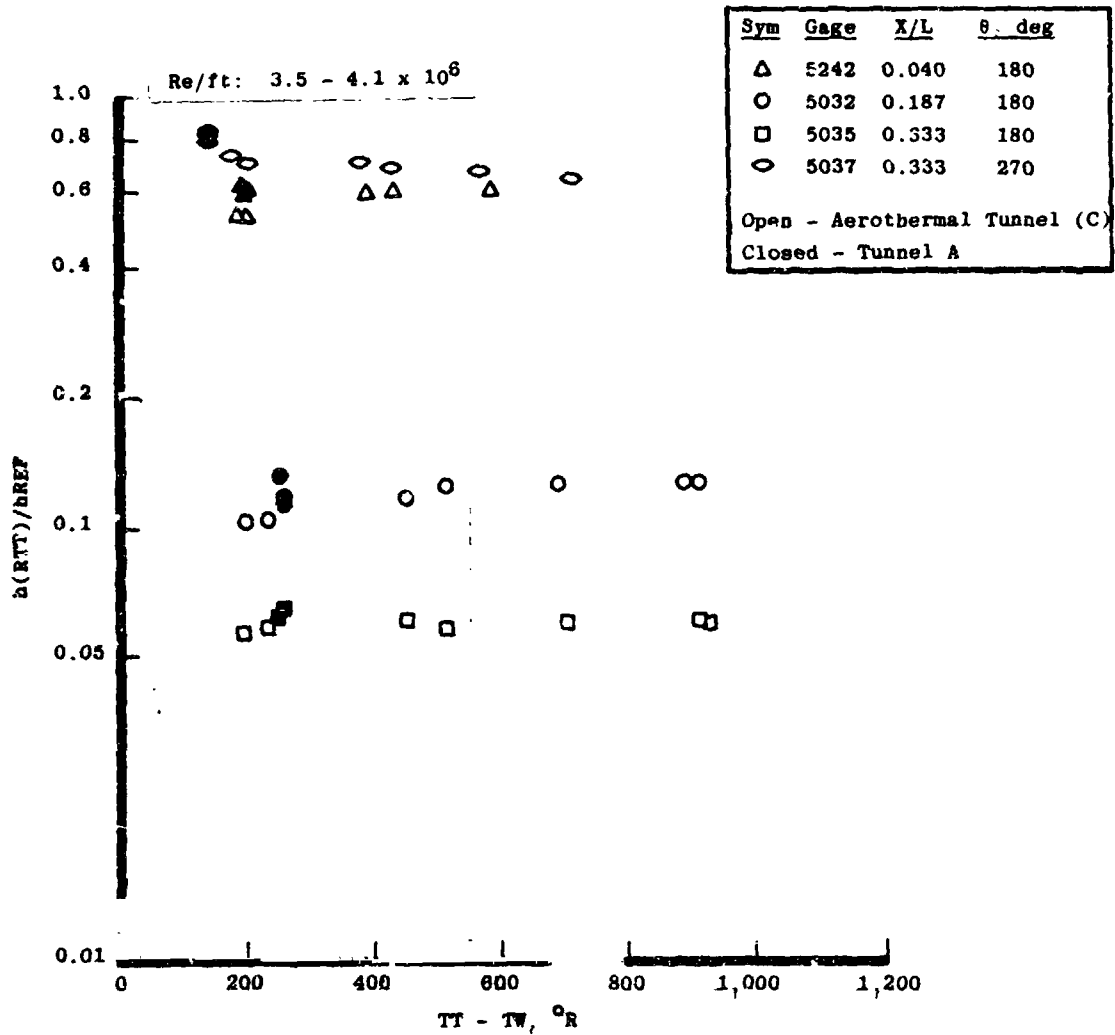
c. Alpha = -5 deg, beta = 0 deg
Figure 23. Continued.



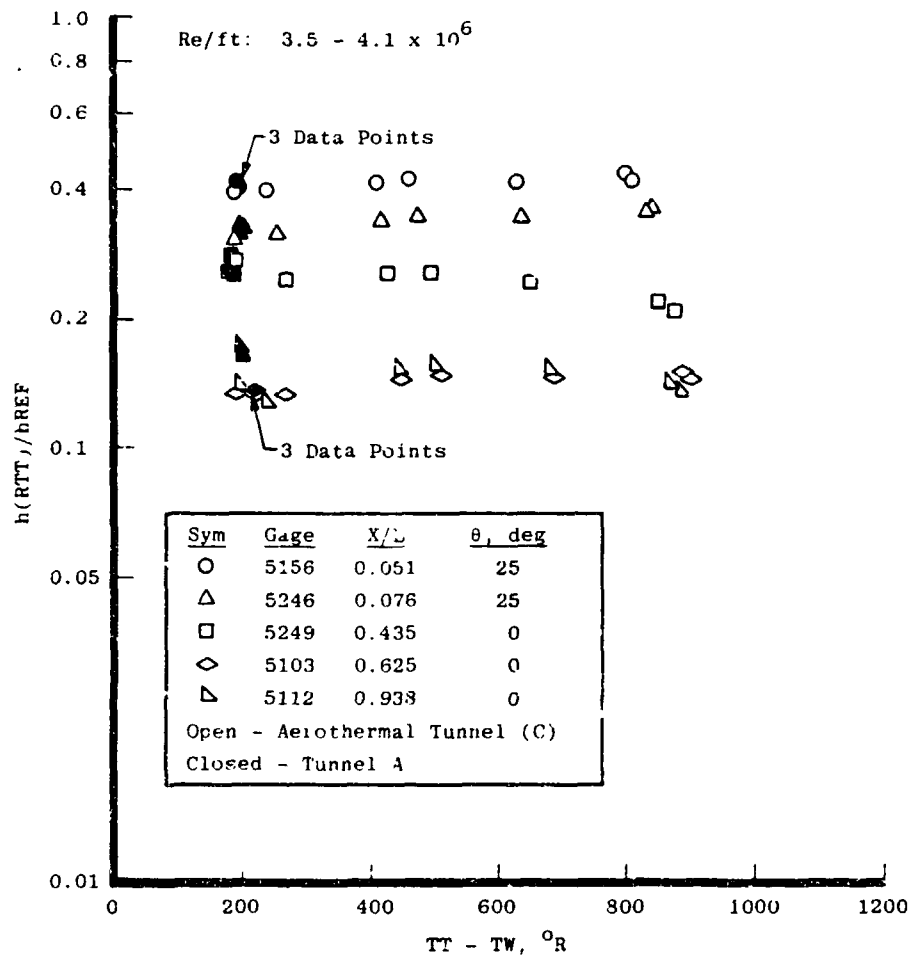
d. Alpha = 0 deg, beta = -3 deg



e. Alpha = 0 deg, beta = 3 deg
Figure 23. Concluded.

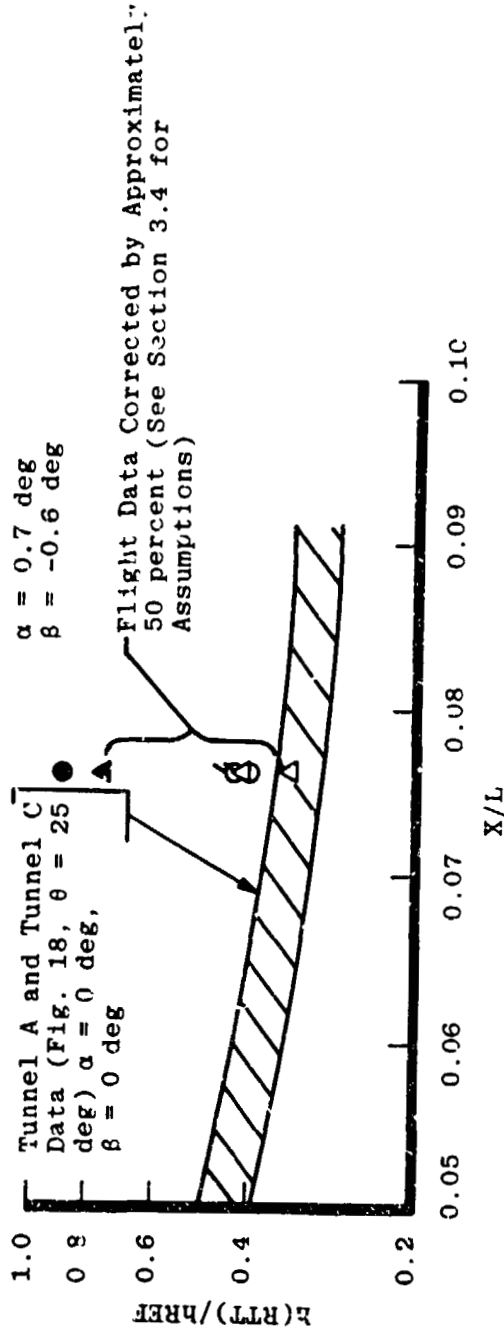


a. Comparison of Tunnel A and Aerothermal Tunnel (C) gage measurements
 Figure 24. Influence of temperature difference ($TT - TW$) on measured heating coefficient.

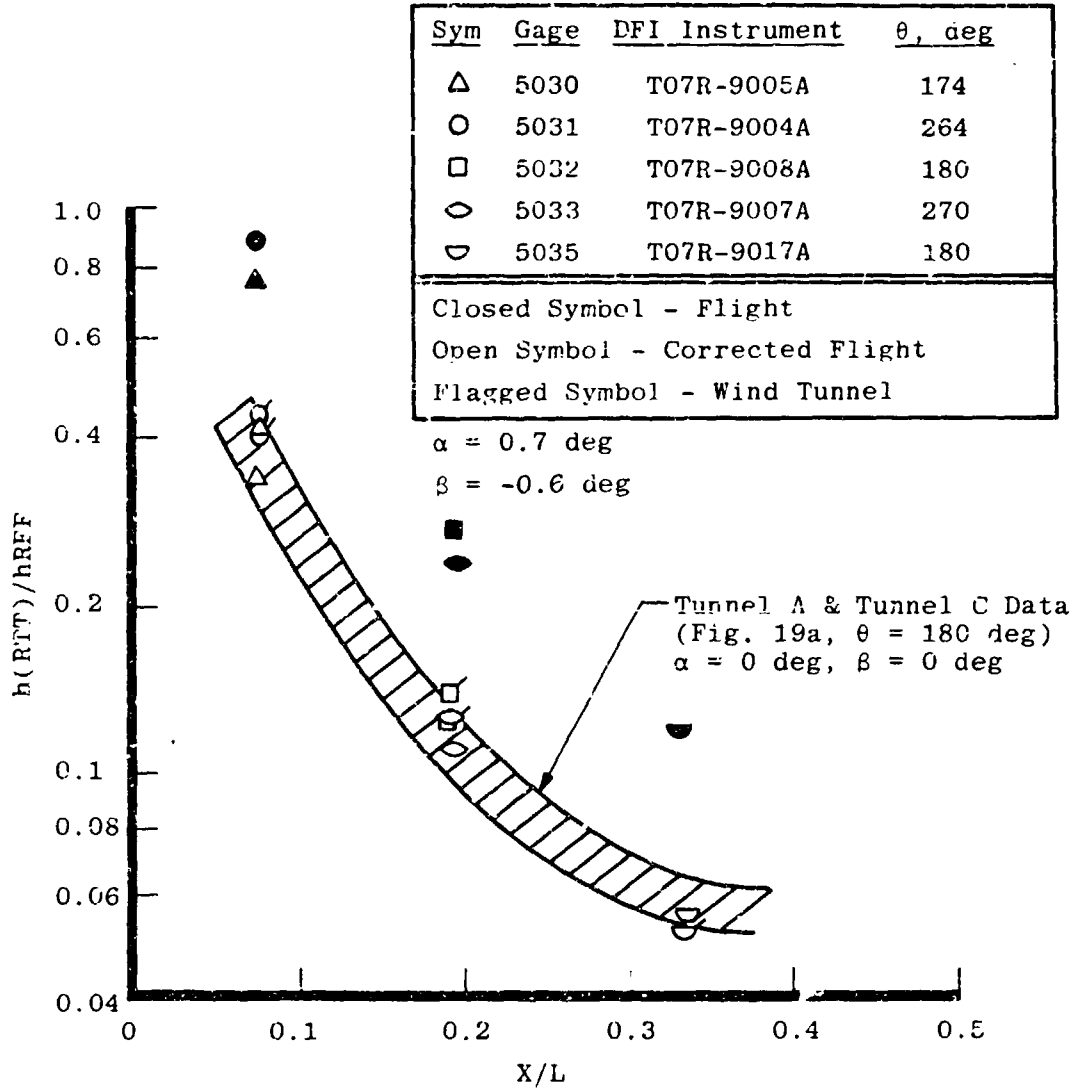


b. Comparison of Tunnel A and Aerothermal Tunnel (C) thin-skin T/C measurements
Figure 24. Concluded.

Sym	Gage	DFI Instrument	θ , deg
Δ	5030	T07R-9005A	174
O	5031	T07R-9004A	264
Closed Symbol - Flight			
Open Symbol - Corrected Flight			
Flagged Symbol - Wind Tunnel			



a. Heating distribution on nose section
 Figure 25. Wind tunnel-to-flight data comparison.



b. Heating distribution on bottom centerline.
 Figure 25. Concluded.

Table 1. Model Instrumentation Locations

Gage No.	θ , deg	X/L	Gage Type	Gage No.	θ , deg	X/L	Gage Type
626	0	0.440	T/C	5054	25	0.369	S-B
628	↓	0.450	↓	5055	27.5	0.362	↓
629	↓	0.455	↓	5060	17	0.545	↓
631	↓	0.470	↓	5061	33	0.937	↓
632	↓	0.480	↓	5072	280	0.290	T/C
633	↓	0.490	↓	5073	↓	0.300	↓
634	↓	0.500	↓	5074	↓	0.310	↓
635	↓	0.550	↓	5075	↓	0.320	↓
699	29.8	0.050	↓	5076	↓	0.330	↓
715	37.7	0.050	↓	5077	↓	0.340	↓
5030	174	0.076	↓	5078	↓	0.350	↓
5031	264	0.076	↓	5079	↓	0.360	↓
5032	180	0.187	S-B	5080	↓	0.370	↓
5033	270	0.187	T/C	5081	↓	0.385	↓
5034	270	0.270	T/C	5082	337.5	0.395	↓
5035	180	0.333	S-B	5083	337.5	0.470	↓
5036	251.4	↓	↓	5084	337.5	0.500	↓
5037	270	↓	↓	5085	330	0.395	↓
5038	288.6	0.333	↓	5086	330	0.431	↓
5039	2.5	0.418	↓	5087	343.1	0.395	↓
5040	↓	0.410	↓	5088	40	0.390	↓
5041	↓	0.424	↓	5103	0	0.625	↓
5042	25	0.352	↓	5109	270	0.880	↓
5043	270	0.383	↓	5110	255	0.880	↓
5044	180	0.409	↓	5111	315	0.938	↓
5046	264.4	0.630	T/C	5112	0	0.938	↓
5047	168.8	0.908	↓	5113	23	0.938	↓
5048	5.6	0.916	↓	5114	240	0.880	↓
5049	356.3	0.928	↓	5115	285	0.880	↓
5050	5.6	0.937	↓	5118	240	0.926	↓
5051	276	0.937	↓	5119	285	0.926	↓
5052	340.6	0.937	↓	5120	15	0.938	↓
5053	23	0.369	S-B	5121	240	0.938	↓

Table 1. Concluded

Gage No.	θ , deg	X/L	Gage Type	Gage No.	θ , deg	X/L	Gage Type
5122	345	0.938	T/C	5504	32	0.430	T/C
5123	58.5	0.800	↓	5508	↓	0.459	↓
5124	58.5	0.840		5512	↓	0.494	
5126	58.5	0.926		5515	↓	0.564	
5127	68	0.800		5534	38	0.879	
5128	↓	0.840		5535	32	0.879	
5129	↓	0.880		5537	27	0.465	
5130	↓	0.926		5538	27	0.844	
5131	75	0.800		5539	27	0.850	
5132	↓	0.840					
5133	↓	0.880					
5134	↓	0.926					
5156	25	0.051					
5157	↓	0.060					
5158	↓	0.080					
5159	↓	0.091					
5160	17	0.430					
5162	20	0.447	↓				
5173	20	0.861					
5181	37.7	0.057	S-B				
5242	180	0.040	S-B				
5246	25	0.076	T/C				
5247	8.2	0.187	↓				
5248	0	0.270					
5249	0	0.435					
5250	358	0.444					
5251	352.5	0.630					
5252	310	0.837					
5253	180	0.175					
5254	180	0.200					
5257	270	0.310					
5258	270	0.340					
5259	37.5	0.473		S-B			

Table 2. Test Data Summary

Tunnel	M	α , deg	β , deg	TI, °R				
				740	980	1050	1240	1440
A	4.0	0	0	39, 68				
				69				
				78				
				74				
		0	3	77				
C	4.0	0	0	100	99	98	97	86, 95
				101				89
				102				92
								87
		0	3	106				88
		0	-3					
		0.7	-0.6					

Run Number (TYP)

APPENDIX A IMPORTANCE OF RECOVERY TEMPERATURE

Experimental heating data are usually expressed in the form of the aerodynamic heat-transfer coefficient, h . This parameter is defined by Newton's law of cooling as the proportionality constant relating the local heat-transfer rate, Q_{DOT} , and the driving potential of the heat-transfer process. This driving potential is the difference between the local recovery temperature, TR , and the local wall temperature, TW . Thus, the definition of h is

$$h \equiv \frac{Q_{DOT}}{TR - TW} \quad (A-1)$$

In experimental work it is often difficult to determine the correct value of TR . It has become customary in hypersonic flow ($TT - TW \gg 200^\circ F$) to use a measured parameter, namely the stilling chamber temperature, TT , in place of TR , i.e.,

$$h_i \equiv \frac{Q_{DOT}}{TT - TW} \quad (A-2)$$

The assumption that $(TT - TW) \approx (TR - TW)$ causes little difficulty as long as TW is very small compared to TT . However, for test situations where $TT - TW \leq 200^\circ F$, both the numerator and denominator of Eq. (A-2) start to approach zero, and the above assumption is not valid. This is precisely the case for supersonic heat-transfer testing.

To investigate the significance of driving potential, consider the case where the heat-transfer coefficient is based on some arbitrary temperature, TX , instead of the actual recovery temperature, TR . The error is

$$\epsilon_h = \frac{h_{TX} - h_{TR}}{h_{TR}} = \frac{TR - TW}{(1 - \epsilon_{TR})(TR) - TW} - 1 \quad (A-3)$$

where

$$\epsilon_{TR} = \frac{TR - TX}{TR} \quad (A-4)$$

This heat-transfer coefficient error is presented in Fig. A-1 as a function of the temperature driving potential. As clearly indicated for $(TR - TW) < 200$ large errors (> 40 percent) can occur even for small errors in TR (e.g., 4 percent). Also shown in this figure are the temperature operating ranges of the VKF tunnels which are typical of those throughout the country for corresponding Mach numbers. For the hypersonic Mach numbers of 8 and 10,

the errors are relatively small; however, in the supersonic Mach number regime it is extremely important to consider recovery temperature effects. The one unique supersonic tunnel is the Mach 4 capability in the VKI Aerothermal Tunnel (C) which provides driving potentials of about 1100°F. This new tunnel was designed specifically for supersonic heat-transfer testing.

The lower temperature driving potential available in Tunnel A has caused concern regarding the quality of the Shuttle heat-transfer measurements obtained in this tunnel. Therefore, when the Mach 4 capabilities of the Aerothermal Tunnel (C) became available, the current test program was planned to compare the Tunnel A data with data obtained with a higher driving potential. The data presented in Fig. 24 showed good agreement (≈ 15 percent) between the two tunnels. There were at least two reasons why the larger potential errors (implied by Fig. A-1) were not produced in the data. The first reason is that considerable effort was expended in Tunnel A to improve the model cooling to lower T_W and increase $T_T - T_W$ to nominally 200° as seen in Fig. 24. The second reason is that an analytical method for calculating the theoretical value of TR at each measurement location was used. This method was formulated by Rockwell International and aided in reducing the error in TR (ϵ_{TR}). From Fig. A-1 it can be seen that the error in the heat-transfer coefficient is < 10 percent at $TR - T_W$ of nominally 200°R when $\epsilon_{TR} < 2$ percent.

Efforts to improve the model cooling capabilities have been underway since early in the Tunnel A Shuttle test program. This fact, coupled with the fact that the Rockwell method for calculating the theoretical value of TR has been applied to all but the earliest test data indicates that Tunnel A provided satisfactory data.

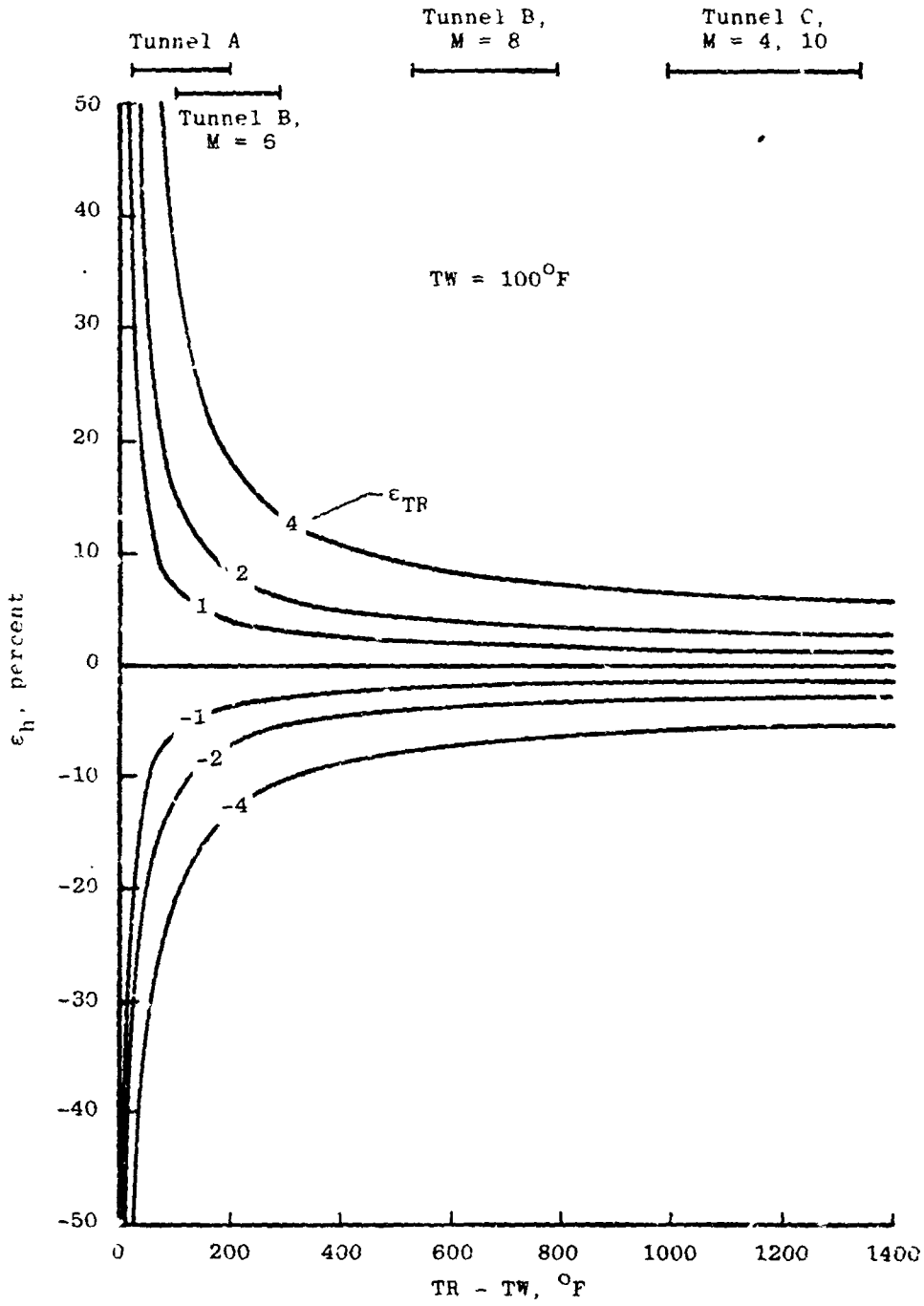


Figure A-1. Error in heat-transfer coefficient attributable to error in recovery temperature.

NOMENCLATURE

a_1, a_2, a_3	Denote constant terms used to calculate R, Eq. (10)
b	Model wall thickness, ft
c	Model wall specific heat, Btu/(lbm-°R)
dTW/dt	Derivative of the model wall temperature with respect to time, °R/sec
E	Schmidt-Boelter gage output, mv
$F(L/W)$	Geometrical function in Eq. (12)
$H(L/W)$	Geometrical function in Eq. (12)
h	Heat-transfer coefficient, Btu/ft ² -sec-°R (see Appendix A)
h_{REF}	Reference heat-transfer coefficient based on Fay Riddell theory and a 1-ft nose radius scaled to the model scale (0.0175 ft), Btu/ft ² -sec-°R
$h(RTT)$	Heat-transfer coefficient based on RTT, $QDOT/RTT - TW$, Btu/ft ² -sec-°R
$h(TR)$	Heat-transfer coefficient based on TR, $QDOT/TR - TW$, Btu/ft ² -sec-°R
L	Axial length of external tank model, in. (see Fig. 5). Also, approach length to step discontinuity in surface temperature, ft (see Fig. 11)
M	Free-stream Mach number
M_e	Mach number at boundary layer edge
P_T	Tunnel stilling chamber pressure, psia
$QDOT$	Heat-transfer rate, Btu/ft ² -sec
R	Analytical temperature ratio, TR/TT
r	Recovery factor

Re _o : Re/ft	Free-stream Reynolds number per foot, ft ⁻¹
RUN	Data set identification number
S.F.	Schmidt-Boelter gage scale factor, Btu/ft ² -sec/mv
T	Free-stream static temperature, °R
t	Time, sec
T _e	Temperature at the edge of the boundary layer, °R
TR	Boundary layer recovery temperature, °R
TT	Free-stream total temperature, °R
TW	Model wall temperature, °R
TW ₁	Wall temperature upstream of temperature discontinuity, °R (see Fig. 11)
TW ₂	Gage temperature downstream of temperature discontinuity, °R (see Fig. 11)
TX	Arbitrary recovery temperature, °R [see Eq. (A-4), Appendix A]
W	Approach length to downstream side of discontinuity, ft (see Fig. 11)
X	Model axial coordinate, in.
X/L	Nondimensionalized axial location
Alpha, α	Model angle of attack, deg
Beta, β	Model angle of sideslip, deg
γ	Ratio of specific heats
ϵ_h	Error in heat-transfer coefficient [see Eq. (A-3), Appendix A]
ϵ_{TR}	Error in recovery temperature [see Eq. (A-4), Appendix A]

AEDC-TR-84-3

δ The included angle between the free-stream velocity vector and local unit normal to the model surface, deg

Theta, θ Model circumferential measurement coordinate, deg (see Fig. 5)

ρ Model wall density, lbm/ft³

SUBSCRIPTS

i Initial condition